PRODUCTION AND CHARACTERISATION OF TITANIUM FOAM SCAFFOLDS AS BONE SUBSTITUTE MATERIALS

KEMİK İMPLANT MALZEMESİ OLARAK TİTANYUM KÖPÜK MATERYALİN ÜRETİMİ VE KARAKTERİZASYONU

OKTAY ÇETİNEL

PROF.DR.BORA YILDIRIM

Supervisor

Submitted to Graduate School of Science and Engineering of Hacettepe University
as a Partial Fulfilment to the Requirements
for the Award of the Degree of Doctor of Philosophy
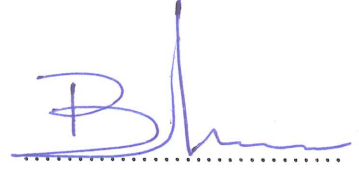in Mechanical Engineering

2019

This work titled "**PRODUCTION AND CHARACTERISATION OF TITANIUM FOAM SCAFFOLDS AS BONE SUBSTITUTE MATERIALS**" by Oktay ÇETİNEL has been approved as a thesis for the Degree of **Doctor Of Philosophy** in **Mechanical Engineering** by the Examining Committee Members mentioned below.
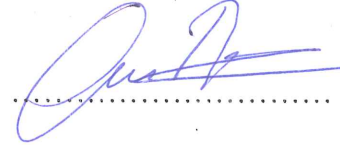
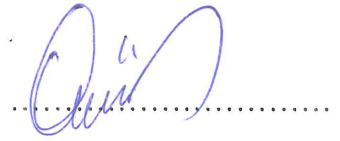Prof.Dr.Hakan Ateş
Head

Prof.Dr.Bora Yıldırım
Supervisor

Dr.Özgür Ünver
Member

Assoc.Prof. Dr. Can Ulaş Doğruer
Member

Assoc. Prof. Dr. Hakan Gürün
Member

This thesis has been approved as a thesis for the Degree of **Doctor Of Philosophy In Mechanical Engineering** by Board of Directors of the Institute for Graduate School of Science and Engineering on ..../..../......

Prof.Dr. Mememşe Gümüşderelioğlu
Director of the Institute of
Graduate School of Science and Engineering

ETHICS

In this thesis study, prepared in accordance with the spelling rules of Institute of Graduate Studies in Science of Hacettepe University,

I declare that

- all the information and documents have been obtained in the base of the academic rules
- all audio-visual and written information and results have been presented according to the rules of scientific ethics
- in case of using others Works, related studies have been cited in accordance with the scientific standards
- all cited studies have been fully referenced
- I did not do any distortion in the data set
- and any part of this thesis has not been presented as another thesis study at this or any other university.

09 / 07 /2019

Oktay ÇETİNEL

YAYINLANMA FİKRİ MÜLKİYET HAKKLARI BEYANI

Enstitü tarafından onaylanan lisansüstü tezimin/raporumun tamamını veya herhangi bir kısmını, basılı (kağıt) ve elektronik formatta arşivleme ve aşağıda verilen koşullarla kullanıma açma iznini Hacettepe üniversitesine verdiğimi bildiririm. Bu izinle Üniversiteye verilen kullanım hakları dışındaki tüm fikri mülkiyet haklarım bende kalacak, tezimin tamamının ya da bir bölümünün gelecekteki çalışmalarda (makale, kitap, lisans ve patent vb.) kullanım hakları bana ait olacaktır.

Tezin kendi orijinal çalışmam olduğunu, başkalarının haklarını ihlal etmediğimi ve tezimin tek yetkili sahibi olduğumu beyan ve taahhüt ederim. Tezimde yer alan telif hakkı bulunan ve sahiplerinden yazılı izin alınarak kullanması zorunlu metinlerin yazılı izin alarak kullandığımı ve istenildiğinde suretlerini Üniversiteye teslim etmeyi taahhüt ederim.

Yükseköğretim Kurulu tarafından yayınlanan "*Lisansüstü Tezlerin Elektronik Ortamda Toplanması, Düzenlenmesi ve Erişime Açılmasına İlişkin Yönerge*" kapsamında tezim aşağıda belirtilen koşullar haricince YÖK Ulusal Tez Merkezi / H. Ü. Kütüphaneleri Açık Erişim Sisteminde erişime açılır.

☐   Enstitü / Fakülte yönetim kurulu kararı ile tezimin erişime açılması mezuniyet tarihimden itibaren 2 yıl ertelenmiştir.

☐   Enstitü / Fakülte yönetim kurulu gerekçeli kararı ile tezimin erişime açılması mezuniyet tarihimden itibaren .... ay ertelenmiştir.

☐   Tezim ile ilgili gizlilik kararı verilmiştir.

.... / ...... /........

(İmza)

Oktay Çetinel

ABSTRACT

PRODUCTION AND CHARACTERISATION OF TITANIUM FOAM SCAFFOLDS AS BONE SUBSTITUTE MATERIALS

Oktay ÇETİNEL

Doctor of Philosophy, Department of Mechanical Engineering

Supervisor: Prof. Dr. Bora Yıldırım

Co-Supervisor: Assoc.Prof.Dr.Ziya Esen

July 2019, 147 Pages

Studies have confirmed that titanium (Ti) can improve the contact of bone and its surface growth. Titanium foam may, therefore, prove beneficial in aiding healing and the generation of greater power from implant regions. Biomedical methodologies have only recently sought to use porous metal frameworks in copying the structure and mechanical features of bone. When forming and constructing metal foams with the aim of achieving their best features, it is of utmost significance that their mechanical factors and possible failures of mechanism are comprehended. The way they behave mechanically is determined by their microform and their cellular organisation. Differences in density, topology, mechanics of breaks and cellular aluminium, steel and magnesium foam fatigue (mainly not biocompatible) have been researched a lot previously.

Nevertheless, for the new biocompatible foams such as the porous titanium foams, there is a lack of comprehension of their failure processes. This report therefore seeks to enhance the basic comprehension of the mechanical functions of titanium foams and new material that can be employed for biomedical use in the coming years.

The study spans details on how titanium foams are produced with individual chemical make up of three varied degrees of porosity; namely 60, 70 and 80% and which will define the features of both cancellous and cortical bone. The study also seeks to form a Finite Element Method (FEM) model for analysis of the implants made of titanium form. This would allow

for assessment of the mechanical properties across the various dimensions, compression settings and levels of porosity. This will result in the efficacious design of suitable implants at times of surgery.

Uniaxial compression testing was used to examine the performance in the mechanical context together with the compressive strength and the elastic modulus. The mean elastic modulus and yield strength values of the three degrees of porosity of the titanium foam were similar to those attained for human cortical and cancellous bone. Prior to and following compression, a macro and micro assessment of their physical and morphological parameters was carried out to aid in comprehension of the morphological features. This work was supported with the use of electron microscopes (scanning and optical), micro-CT, EDS (Energy-Dispersive X-Ray Spectroscopy) and XRD (X-ray Powder Diffraction analyses and Vickers hardness. Moreover, osteointegration was assessed for two, three and four weeks by immersion of the samples of titanium foam in substances that are similar to body fluid.

The primary objective of this study was comprehension of the degree of porosity and organisation of the foam that would adequately form inner connections to enable regeneration of vasculature whilst also mimicking the features of porosity associated with human bones. The best morphological and mechanical features regards human bone were achieved for samples that were 60% porous. However, the optimum mimicking of cancellous human bone was achieved at a degree of 80% porosity.

Finite element analyses were carried out in order to simulate the compression behaviour of the titanium foam implants with 60,70 and 80%. The outcomes of these evaluations supported the experimental findings which in turn resulted in model validation. The model was subsequently employed in the examination of distribution of stress within the titanium foam structure of dental implants. The findings of the research showed that the use of the space holder method to produce porous titanium scaffolds had great possibilities in the field of hard tissue engineering.

It is therefore anticipated that the findings of this study would be advantageous for the formation of new materials and their employment in the biomedical field.

Keywords: Fracture Mechanics, Titanium Foam, Mechanical Properties, Powder Metallurgy, Heat Treatment

ÖZET

KEMİK İMPLANT MALZEMESİ OLARAK TİTANYUM KÖPÜK MATERYALİN ÜRETİMİ VE KARAKTERİZASYONU

Oktay ÇETİNEL

Doktora, Makina Mühendisliği Anabilim Dalı

Tez Danışmanı: Prof. Dr. Bora Yıldırım

İkinci Tez Danışmanı: Doç.Dr.Ziya Esen

Temmuz 2019, 147 Sayfa

Çalışmalar, titanyumun (Ti) kemik temasını ve yüzey gelişimini artırabildiğini doğrulamaktadır. Titanyum köpük, bu nedenle, implant bölgelerinin iyileşmesini ve bu bölgelerden daha fazla güç elde edilmesini desteklemede faydalı olabilir. Biyomedikal metodolojiler, kemiğin yapısını ve mekanik özelliklerini kopyalamada poröz metal kafesleri kullanmayı ancak son zamanlarda denemektedir. En iyi özelliklerini elde etmek amacıyla metal köpük oluştururken ve yaparken mekanik faktörlerinin ve olası mekanizma kopmalarının iyi anlaşılması en büyük öneme sahiptir. Onların mekanik olarak davranış şekilleri, sahip oldukları mikro-form ve hücresel organizasyon tarafından belirlenir. Dansite, topoloji, kırılma mekaniği ve hücresel alüminyum, çelik ve magnezyum köpük yorgunluğu (daha çok biyo-uyumlu olmayan) farkları daha önce çok araştırılmıştır.

Yine de, poröz titanyum köpükler gibi yeni biyo-uyumlu köpüklerin kopma prosesleri yeterince anlaşılmış değildir. Bu tez, bu nedenle, önümüzdeki yıllarda biyomedikal kullanımda yararlanılabilecek titanyum köpüklerin ve yeni materyallerin mekanik fonksiyonlarının temel olarak anlaşılmasına katkıda bulunmayı amaçlamaktadır.

Çalışma, titanyum köpüklerin üç farklı, yani %60, 70 ve 80 porozite derecesinden oluşan ve hem süngerimsi hem de kortikal kemiğin özelliklerini tanımlayacak olan özel kimyasal ile nasıl üretildiğine dair detayları kapsamaktadır. Çalışma, ayrıca titanyum formdan oluşan implantların analizi için bir Sonlu Elemanlar Metodu (SEM) modeli oluşturmayı

amaçlamaktadır. Böylece, çeşitli porozite boyutlarındaki, sıkıştırma ayarlarındaki ve seviyelerindeki mekanik özelliklerin ölçümü mümkün olacaktır. Sonuç olarak, cerrahi durumlarda etkili tasarıma sahip uygun implantlar ortaya çıkacaktır.

Mekanik konteksteki performansın yanı sıra basınç dayanımının elastisite modülünün incelenmesi için tek eksenli basınç deneyi yapılmıştır. Titanyum köpüğün üç porozite derecesinin ortalama elastisite modülü ve sünme dayanımı değerleri, insan kortikal ve süngerimsi kemiği için elde edilenlere benzer bulunmuştur. Morfolojik özelliklerin anlaşılmasına katkıda bulunmak amacıyla basma testinden önce ve sonra, fiziksel ve morfolojik parametrelerinin bir makro ve mikro değerlendirmesi gerçekleştirilmiştir. Bu çalışma, elektron mikroskoplarının (tarayıcı ve optik), mikro-CT, EDS (Enerji Dağılımlı X-Işını Spektroskopisi) ve XRD (X-Işını Toz Kırınımı) analizlerinin ve Vickers sertliğinin kullanımı ile desteklenmiştir. Ek olarak, titanyum köpük numunelerinin vücut sıvısına benzer maddelerin içerisine immersiyonu yoluyla iki, üç ve dört hafta için kemik tümleşimi değerlendirilmiştir.

Bu çalışmanın esas amacı, insan kemiklerine ilişkin porozite özelliklerini taklit ederken vaskülatür rejenerasyonu sağlamak için yeterli bir şekilde iç bağlar oluşturacak köpük porozite derecesinin ve organizasyonunun anlaşılmasıdır. İnsan kemiğiyle ilgili en iyi morfolojik ve mekanik özellikler, %60 poröz numunelerde elde edilmiştir. Ancak süngerimsi insan kemiğinin optimum taklidi, %80 porozite derecesinde elde edilmiştir.

%60, 70 ve 80 titanyum köpük implantların basınç davranışını simüle etmek amacıyla sonlu eleman analizleri gerçekleştirilmiştir. Bu değerlendirmelerin sonuçları, model validasyonunu sağlayan deney bulgularını desteklemiştir. Model, daha sonra diş implantlarının titanyum köpük yapısındaki gerilimin dağılımının incelenmesinde kullanılmıştır. Araştırmanın bulguları, poröz titanyum iskeleler üretmek için aralık tutucu metodunun kullanımının sert doku mühendisliği alanında çok büyük olanaklar sunduğunu ortaya koymuştur.

Bu nedenle, bu çalışmanın bulgularının yeni materyallerin formasyonu ve bunların biyomedikal alanda kullanımı açısından faydalı olması beklenmektedir.

Anahtar Kelimeler: Kırılma Mekaniği, Titanyum Köpük, Mekanik Özellikler,Toz Metalurji, Isıl İşlem

ACKNOWLEDGMENTS

I would like to thank my principle supervisor, Professor Bora Yıldırım, for his kindness, guidance, and support. Without his support this work would not be possible. It was a fruitful journey overall and I have learned a lot through Professor Bora's supervision. The most important lesson of all has been to be an independent researcher.

I am grateful to my co-supervisor, Assoc.Dr. Ziya Esen for their continuous guidance and advice throughout my study and who also kindly allowed me to carry majority of my experiments in his lab. His support is greatly appreciated. I am also thankful to Ezgi Bütev at Metallic Implants lab for her technical support.

I would also like to thank Prof.Dr. Hakan Ateş and Assoc.Dr.Hakan Gürün for their continuous supply of their knowledge and suggestions on my work.

Finally, a special thanks goes to my Dad, who have always been on my side and supported me and for the sacrifices he has made.

TABLE OF CONTENTS

LIST OF TABLES

LIST OF FIGURES

1. INTRODUCTION

The recent developments in the field of biomaterials which exploit the innovations derived from molecular and cell biology are driving significant interest and advances in twenty first century materials science and engineering.

In the initiating stages of biomaterials, the materials used were standardly well defined from a technology perspective but the implants derived from the materials used for the manufacture of human medical or dental implants were not designed specifically for human applications. Examples may be found in a number of medical areas, including the application of low-corrosion steels and alloys or ultra-high density polyethylene being used to manufacture bone implants used by orthopaedic surgeons. Likewise, methacrylate polymers were used in the field of dentistry, fabrics were constructed to mimic blood vessels using polyethylene terephthalate fibres. One of the earliest examples is the use of cellulose-based membranes for kidney dialysis. Given the nature of these materials, research advancing their use was focused on *in vitro* testing scenarios to mimic biological challenges, and to determine the robustness of the materials to, for example, corrosion, fatigue, creep and wear.

Biological response to these materials was initially determined in animal models, in which the compounds had been implanted, with much of the suitably or otherwise being derived through histological assessment of tissues post-implantation. At this time, there was only a minimal drive to investigate alternatives to the existing material options; effectively utilising materials science parameters to guide the application of materials within the biomedical field. At this point, biomaterials were largely synthetic and their use was intended to be a permanent replacement or support to functionally replace damaged tissues. Biomaterial research was the domain of the engineers and physical scientists who worked in collaboration with pathologists and clinicians to define medical applications for the materials. Today, synthetic implant materials are derived from a variety of materials and their composites, including metals, ceramics and polymers.

Ease of production and relatively low costs, combined with desirable mechanical properties, have given metals a key role in biomaterials. Since early history, metals, even those considered as toxic to humans, such as copper, have been used for biomedical roles. The three most frequently used metals and / or their alloys used for biomaterial production are stainless steels, cobalt (Co) alloys, titanium (Ti) and its alloys. While titanium and titanium

alloys incur higher costs and more complex production methods than the others, they are the most interesting due to the corrosion resistance. This substantial advantage is likely to result from the ability to Ti and its alloys to form an oxide layer that is significantly resistant to corrosive compounds, including acid and salt solutions. A vital orthopaedic and dental material, titanium and its alloys are highly biocompatible with low failure rates resulting from metal fatigue.

More recently, scientists have focused efforts on implantable metal foams, including titanium and steel, used for 'scaffolding' [10-14]. The metal foams are porous and lighter weight, and have been developed to resolve stress-shielding issues. The major issue, reduced mechanical strength, with these metal foams in comparison to solid metal biomaterials results from spaces and disruptions within the structure.

In developing new biomaterials, both the mechanical properties and suitability for biomedical application need to be considered:

For a biomedical application the compound must exhibit reasonable bioactivity and facilitate bone-in-growth. One major benefit of the porous metals is the ability of bone to extend into the pores and enhances fixation and reduces healing time.

Mechanical considerations of these metal foams include density, elasticity, weight and surface characteristics, with major focus on fatigue and fracture for materials used in orthopaedic implants, due to the likely forces that they will be subjected to. It is logical to propose that highly porous metals will have reduced mechanical strength as porosity increases, which in necessary for new bone in-growth and tissue vascularisation. Consequently, it is vital for these materials to be rigorously tested for toughness, resistance to fracture and fatigue crack development. These aspects can be assessed by changes in microstructure of the metal foams.

In comparison with the newer titanium foams, aluminium-based foams are robustly defined and widely used in commercial applications, including aerospace and car manufacture [18, 36-41]. The specific base metal properties contribute to the point at which a metal foam fails due to fatigue; however, the fatigue point is also a function of the shape, topology and structure of the metal foams, which are dependent on the application and manufacturing processes.

The purpose of this thesis is to interrogate the mechanical behaviours of titanium foams, specifically used for surgical applications. The innovation of this work is to determine the range of titanium foam densities that may correspond to the mechanical properties of specific parts of the body, to enable selection of materials most suited to a fracture with respect to mechanics. Furthermore, this study researches the impact of both microstructure, that is cell size and shape and cell wall thickness, and microarchitecture on fracture mechanics of the titanium foams. Ultimately, this shows the process to improve the quality of novel porous substances for a range of biomedical applications.

To this end, this research focuses on resolution of issues relating to stress shielding and poor bone integration detected from 60, 70 and 80% porous titanium, derived by treatment with magnesium powder, heat treatment and NaOH, respectively. The biologically active surfaces produced are thought to unite with and form a stable bond with living bone. Relative bioactivities of treated and untreated materials are determined by *in vitro* testing to measure the ability of the materials to form an apatite layer (apatite-forming-ability, AFA) on immersion in fluid that is comparable with body fluids (simulated body fluid, SBF), ensuring that ionic concentrations remain within the range of normal human plasma.

In summary, the major objectives of this study are:

i)   Produce stable, contamination-free, highly porous titanium and titanium-foams, using limited soluble magnesium as a space-holder.

ii)   Provide a full and detailed description of material properties and methodologies used to produce the Ti foams, NaOH-alkali and heat treatments, and *in vitro* procedures.

iii)   Validating a 3D finite element analysis (FEA) mode against *in situ* μCT imaging assessment is shown to define the compressive characteristics and limits of the implant. Within this study, we present observations of the elastic behaviour of the foams. Furthermore, the strut failure is defined and the potential mechanism explored. The association between foam microstructure and the mechanical properties conveyed is assessed by analysis of three individual Ti-type foams.

iv)   The structural and mechanical characteristics of the cell wall are also determined, including porosity and neck size.

v) The comparison data on the mechanical response of the titanium foams to compression loading and define key parameters, such as Young's Modulus and yield strength, and the association of porosity and relative density, making use of both empirical data and theoretical determinations.

vi) To present and analyse the data collated from *in vitro* studies using SBF, and lastly, we draw our conclusions and give recommendations for future research in this area.

1.1 Thesis Layout

The thesis is categorise into the following areas:

- Numerical Analytical, and basic experimental methods,
- Titanium foam fabrication and morphology,
- Mechanical Properties and Finite Element Modelling

Following this introduction, chapter 2 provides a detailed critical review of the literature pertaining to this area, whereby previous research in titanium foams, specifically their mechanical properties, their manufacture and mechanical testing strategies are assessed and discussed. In brief, this chapter shows that previous work on titanium foams, specifically titanium-foams, largely focused on strength and basic mechanical functions. Consequently, this supports the critical need to interrogate the robustness of these materials in respect to damage tolerance through assessment of their microstructure, to elicit an insight into the most relevant aspects of the foam in stress conditions. The gap in the literature, specifically pertaining to the mechanical properties of titanium foams, facilitates our focus in the analysis of failure conditions of these porous compounds.

In chapter 3, we describe the production of the 60, 70 and 80% titanium foams and detail the structure. Furthermore, we discuss the applicability of the methodology used for manufacture of the biomaterials.

Thereafter, in chapter 4 we investigate the compressive and structural properties of the titanium foams and quality control of our procedures, with regards to standards used and methodologies applied in the study. Given the powder metallurgy process used to make the foams, the porosities are high and variable, resulting in a requirement for assessing compressive strength, Young's Moduli, yield strength, hardness and relative density.

4

Chapter 4 also incorporates the details and analysis of the experimental tests of the titanium foams, using a FEM model for heterogeneous materials. Using a simulation, we investigate the validity of a crushable foam model in Ansys, derived from aluminium foam alloys, for titanium, by comparing real sample damage with the simulation. Considering the compressive properties of titanium foams, we address the suitable of these compounds as skeletal bio-implants.

Finally, chapter 5 includes the conclusions drawn and recommendations for future works.

2. LITERATURE REVIEW

2.1 Background

Nature and the world around us have been exploited as a source of inspiration over generations, leading to the development of technologically important items, including aeroplanes, ships, computer systems and cameras. This approach is one which has informed the initial development of composites, and thereafter foams and nanomaterials [1].

With multiple parallels in nature, cellular structures which are by definition porous, are light weigh and stiff matrices, and they enable gas permeation, have high energy absorption and high thermal conductivity.
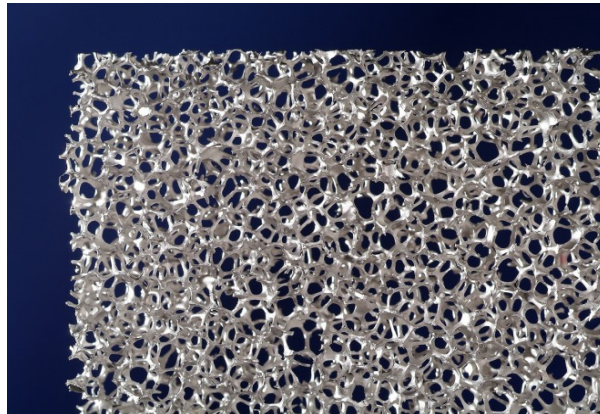
Figure 2.1 Titanium Foam [2].

Low weight and biocompatible titaniums are popular as a result of the blend of properties, including resistance to corrosion and high mechanical ability [2].

Merging the metal, titanium, and cellular structure delivers an individual biocompatible material with substantial benefits, irrespective of the production-related challenges. Over the past decade, the open nature of the cellular structure and porosity conveyed by titanium materials that facilitate bone ingrowth have shown excellent promise as orthopaedic implants. Previous literature indicates that the optimal parameters for titanium biomaterials that enable bone infiltration are 50-70% interconnection with pore size between 200-500 μm [3]. Shielding, an issue that occurs in response to differences in elastic modulus of the two materials – that is, bone and titanium-based biomaterial – may be subverted by altering porosity of the titanium, which in turn alters the mechanical characteristics.

Liquid titanium is highly reactive, and this property demands that production of a highly porous titanium foam depends on the solid form of the metal. Production falls in to two broad categories, firstly, costly methods, which result in maximum porosities of 44%, and include plasma-spray, electro-discharge sintering or gas entrapment; and secondly, using powder metallurgy as a space holder [4,5]. In addition to economy, applying a space holder method is beneficial as it facilitates changes in porosity, pore size and location. Further, this method is straight forward, requiring a simple mix and compaction of metal powder and space holder, thereafter removing the space holder at low temperatures before exposing the remaining shaped metal to be sintered at high temperature. Other researchers have demonstrated an ability of achieving up to 80% porosity when using carbamide as a filler in the space holder process; however, they researchers in this case fail to provide details of the production process [6,7,8].

2.2   Structure of Bone

There are two types of bone, cortical and cancellous / trabecular, which are also termed compact and spongy, respectively. In a long bone, curtail bone outweighs cancellous bone in a ratio of 4 to 1. While the base materials of these bone types is the same, the difference is represented by level of porosity and organisation. Cancellous bone is highly porous, ranging from 30 – 90% porosity, with the vast majority in the higher 75 – 95% range [9]. Conversely, cortical bone is less porous, with a range of 5 – 30%, with the majority in the 5 – 10% range [9].   Porosity is a variable factor in bone, with alterations resulting from load, age and disease status.
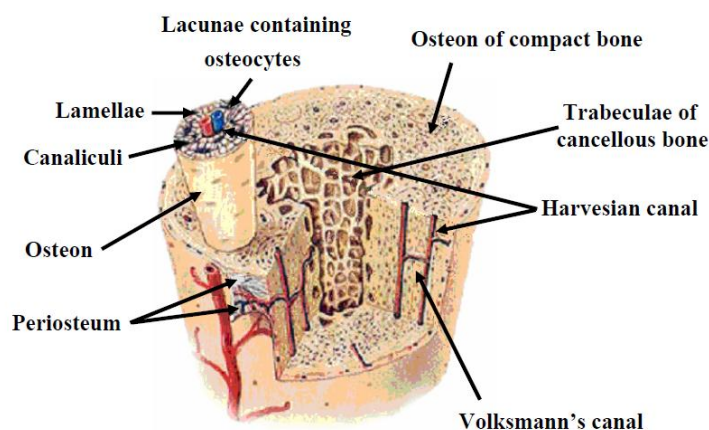
Figure 2.2 Structure of Bone [9].

The balance of bone density is maintained by the actions of two cell types, specifically, bone

forming cells, osteoclasts, and cells responsible for absorption and break down, osteoblasts. A third cell type, osteocytes are the mature bone cells [9].

2.2.1 Compact Bone

Compact bone comprises of tightly arranged osteons (Haversian systems), which are so dense as to appear to be solid, as seen in Figure 1.2. The structure of the osteon is a middle channel (the osteonic or Haversian canal) surrounded by a matrix of surrounding rings (lamellae) [10]. Cylindrical in shape, the osteons have a diameter of $200 - 250$ μm and are oriented in a near-parallel configuration with the centre axis of the bone. The osteocytes, bone cells, are found within the lacunae, which the spaces of the lamellar matrix. To enable movement through the tough matrix, canaliculi, small channels, connect the lacunae with the Haversian canals. Blood is supplied to the internal aspect of the bone via blood vessels, which run parallel to the long axis of the bone, within the osteonic canals [9]. The compact cortical bone is a relatively brittle substance that demonstrates viscoelasticity and anisotropism, that is, it shows differing physical properties depending of direction of measurement. The properties of cortical bone are a function of porosity, level of mineralisation and the organisation of the matrix [11].

2.2.2 Cancellous (Trabecular) Bone

Lighter and less dense than coritcal bone, cancellous (trabecular) bone comprises of trabeculae and endosteum of bone. The spongy bone components, a porous structure, are found side by side with irregularly shaped, small, red bone marrow-containing voids. Unlikely compact bone, which is served via the central Haversian canal, blood supply is achieved via a network of canaliculi connecting the cavities [11]. Whilst the arrangement of trabeculae looks irregular, the organisation is designed to deliver optimal strength in a manner similar to bracing a building during construction. Following the stress pathway, trabeculae are able to realign when the direction of stress alters. Metabolically active, and unlike cortical bone, cancellous bone is frequently remodelled and age-related mechanical function changes are observed [12].

2.3 Characterization of Bone

Retaining moisture in the bone during testing is critical as the properties of bone alter if samples are allowed to dry. Both ultrasound and destructive testing of samples are common to quantify the mechanical properties of bone. To mimic the in vivo situation, how a bone

sample deforms in response to various mechanical stresses, including tensile, compressive, torsion or shear forces is taken as a measure of mechanical strength [13]. The requirement for multiple samples and the available small sample size restricts in vitro bone testing, and consequently, there is interest in ultrasound applications for this testing [14]. The relationship between the speed of sound and the elastic properties of the bone means that rigorous testing can be conducted on fewer bone samples to generate similar data as destructive testing.
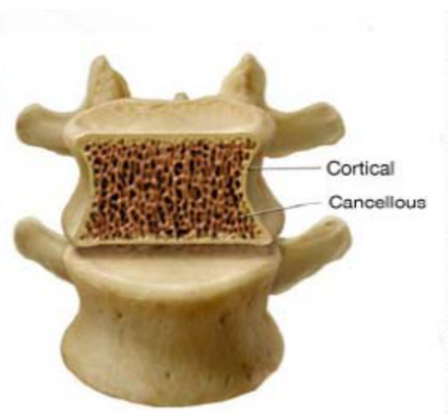
Figure 2.3 Human Vertebra [11].

Mechanically, cortical bone comprises of three phases, that is, mineralised matrix, collagen fibre network and fluid-filled cavities.

2.4   Mechanical Properties of Bone

Resulting from their different makeup, cortical and cancellous bone have differing mechanical and metabolic properties. The greater stiffness of cortical bone facilitates a larger stress burden, but significantly lower strain than cancellous bone prior to failure. Indeed, trabecular bone can resist strains of up to 75% while cortical bone fractures at strains in excess of only 2% [13]. The mechanical properties of these two types of bone are largely dependent on the volume fraction of calcium present. That is, higher calcium confers greater stiffness and strength, but lower toughness. In addition, the strength and mechanical toughness of bone is also associated with time, biological age and strain rate [15]. From a metabolic perspective, cancellous bone stores more energy than cortical bone.

(i)   Biological aging: Both strength and elasticity of bone decrease as an individual ages [16]. This is particularly evident in children, where their bones generally absorb more energy prior to failure, in spite of their bones being weaker, in a child the bones

end to be more accommodating to stress.

(ii) Strain rate effect: Both ultimate strength and elastic modulus of cortical bone increase in response to increased load or strain rate, while conversely the ultimate strain decreases. More sensitive than other body tissues, bone is responsive to strain rate, and at low rates is functions as a viscous substance. Furthermore, fracture toughness of bone is closely correlated to strain rate [16].

Biological materials possess a unique ability to repair damage caused by cyclical loading and unloading, which leads to micro-damage, when compared to non-biological structural materials. If repair mechanisms are activated in these cases, the damage does not increase; however, there are various situations that inhibit or slow the repair mechanisms, including ageing, which reduces bone mineral composition, metabolic conditions, such as osteoporosis, or by some prescribed drugs [17]. Lastly, repeated loading without allowing adequate repair time leads to fatigue failure.

Mechanical properties of bone can largely be defined by three critical measures, which can be derived from a force-deformation chart, specifically ultimate force, maximum deformation to failure and level of energy sored prior to failure. The ultimate force varies dependant on the type of load applied to the bone and is a measure of the maximum load and loading rate that the bone can tolerate before it breaks. The area under the force deformation curve represents the energy absorbed prior to failure and is a function of both ultimate force and strain [18].

2.5   Replacement of Bone

In biomedical applications, replacement or augmentation of bone by either synthetic or naturally occurring materials is necessary to overcome pain resulting from trauma or disease. Bone may be replaced by joint arthroplasty or bone grafting, and augmentation requires the application of fixation materials to facilitate fracture repair, stabilise or fuse a joint, and for alignment or distraction of bones [19]. Singh et al. [14] state that design of bone prostheses demands solutions to multiple requirements which include:

(i)   Cover a wide range of patients, based on anatomy.
(ii)   Sustain fixed position when exposed to cyclic loading
(iii)   Deliver a good, functional range of motion.

(iv)   Deliver the necessary kinematic stability.

Functionality drives the implant design, both from a patient perspective and from the surgical perspective: note of the surgical procedure and requirements are key aspects to developing orthopaedic prosthetics [14].

As a starting point the composition of the biomaterial is key, including assessment of biocompatibility. For orthopaedic implants, three main types are considered. Firstly, those which are stringently inert and can be removed at a later date, including fixation plates, and secondly, those which resorb over a period of time, and lastly, those which enable bone ingrowth at the bone/implant interface, which is termed osseointegration [7]. The geometric structure of the implant is a further critical aspect to consider during development. The structure controls the stress levels at the interface and within the local area of bone [20]. Furthermore, the geometry of the prosthesis, specifically in joint replacement, controls the range of motion and kinematic stability of the surgical site. Stringent regulation in this area ensures well-controlled design and development of novel implants.

Novel developments in implants include biocompatible scaffolds which stimulate 3-dimensional bone growth, and consequently, the design must incorporate the parameters for bone regeneration. Biocompatibility, that is a lack of inflammatory response to the implant post-surgery, is vital [13].

Inducing 3D cell growth is a complex operation, which incorporates the cellular and surface interaction to optimise cell affinity. The physical characteristics of the surface, including the particle size and texture are further aspects which directly control cell attachment and proliferation. Appropriate cell differentiation and proliferation is directed via the macrostructure of the implant, which should mirror the normal environment for the cells [21].

To facilitate cell ingrowth and angiogenesis, the implant should be a porous structure, with porosity of between $200 - 500$ μm depending on the targeted cell type [22]. The structure is optimised in such a way as to allow easy distribution of body fluids, nutrients and gases to support cell distribution, proliferation and migration and facilitate the removal of toxic waste products. The design of the implants provides a high internal surface area when compared to the volume, this is vital to allow growth of a sufficiently large number of cells [17].

11
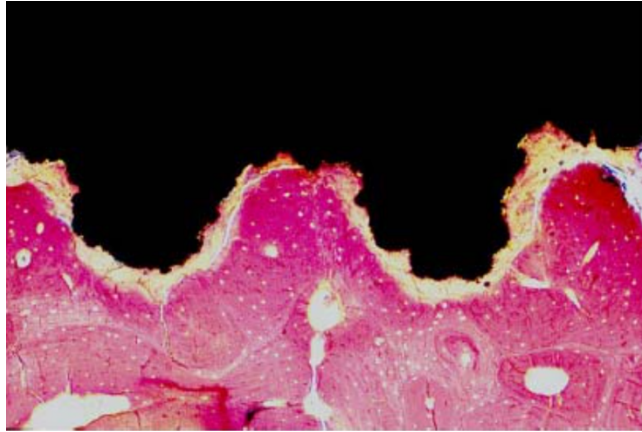
Figure 2.4 Titanium- Bone Bonding [17].

Further to the requirement for biocompatibility and cell-growth compatibility, scaffolds must confer a high mechanical strength until the novel bone or tissue is fully formed to ensure that they can remain functional when exposed to physiological stress and loads. From a production perspective, the seamless and timely provision of quantities of implants is vital [23]. Overall, there is no standard requirement for tissue engineering implants, this is largely a result of the wide range of demands conferred by different tissues, and manufacturers produce scaffolds which vary in pore size, shape and connectivity, surface chemistry and implant rigidity, all of which influence the surgical outcomes.

2.6   Implant Design Criteria for Bone Fixation

Biological fixation is a method introduced in the late 1980s to overcome the issues observed, including implant fracture, that resulted from wear of metal plates and pegs [22,23,24]. Biological fixation requires the use of porous materials which induce bone in-growth and integration [25]. An alternative method is termed morphological fixation, whereby the bone grows into the pores of the implant but does not forge a bond.

The chemical and structural properties of the implant, combined with the mechanical compression and scope of motion at the implant and bone interface control the biological or morphological fixation response. A number of authors [26,27,28,29] concur on the major criteria necessary for the 'optimal' implant to facilitate bone fixation, and the requirements include:

- The material should not be toxic and it should be designed to induce cell attachment and growth.

- The material should be provided in a 3D structure with pores and channels suitable for cell invasion and to facilitate transfer of nutrients and waste products.
- The surface chemistry and physical properties, including orientation and texture, should be designed to encourage cell attachment.
- The mechanical attributes of the implant should correspond to those of the patient bone, both for fixation and bone development. The implant must be capable of sustaining necessary loads and it should have the required modulus to negate stress shielding.
- The implant should exhibit good resistance to wear and be non-corrosive, both of which are vital to minimise debris and maintain a strong bond.
- The shape of the implant should closely mirror the affected area of bone.
- Commercial production requires substantial quantities of sterile implants and design must accommodate the international standards for clinical usage.

The internal 3D structure is critical to ensure cell attachment, migration, growth and establishment of an extra cellular matrix, all of which require effective nutrient and oxygen transfer, achieved by optimisation of pore size and interconnectivity between the pores [30]. Researchers have established that pore sizes between $100 - 500$ μm [31,32] and connecting tunnels larger than 100 μm facilitate development of a blood supply [33]. When discussing surface area, we must remember that the internal surface of a 3D structure is as important as the external structure, and the properties of roughness, strut orientation and topology are vital within the structure [34]. The texture of the surface roughness is a key factor in cell attachment, proliferation and differentiation, with researchers indicating that surfaces exhibiting greater texture promote enhanced cell attachment in comparison to smoother surfaces [35,36].

Optimally, an implant should possess mechanical and physical attributes that mirror the correponding bone, that is, the implant must have adequate strength to retain its shape whist facilitating bone remodelling.

The stiffness of the implant is critical to enabling appropriate bone remodelling. We know that bone remodels as a direct response to the load that is exposed to [37]. This law explains that increasing load on a bone induces remodelling of the bone, which strengthens to resist the load. However, if an implant is stiffer than the surrounding tissues, it will carry an

unequal load and consequently the bone will be subjected to lower stresses and lose density and become weaker [32]. Alternatively, if the implant is less stiff than the surrounding tissues, the implant may fail as a direct result of high stresses. This effect termed the imbalance between the implant and patient tissue 'the stress shielding effect', and demonstrates the necessity for the implant to maintain its structure post-implantation while ensuring that the modulus does not exceed the critical limit to minimise stress shielding of the patient's bone [33].

2.7 Biomaterials for orthopaedic applications

Degenerative and inflammatory diseases of bone and joints are a global issue, impacting millions of individuals, half of which occur in the over 50 age group of individuals in first world countries. Given the ageing demographic in developed countries, this figure is likely to increase substantially by 2020 [35,36].

The demand exceeds these chronic disease states, with significant surgical need being required for hard tissue replacement, in the form of hip replacements and such like, in response to dysfunction of the bone-joint interface. Furthermore, many other musculoskeletal issues require similar intervention, including osteoporosis, back pain and fractures, all of which may necessitate interventions with biomaterials which could be permanent, temporary or biodegradable. These demands are met by development of materials that meet key functionality specifications and which are safe for implantation [37].

The body's response to the biomaterial is pivotal for the success of the implant, and a substantial body or research has been undertaken to define both positive and negative material and host interactions [38,39], with the aim of developing robust, long-lasting biomaterials that minimise any negative immune responses. Individual biomaterials are designed to meet specific criteria while reducing any negative host response.

2.7.1 Biological compatibility

Biocompatible materials, also termed biologically compatible materials, interact with the host tissue without causing any negative responses that result from toxicity or cytotoxicity. A biocompatible scaffold will enable normal cellular functionality, including cell signalling, with zero toxicity at a local or systematic level [40]. Provision of a substance this is not toxic nor cytotoxic, ensures that cells are not damaged, metabolism is not inhibited and the

immune system is not induced to cause wither inflammation or an allergic response.

The introduction of non-native materials to the human body induces a response, which drives destruction and breakdown of the materials by chemical and enzymatic means. Consequently, the performance of an implant is based on the host response and the level of material degradation in the body. Alternatively, if the material cannot be broken down by the host response, it is encapsulated as a protection mechanism. Classified in accordance to encapsulation tissue thickness, the reactions to metal implants are in two categories. For titanium alloys, stainless steel and Co-Cr alloys, minor reactions are observed, and more serious reactions observed for Fe, Co, Cr, Ni [41].

Toxicity of the implant materials induces a continued inflammatory response which can result in death of surrounding tissues, while biotolerant and bioinert materials do not induce a toxic response, they may lead to the production of a fibrous capsule surrounding the implant which causes weakening of the tissue-implant bond [42]. This weak association facilitates small movements between the two surfaces (micromotions), which stimulates thickening of the connective tissue. It is accepted that small movements, around 40 μm stimulate ordered bone development, while larger movements, around 75 μm tend to initiate the growth of fibrous tissue within the implant [43,44]. Furthermore, these larger micro-movements may result in fretting-fatigue corrosion failure of the implant.

On the other hand, bioactive materials induce tissue regeneration and integration, specifically useful in hard tissue replacement situations [42, 45-49]. The bioactive materials stimulate the production of a bone-like substance, derived from carbonated hydroxyapatite (CHA), which forms a compatible layer on the implant surface post-operatively [50,51].

Additional to the chemical make up of a biomaterial, both the geometric and macro-structure are pivotal to the success of an implant. The macrostructure is vital to induce bone formation, comparing two ceramic structures of the same chemical composition, but differing structures, show that the dense structure does not facilitate bone in-growth and formation, whereas a more porous structure does, indicating the critical nature of controlled porosity in the manufacture of these structures [52,53]. Osteoinduction, the recruitment and differentiation of cells that become osteoblasts, when using inductive materials is controlled by the ability of blood vessels to access the interior of the structure to provide nutrients and oxygen to the cells [54].

Ideally, a 'perfect' scaffold should be capable of being resorbed as is degrades at a controlled rate to give space for new bone formation [55]. The rate of degradation is dependent on the specific application, with some situations demanding slower or faster degradation times. Resorbable materials are currently used for multiple orthopaedic issues, include cartilage replacement, bone substitution and repair.

The combination of destructive environments, frequently at extreme pHs, with exposure to both static and repetitive stresses, induces degradation of biomaterial into ions and debris, and non-toxic compounds should be selected for preparing alloys [56,57]. It is necessary, therefore, to consider the biocompatibility of the products of degradation, some of which may be locally of systemically damaging, to ensure that negative responses are minimised. The degraded compounds are defined within two toxicity classes, firstly, chemical toxicity produced by the release of particles and monomeric compounds, and secondly, mechanical toxicity from non-dissolving particles replaced by mechanical means. Biomedical implants, such as replacement joints, can release a wide range of debris when exposed to the in vivo environment, including metals, ceramics and polymers.

The most widely used metallic implant material is Ti_6Al_4V, which contains vanadium, an essential element for humans and one which is highly soluble in this material. Indeed, the solubility may be an issue as it can reach levels of toxicity [58,59].

Particulate matter is associated with ceramic implants, more so than ionic debris, with cytotoxicity observed at relatively lower levels of ceramic particles, such as TiO_2, Al_2O_3, ZrO_2 and Si_3N_4 than metal ions [60]. Levels of relative cytotoxicity for metals can be observed in cell cultures, whereby lower rate of cell growth is associated with cytotoxic materials.

Patient allergy to metal ions is an important consideration when selecting biomedical materials. Metal ions originating from the implant may be released through sweat and body fluids, reaching the skin and enabling keratin binding of ions including Ni, Cr and Co [61,62]. Metal allergies, where we observe that cobalt and nickel are the second most allergenic. However, it is worthwhile taking a wider view, as while the ions and debris from cobalt are highly allergenic, the alloys formed are robust in terms of fatigue and corrosion resistance [63].

2.7.2 Biomechanical compatibility

Most important for hard tissue replacement situations, biomechanical compatibility, in terms of similarity with the host tissue, is a vital criteria. Similar indices of strength, elastic modulus and fracture toughness enable the optimal outcomes, and these properties for a range of materials can be seen in Table 2.1. Failure of implants as a result of fatigue, the resistance or lack of resistance to repetitive and alternating stresses or strains, is commonly reported in dental implants [64] and hip replacements [65-68], and may also produce harmful debris though the fretting and fatigue process.

Table 2.1 Mechanical attributes of human bone, metal, composite biomaterials [69,70,71-73].

Material	Density (g/cc)	Compressive strength (MPa)	Elastic Modulus (GPa)	Toughness (MPa m$^{1/2}$)	Tensile strength (MPa)[c]
Cancellous Bone		4-12	0.02-0.5		10-20
Cortical Bone	1.8-2.1	130-180	10-40	3-6	82-114
Ti and Ti Alloys	4.4-4.5	590-1117	55-117	55-115	900-1172
Co-Cr-Mo Alloys	8.3-9.2	450-1896	200-253	100	400-1030
Stainless Steel	7.9-8.1	170-310	189-205	50-200	515-620
Zirconia	6.1	2000	220	9	800-1500
Alumina	3.98	4000-5000	380-420	3-5	282-551
HAP	3.1	600	73-117	0.7	38-48
CF/PMMA			55		772
CF/Polysulfone			76		938
CF/Epoxy Stycast			30		535
CF/Epoxy Hysol			24		207

In respect to the conditions that implants may be subject to, the materials used must be of sufficient strength and fracture toughness to withstand both static and dynamic loads. Material choice is significant, with ceramics possessing high strength but comparatively low toughness, while polymers have too much flexibility and are not sufficiently strong the meet the mechanical demands of orthopaedic implants. While metals and composites possess high levels of both strength and toughness, their elastic modulus, which is higher than bone, may

be problematic.

For replacement of bone tissues, such as the femur, which comprises of both cortical and cancellous bone and exhibits an elastic modulus of 10-40 GPa, depending on the specifics of measurement [18,61], the implant standardly is required to have a elastic modulus approximating in comparison to the human bone. Some simulations indicate that an implant modulus that is lower than the bone may enhance bone growth [74], while it is also recognised that implants with a higher modulus bears more load and consequently the bone does not receive sufficient loading, generally 25-40 MPa, to maintain the bone density [75], which is termed stress protection or shielding.

Protecting the bone from adequate stress increases resorption surrounding the implant area and leads to bone loss [76,77], ultimately causing failure of the implant. Optimal choice of material for structural biomaterials should meet the following criteria, which are comparable to that f bone, such as high strength and toughness and young's modulus adjacent to, or slightly lower than, bone. If these conditions are met, the implant is less likely to be maintained for the longer-term without loosening around the implant.

2.7.3 Corrosion resistance

Corrosion of biometals occurs as a function of many chemical variables, including the geometry, metallurgy, mechanical and solution [78]. Standardly, electro-chemical methodologies are employed to measure the corrosive nature of these compounds in biological systems, and include potentio-dynamic polarisation and electrochemical impedance spectroscopy, which are used to quantify the effect within the body. Body fluids are known to be corrosive to metal substances, and consequently, metal-based implants may corrode and cause issues within the body. Nowadays, metal implants are protected from corrosion by the application of a protective surface film, which effectively minimises current flow and restricts the release of corrosive by-products into the system.

Corrosion tests on non-vanadium titanium alloy in Ringer's solution demonstrate measurably greater resistance to corrosion than comparable testing with CP Ti [79]. Testing a range of titanium alloys in an alternative physiological solution (Hank's solution), showed that all of the alloys tested displayed stable passive polarisation parameters, and likewise the corrosion potential and corrosion current density were also comparable, with ranges of -379 mV to -606 mV and 0,08 $\mu A/cm^2$ to 0,48 $\mu A/cm^2$, respectively. Similarly, for all alloys

18

tested, unique breakdown potentials and large passive ranges were noted [80].

The mechanical properties of porous metallic implants have been extensively investigated, and likewise the effect of porosity on corrosion parameters has also been rigorously tested. Significantly, the findings reveal that highly porous metal structures that facilitate the improved exchange of fluids and gases generate a material that is more resistant to pitting. The build up of potentially incompatible metal ions, the products of corrosion, may result in allergic or toxic reactions and ultimately reduce the usable lifetime of the implant [81,82].

Frequently experienced in orthopaedic prosthetics, including the knee and hip, the capability of the implant to resist wear is another key contributor to determine the lifespan of the device. The implant may become loose as a result of wear and there are reports of debris resulting from wear causing substantial unwanted tissue reactions [83, 84].

2.7.4 Osseointegration

Originally defined as the direct link between viable bone and a load bearing implant contained within human bone, determined by light microscopy [85], osseointegration is the term currently used for close contact between implant surface and the bone [87]. Effective anchoring implants within surrounding bone contributes substantially to the lifespan and minimises risk of failure.

Close attachment between the implant surface and the bone is accomplished by either biomechanical or biochemical means, or a combined methodology. Using or coating the implant with bioactive materials enables biochemical bonds, whereas biomechanical bonding requires the bone to grow into the implant by attachment to rough surfaces, established via porous coatings or using a porous material. Biomechanical processes generate a 'lock' between the two surfaces. For optimal osseointegration the design of implant materials considers surface chemistry, roughness, morphology and topography [86, 88].

Three further criteria that biomaterials must meet are steralisabilty, without the breakdown of the materials, functional, that is, the materials can be formed to meet the needs of a specified function, and manufacturability, that is the materials must be able to be prepared for used in the specific implant [89].

19

2.8   Titanium (Ti) as Orthopaedic Implant Material

Commonly used metals for biocompatible implant manufacture include stainless steel, cobalt chromium (CrCo) alloys and titanium and its alloys are being used in surgical applications over fifty years [89,91]. In addition to its uses in replacement orthopaedic joint prosthetics, titanium implants are also used in stents and dental implants [85].

Ti is very well tolerated within the human body and it is considered to be near-inert in vivo [93]. When compared to other metals, such and stainless steel and CrCo alloys, Ti exhibits a high level of biocompatibility and significant resistance to corrosion, likely as a result of the spontaneously occurring TiO_2 stable surface layer [92,93,94].

Figure 2.5 Titanium Bone Implant [4].

The light weight and beneficial mechanical properties of Ti, including high and suitable compressive and tensile strength, low modulus and density in comparison to other biometals are beneficial in implant design [95]. The requirement for close alignment of implant mechanics with the corresponding bone is often neglected in orthopaedic implant design. Xue et al. [94] established that compact bone has elastic modulus in the range 3 – 30 GPa, and cancellous bone, 1 – 10 GPa. When comparing metal and metal alloy modulus, we see that titanium and its alloys have young's modulus within the range of 55 – 110 GPa [93], whereas stainless steel and cobalt alloys have moduli around 210 and 220 GPa, respectively [96]. We can clearly see that the young's modulus for titanium and its alloys have similar mechanical characteristics to the human cancellous and compact bone than the other metals and alloys. Titanium and its alloys show high strengths, in a range (220 – 1100 MPa) comparable with stainless steel, however, the specific strength, a measure of strength / density, of titanium and Ti alloys is greater.

Furthermore, the debris produced, resulting from wear, gathers in local tissues and produces osteolytic lesions within the joint [97]. Ultimately, the implant may become loose and cause pain due to production of a fibrous capsule around the implant and a high friction level [98]. Encapsulated Ti implants have a substantially diminished lifespan, due to the reduced level of bonding between the two surfaces. It is imperative, therefore, to continue to explore and develop novel Ti implants that closely mimic the structural and mechanical properties of human bone and that can facilitate robust integration between the two [99,100]

2.9 Porous Titanium (Ti) Implants for Bone Fixation

Early fixation of metallic implants standardly used cements or screws [101]. When using cement in prosthetic joint replacement surgeries, a liquid cement is injected to the damaged area, the cement is allowed to polymerise before application of the implant to the bone. As an alternative, the implant may be attached by means of screws or interference fits directly in the bone [102].

Unfortunately, the disparity in stiffness generated by these fixation strategies often requires a subsequent operation to rectify issues caused.

Described by various authors, biological / morphological fixation, the used of porous metallic implants, may provide an improved strategy as the stimulated bone ingrowth delivers a mechanical lock between the implant and bone [103].

As early as 1909, Greenfield devised the initial idea of biological fixation by designing a metal framework for a dental root implant, which facilitated bone growth to stabilise the implant. Currently there are 3 major types of porous implants, (i) porous coated solid implant, (ii) porous metal part attached to a solid implant, and (iii) a completely porous implant, and there is a wealth of research describing the details of porous coatings and full implants, beneficial for bone ingrowth in hip and knee replacement [104].

Figure 2.6 Titanium Bone Foams with different levels of porosity [108].

The demands for improving bone infiltration has been met more recently by the development of highly porous structures, that encourage cell growth and movement and facilitate nutrient and oxygen exchange [105,106]. An alternative solution was a metallic structure that contained both macropores, in the 200 - 500 μm range, which encourage bone ingrowth, and micropores, present in the low micrometer range, which are indicated to assist osteoconductivity [107,109]. The introduction of a novel liquid foaming method of Ti powder enabled to control the porosity during production and deliver an open network of large pores (100 - 400 μm), optimised for osteogenesis [108]. High porosity effectively overcomes the differences in stiffness between implant and bone by reducing the Elastic modulus of the implant [109]. Gibson and Ashby [124] show that an estimation of Elastic modulus, E*, is derived from the following:

$$\frac{E^*}{E_s} = \left(\frac{\rho^*}{\rho_s}\right)^2 \qquad (2.1)$$

Where the Elastic modulus of the solid part is designated by E_s, and p^*/p_s is the relative density of the porous foam.

The porosity, compressive strength and consequently the moduli of Ti foams are adjustable to generate a close fit with human bone. Adjustment between 50 – 80% porosity is possible and Ti foams prepared within the 60-65% range of porosity (9 -14 GPa) are aligned with human bone. Likewise, lower density porosity in Ti foams, in the 35–42% range achieve a compressive strength of 130 – 180 MPa, which is close to that of cortical bone [110], The structures, at micro and macro level, can be further adjusted to meet to needs of the requisite mechanical properties through control of porosity and 3D structural network [111]. It was found that encouraging ingrowth and growth of bone surrounding the implant minimises the

stress shielding effect, as the load is balanced across the implant and bone. Furthermore, the structure of the implant is maintained through the adjustment of porosity which fine-tunes the compressive strength and stiffness [112].

Porous Ti implants offer promising options for implantation, resulting from their inert, biocompatible nature, and good mechanical match with human bone. Interestingly it was found that while Ti foams are inert, surface treatments, including heat and chemicals, enable the stimulation of bone development when implanted at sites remote from exiting bone [113].

To summarise, there are multiple variables that must be considered and balanced prior to designing orthopaedic-suitable porous Ti implants, including porosity, pore size, network size, and mechanical functionality. It was defined that several methodologies for manufacture of porous Ti implants, including sintering titanium powder, the creep expansion method and the space holder method; however, production of Ti foams that meet the specific requirements noted previously, is not met by these traditional methods. Innovations in manufacturing are needed to address these issues, and the following section introduces a new method for production of porous Ti foams that meet the stringent parameters for natural bone [114-116].

2.10 Production of Porous Titanium via Powder Metallurgy

Powder metallurgy is used for creating porous titanium and titanium alloys . This section will briefly present the production methods used most often. These methods can be classified into five types: space holder method, loose powder sintering, gas entrapment techniques, replication method and electro discharge methods, and hollow sphere sintering [117].

The section below will examine the space holder method and the loose powder sintering.

The gas entrapment method involves introducing an inert gas into the system that involves metal powders which are under extensive pressure, followed by densifying them at high temperatures. In the process of densification, gas is trapped into the metal matrix. Once the densification process is completed, elevated temperatures are applied to the processed metal so that the metals' lowered mechanical strength at elevated temperatures expands the gas. As this process needs high temperatures as well as high pressure, it is difficult operate. In a study , they expanded argon gas for processing Ti_6Al_4V foams and compacted Ti_6Al_4V alloy

powders [117]. They also used an approximately 0.33 MPa pressure to fill argon gas into the mould and then the mould was welded. Then, the densification process was conducted in a press with 950°C and 100 MPa pressure. At an atmospheric pressure of 1030°C was applied during the experimentation. These processed foams not only were irregularly sized and shaped but also had an interconnected structure, including porosities as far as 52 vol. % [117].

The hollow sphere technique involves using preproduced hollow spheres to sinter the foams. Gas atomization techniques are utilised for creating hollow spheres. Then, special methods are used to melt the metal while blow gas using nozzles inside the viscous metal melt drops. In this process, the metal can be introduced to multiple polymeric or organic additives for increasing its viscosity, following which they must be burned. This technique can help in creating high porosities without the need for interconnection of pores.

The technique of replication can help in developing open cellular foam that is highly porous. For creating titanium foams, a sponge that is preconstructed is first immersed into metallic slurry and is then heated at various stages to dehydrate it so that the polymer is burned and sintering occurs. The metal slurry was shaped using polyurethane (PU) sponges and then gradually heated to 150°C, followed by 400°C, and then 500°C temperatures for removing PU. The, it was cooled down to room temperature and sintered by heating it to 1250°C.

It was also developed Ti foams using replication method along with porosities ranging between 20 and 35 vol. %. This method involves mixing Ti powder particles that are then compacted using a steel mesh. When the sintering of Ti-Fe is being formed, the eutectic phase hinders the diffusion of Fe because of Ti and following the electrochemical removal of steel mesh sintering from the foam. This procedure results in macropores homogenous distribution that are the same size of steel wire which the mesh uses [118].

2.10.1 Loose Powder Sintering

Porous structures are most easily developed using loose powder sintering. This method helps in creating foams that have low porosity levels. During this method, the sintering of metal powders takes place after they are inserted into a mould. Sintering time as well as temperature helps in controlling the pore size and characteristics indirectly. Further, it is possible to apply compaction methods to metal powder for reducing the porosity level through breaking the stable oxide layers and increasing contact area. Studies that have

examined aluminium foams have determined that sintering ratio is increased by ball milling of the powders prior to sintering [119]. The pores resulting from this method are irregularly sized and shaped. Figure 2.7 illustrates the process schematic description and pore shapes.
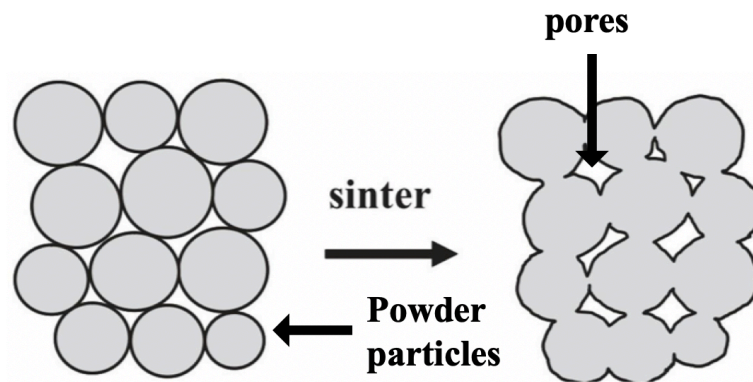
Figure 2.7 Schematically portrayed loose powder method.

Esen et al.'s study demonstrated that Ti-6Al-4V and titanium can foam until it reaches 40 vol. % porosity that can be created by utilising Ti-6Al-4V and Ti powders that have 107 μm and 74 μm average sizes, respectively. It was observed that the pores' geometry was irregular and ranged 10–100 μm in size. Moreover, it is possible to control the porosity amount and to change it through sintering temperature and time as well as powder characteristics [120].

2.10.2 Gas entrapment technique

This technique typically involves the elemental powders being compressed into a container in a compact form, and while pressing, an inert gas is trapped into compact. While heating, the internal pressure caused that the gas creates in the compact results in expansion. Hence, temperature equipment as well as high pressure is needed for this process along with two heat treatment steps: for bubble expansion and during powder compaction. Several studies regarding this subject have examined the development of titanium and titanium alloys that are highly porous and include isolated highly spherical pores utilised in aircraft industry [121]. Figure 2.8 illustrates the process' schematic representation.
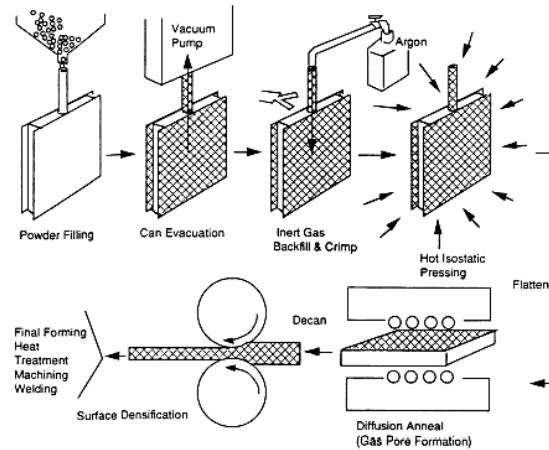
Figure 2.8 Schematically portrayed gas entrapment technique [23].

2.10.3 Sintering of Slurry Saturated Sponge (Replication Process)

A temporary support is used for developing metallic foams method that may include be an organic sponge-like material including polyurethane foams [122], a synthetic plastic or natural sponge [4], or NaCl's or NaF's sintered structures [121]. First, temporary support is immersed into slurry that has the desired metal powder, organic liquid, and water until saturation. To ensure that the organic support is pyrolysed, the saturated support is first dried and then heated. Once sintering is conducted, it produces substantially porous material whose porosity is interconnected. If the NaF or NaCl is used for support, following the sintering process, they are removed in water. Because of the low melting point, the salt patterns' use becomes limited leading to the manufacturing of only porous structures of aluminium as well as lower melting point alloys.
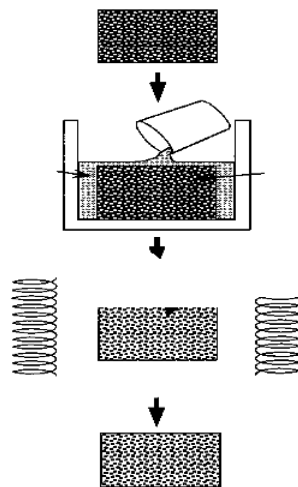
Figure 2.9 Schematically portrayed replication process method.

26

However, it is possible to use NaF at temperatures above 900°C. There are primarily three pore structure types in foams that this technique produces: primary pores on the hollow struts' surface, secondary porosity present at the hollow struts' core that was the brief support occupied previously, and finally, open tertiary porosity present between struts.

2.10.4 Metallic Hollow Spheres

This method includes obtaining highly porous structures through the bonding of metal hollow spheres using transient liquid phase sintering or sintering through powdered additive as well as hot isostatic pressing (HIP).

Gas-atomized hollow powders, coated Styrofoam spheres, coaxially sprayed slurries, or sintering and cementation can be used for creating hollow-sphered structures.

Foams that are made from the sintering of hollow spheres have uniform porosity size because of which they have predictable mechanical properties compared to other foams that have random porosity size. This technique also enables the foaming of a complete range of materials including superalloys, intermetallics, and titanium alloys.

2.10.5 Space Holder Method

It has been noted that the process of foam production described previously tend to lead to the foam structures becoming contaminated while pores are being created or to the induction of limited porosity levels that have pores with irregular shapes and varied distribution in size. However, space holder method refers to a simple method that can help resolve problems concerning foam production techniques.

In this process, the metallic powders are first combined with space holder powder along with binder so that all spacer surfaces are covered to ensure that the powders whose physical bonds are secure. Then, the mixture is cold compacted so that green body is provided with adequate strength while ensuring that the shape of the space holder powders is not disturbed [122]. The space holder material is slowly withdrawn from the compacts before sintering for the required foam strength. The water leaching method involves removing the spacer particles that are water soluble through the spacer particles' dissolution. However, evaporation while heating to sintering temperatures is used to eliminate spacer particles that are thermally removable. The final step involves sintering the leftover metallic skeleton at an approximate high temperature of 1300°C for titanium, considering protective atmosphere.

Figure 2.10 illustrates space holder methods' schematic representation. Sintering mainly aims to bond metallic powders and ensure that the porous body has specific mechanical strength.
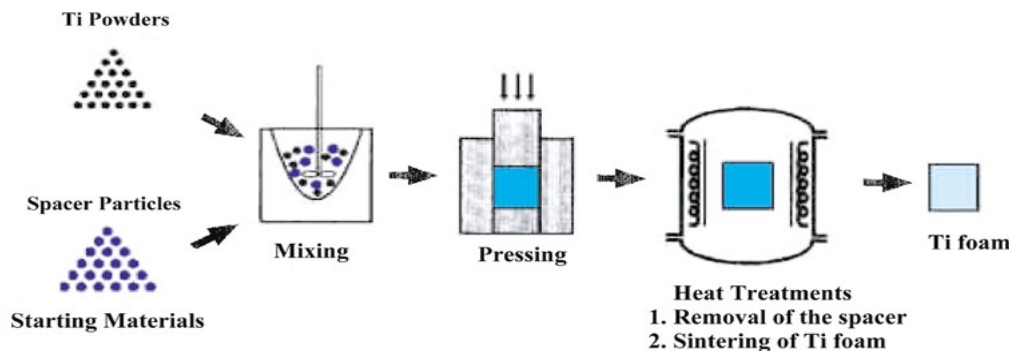
Figure 2.10 Schematically portrayed space holder method.

The spacer material's characteristic impacts the pores' size and morphology as well as the extent to which titanium is contaminated which is also crucial in identifying the resultant foams' structural and functional properties. For example, the spacer particle in biomedical applications must not contaminate the foam or leave a residue. Further, the pore size, porosity content, as well as distribution must be altered such that the foam becomes compatible with natural bone mechanically. It must include an open porous structure with the pore size ideally being approximately 200 μm so that body fluids can be transferred and there is adequate space for bone ingrowth.

The space holder method involves spacer particles being added in varying amounts which can control the porosity's size and distribution that typically ranges from 50 to 85 vol. % along with desired mechanical properties and interconnected porous structure [56,83]. On the other hand, to gain the targeted properties, the major criteria are selecting the most appropriate spacer particles. For creating pores in titanium and titanium allows, spacer particles that are thermally removable including ammonium hydrogen particle, polymer granules, carbamide (urea), as well as metallic materials have been used [123,124].

Researchers also developed titanium foam by using carbonate particles of ammonium hydrogen that were decomposed at 200°C, after which titanium skeleton's sintering was conducted at 1200°C for 2 hours. The subsequent Ti foams had 79% porosity, along with elastic moduli and compressive strength at approximately 5.3 GPa and 35 MPa, respectively. This is also close to the cancellous bone's mechanical properties. On the other hand, no in-depth explanation regarding titanium's contamination caused by ammonium hydrogen

carbonate evaporation is available [125].

However, Kennedy et al. [25] used polymer granules which evaporated at temperatures that were comparatively lower (130°C). Titanium scaffolds were obtained by sintering at 1100–1250°C that had tensile strength as well as elastic moduli ranging between 0.3 and 16 GPa and between 1.5 and 30 MPa, respectively. Micro porosities that were identified in the final structure of the foam, however, led to the mechanical attributes deterioration.

Hence, it is evident that spacer materials, apart from magnesium, can produce residue or interstitial elements such as hydrogen, nitrogen, and oxygen that are seen in spacers and can not only lead to titanium dissolving but also render titanium alloy foams of no utility in biomedical applications because of the degradation of mechanical properties. However, the dissolution rate of magnesium in titanium is limited as shown in Figure 2.11 while it is significantly susceptible to oxidation which ensures that, during foam manufacture, there is no extreme oxidation of titanium.
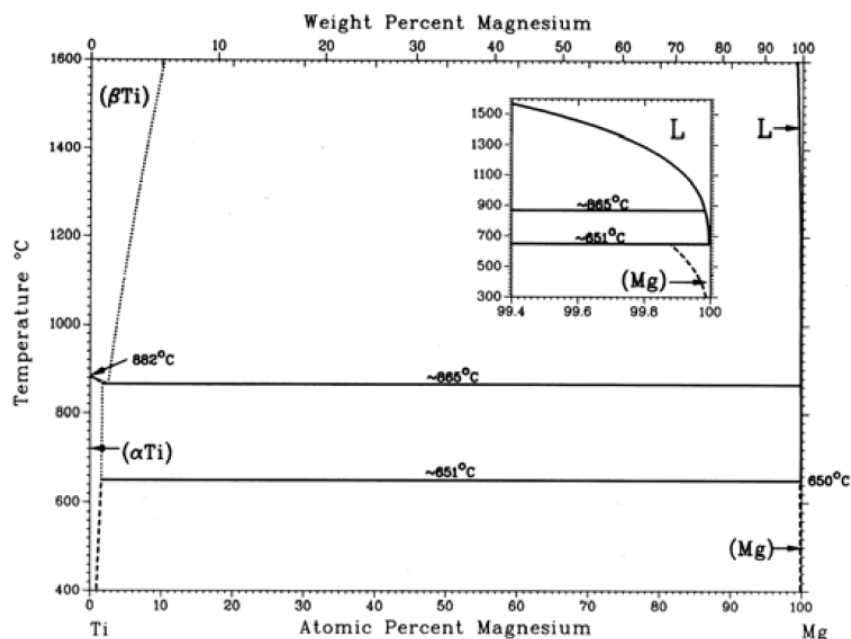
Figure 2.11 Titanium and Magnesium phase diagram

In a recent study, they produced Ti and Ti_6Al_4V alloy foams by first using magnesium powder. The study involved production of porous titanium through evaporating magnesium at 1000°C and then sintering it at 1400°C. The porosity content of the final products ranged from 25% to 82% with their mechanical properties being almost similar to that of cancellous bone [139].

In a study by Esen et al. [113], titanium foams were developed by using magnesium spacers. By slow heating to sintering temperature (1200°C), magnesium was removed from the Ti/Mg compacts. The interconnected open pores' contents that were gathered through magnesium evaporation ranged from 45 to 70%. The porous structures' relative elastic modulus was seen to reduce with the foams' increasing porosity properties. It was observed that elastic modulus as well as yield strength ranged from 0.42 to 8.8 GPa and from 115 to 116 MPa, respectively, and was the same as that of natural bone [113].

2.10.6 Reaction or Combustion Sintering

To generate the elemental powders' reaction, a compacted powder blend is heated, thus causing intermetallics to generate [126]. Then, sintering particle fusion is obtained through a considerably fast exothermic reaction resulting from the release of extensive amount of heat. At first, elemental powders that have predetermined quantities were combined and cold compacted, and then a laser beam, electric discharge, or electric heating under a controlled atmosphere is used to ignite the compact. After the compact is heated to adequately elevated temperature, it catches fire, and there is a significant exothermic reaction because of a combustion wave occurring in the entire mixture, with no need for added energy.

To produce porous nitinol (NiTo), several studies have been conducted. Because of the low exothermic characteristics (67 kJ/mol), before the ignition, a tungsten coil element is used to heat the powder mixture compact to 550°C. The porous compacts' general characteristic included the compact's pore channels developing along the combustion wave's propagation direction. The compact's final porosity is also influenced by the existence of transient liquid phase, the escape of adsorbed gases, and volatilization of impurities [127].

2.11 Mechanical Properties of Ti Foams

It is vital to determine the mechanical behaviour of metals used in biomedical structural situations where they are exposed to repeated cyclic loading and stresses, over extended times. The behaviour characteristic of metallic foams is dependent on the properties of the solid and the pore architecture, including the network structure, pore size and density. Sample weights are used to calculate relative densities and Imwinkelreid described the tensile yield strength of Ti foams with proportional densities of 0.38 [35]. The elasticity and density of the cell walls in this study were selected to be equivalent to those of solid titanium, 110 GPa and 4 g/cm^3 respectively [35].

For orthopaedic prosthetic applications, the tolerance of foam structures and knowledge of how they degrade in response to cyclical loading is vital [128]. Degradation standardly initiates by nucleation and crack formation at the cell face which advances to the edges. As strength declines, for a metal foam, the cell wall flexes in response to compressive strength and straightens under tensile mean strength, resulting in high ductility in compression situation and brittle fracture when under tension. One of the major benefits of metal foams s the substantial level of damage tolerance [129], meaning that a shift to brittle behaviour from ductile necessitates the presence of a significant crack, in the case of tension-tension fatigue or tensile loading.

The major focus of this study is to assess the most important aspects of biocompatible metal foams used in load bearing conditions, including stress-strain behaviour, fatigue crack development and fracture toughness. This work provides contemporary value as an innovative study investigating the fracture mechanics of the latest forms of high porosity Ti foams.

2.11.1 Uniaxial Stress-Strain Behaviour

Much of the research effort in assessing the mechanical properties of metallic implants for use in biomaterials has focused on aluminium foams [20, 25]. The stress vs. strain behaviour for porous Ti materials is defined by a significantly extended plateau, as seen in Figure 2.12. The plateau region represents compression of the foam in response to a large strain, with unchanging stress. When compression occurs at a level at which all of the cell walls collapse, the outcome is densification where the cell walls are touching. The result of densification is increased resistance to compressions which leads to increased stress.
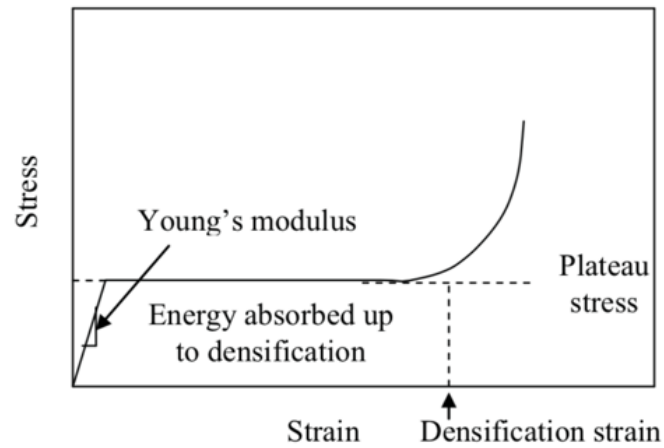
Figure 2.12 Stress vs. Strain behaviour of metallic foams

The Poisson ration and elastic modulus are used to define the linear elastic behaviour of open pore foams [130]. Distortion of high porosity metal foams, which by definition are low density, occurs by flexing of the cell wall. The impact of fundamental compression or extension of the cell wall is a function of the density, and can be increased by a corresponding increase in density [69]. Alternatively, in closed cell foams, the effect of the cell wall stiffness impacts on the elastic modulus, this is a result of the bending and / or contraction of the cell edges as the cell face is stretched [89]. Figure 2.13 represents the cell edge bending during deformation in a simple cube [34]. When a uniaxial stress is exerted on an open cell foam, the force (F) is transmitted by each cell edge, which results in the edges bending. The equation that defines the Young's modulus calculation in this situation is below (Equation 2.2) [45]:

$$E_f = \frac{\sigma}{\epsilon} = \frac{C\, E_s\, I}{l^4} \qquad (2.2)$$

The stress-strain response of metal foams prepared from other metals has been investigated, specifically Wang et al. defied the mechanical characteristics of a porous tantalum, which generated an open cell structure by application of a infiltration methodology and carbon vapor deposition [131]. The prepared tantalum foam showed high porosity and a low elastic modulus, in combination with the good bio-compatibility and activity reported for this metal. Furthermore, the researchers demonstrated the presence of an apatite coating which mimics a bone layer and facilitates both soft tissue attachment and bone in-growth.
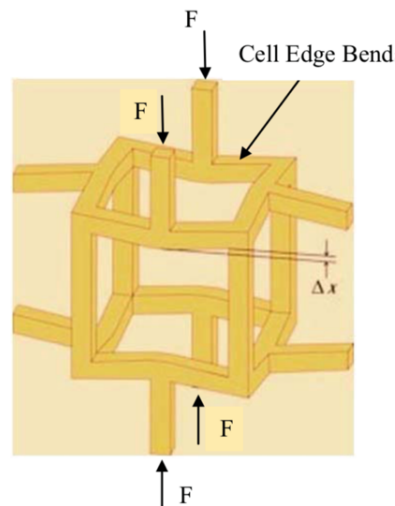
Figure 2.13 Cell behaviour of metallic foams under compression

Adopting the use of laser-engineering net shaping (LENS) to produce Ti foam designed with moderate stiffness specifically for application in high load bearing situations, Xie et al. discovered that this process was suitable for production of titanium foams of porosities up to 70%, facilitating the manufacture of complex shapes for implantation. The foams produced with porosities between 35 – 42% exhibited modulus and strength that equates to that of cortical bone [134].

Behaviour of 17-4PH stainless steels in stress vs. strain curves have been assessed to compare data with theoretic analysis [136]. When comparing the data with literature findings on metal, polymers and experimental deformation foam models, the normalised outputs, in terms of elastic modulus, compressive yield strength and shear modulus shown a similar magnitude to the literature data. Overall, 17-4PH foam densification strains are recorded as lower than polymeric foams, a consequence of the ridged cell wall [136].

The body of literature investigating the mechanical characteristics of foams produced by

titanium powder metallurgy is scant, with the work of Imwinkelried [51] representing just one of the few studies in this area of analysis of porosity in different titanium foams. More recently, Xiong et al. published a work that described the impact of pore size on the tensile behaviour of porous Ti foams [68], and Singh et al., exploited advances in micro-ct and FEM modelling to prepare a publication that defines the elastic-plastic deformation characteristic of Ti foams [69].

The initial aim of this study was to determine the stress vs. strain characteristic of pure Ti foams, drawing comparison with existing literature where applicable. Later, this work extends in to the investigation of the mechanics of fatigue and failure in the foams.

2.11.2 Previous Work on Ti Foam Uniaxial Compression Tests

The compression behaviour of Ti foams of differing porosities and manufacture have been widely reported in the literature. The titanium foam produced by Davis et al., using the hot-isostatic press method, exhibited largely similar behaviours as foams produced by alternate means. In summary, they observed linear elasticity, which is followed by a plateau representing deformation and plastic collapse, and ultimately a rapid increase in stress which results for the densification of the foam. Assessing 316L stainless steel foams with porosities of 40, 46 and 50% and corresponding compression strengths of 20, 25 and 32 MPa respectively, Bram et al. found broadly similar mechanical characteristics. Once again, the curves produced by Bram's team exhibited the same three regions as previously described, namely elastic deformation, long plateau representing deformation, and the final densification stage [22].

Investigating microporous titanium foams, produced with 50% porosity via super plasticity expansion with high pressure argon gas in the HIPing method [52]. These researchers interrogated two products, a 19% round pore titanium and a 41% elongated pore titanium, and the respective stress-strain curves which generated moduli of 30 GPa and 41 GPa. The outcomes of this research are notable as substantially different to those found by Thelen et al. with closed porosities; however, the contrast may be described by the alternate manufacturing methods applied.

Comparing predicted modulus values from 2D and 3D simulation FEM models with stress-strain response to compression testing on a 15% porous titanium foam, showed relatively close agreement between the 3D simulation and the experimental situation, producing 81.4

GPa and 78 GPa values, respectively. However, the predicted plastic response from the 2D model generated values substantially lower than the recorded experimental outcomes [46].

Given the variation observed in the literature reports of Young's modulus values for multiple porous titanium foams, including a value of 5 GPa for 50% porosity in a titanium produced by a superplastic foaming method [46], 4.7 GPa for a product manufactured by a plasma spray method [120], and the values of 38 GPa and 41 GPa, determined by Daudt et al. for their 40% porosity titanium foams, it is clear to see that the choice of manufacturing method is critical to the final porosity of the titanium foam.

Compression of unidirectional freeze cast and water-evaporated titanium foams, which produced foams containing 60% elongated pores and lower than 45 μm powder, recorded strengths of 40-60 MPa [72].

Testing titanium foams produced by PU-replication or gel casting, produced foams with compression strengths of 65, 46 and 30 MPa, and modulus values of 2.8, 1.8 and 1.2 GPa, for porosities of 71, 73 and 76%, respectively [136]. Once again, we observe disparity in compression strength of high porosity titanium foams, similar to that seen previously in the work of Chino and Dunand et al. [32], which is likely a consequence of the manufacturing methods.

To standardise the data, we have chosen to use the powdered metallurgy method that has been previously tested by other groups, including Imwinkelried, who produced titanium foams by compression of metal powder between carbide plates, including, in some cases, experimental unloading and reloading of the parts. Elastic modulus, defined by linear regression of the linear portion of the stress vs. strain curve produced a value of 9GPa, and a corresponding yield strength of 67.7 MPa, for a 62.5% porous titanium foam [51].

Imwinkelried and Wen et al. used the same spacer for their metallurgy, specifically, ammonium carbonate, with combined averages showing the plateaus stress of titanium foams as 35 MPa [34] and elastic modulus as 5.3 GPa. The study of Wen et al. investigated compression of Ti foams with modarate densification of c. 60%; however, they report that the dense status and porosity of the Ti foams affect the mechanical attributes of the porous Ti structures[4].

Wen et al. directly compared compression mechanics of two 63% porous titanium foams

with pore size ranging from 200 to 500 μm, one with an exterior shell of 70% porous material and the other with no outer shell. The outer shell encased foam produced peak stress and Young's modulus values similar to that of human bone, that is, 152 MPa and 4 GPa, respectively. While the Young's modulus of the unshelled structure was the same in comparison to the shell-covered foam, at 4 GPa, the peak stress was lower at 109 MPa [4].

Using magnesium as an alternative space holder, Esen and Bor produced stress-strain curves for titanium foams across a range of porosities from 45 – 70%. The yield strength and elastic moduli are reported as 15-117 MPa and 0.43-8.9 GPa, respectively. Others have conducted similar compression tests on titanium foams with low porosity, and Lefebvre et al. report an elastic modulus of 15.3 GPa [15].

Assessing the outcomes of compression testing of 60% titanium foams produced by the same manufacturing methodology, exhibits widely varying results. For example, Imwinkelried reports yield strength of 67.7, while studies by Wen et al. firstly report 35 MPa and then 109 MPa. We conclude that not only is the manufacturing method critical to the mechanical properties of the titanium foam, but other aspects, including environmental conditions, powder size and spacer type may all contribute to the observed variations.

2.12 Finite Element Method of Titanium Foam Materials

Predictions, based on an approximate response of a continuous complex shape, which is split into geometrically straightforward areas of specific size that can be analytically defined, termed Finite Elements, are beneficial for determining the response of both fluids and structures. The FE models can be applied to a significant number of procedures to predict the elastic or inelastic behaviours and the static or dynamic response of a substance [46].

As a consequence of their advanced ability to model complex materials and define structural behaviours, FE methods are used extensively to predict the mechanics of cellular materials. The modelling and simulation methods of cellular products are the focus of the current section within this study.

Viewed at a microscopic level, cellular materials comprise of a skeleton of solid material which is encased with gaseous or liquid material. Individual cell sizes range from 100 μm to several millimetres, generally only a fraction of the overall component size. Standardly, cellular material exhibits low relative density, which is defined by division of the average

relative density, p*, of the cellular material, by the density, ps, of the solid materials that make up the cell wall and struts:

$$\rho_{\mathrm{rel}} = \frac{\rho^*}{\rho_{\mathrm{S}}} \qquad (2.3)$$

Cellular materials generally comprise of only a few percentage points of the solid volume fraction, and are standardly described by their low relative density; however, for compounds with greater relative densities, porosity-based descriptors are considered to be more apt.

The use of cellular materials is advantageous as a result of the high stiffness and strength mechanics that are directly associated with their weight. Furthermore, the benefits extend beyond the weigh-specific mechanical aspects to multiple applications, including, for fluid-permeable cellular material, heat exchange, and catalytic conversion, and insulation and buoyance aids for closed cell applications [138] .

Cellular materials, including wood, sponge, trabecular bone and cork are found in substantial number in the natural world, thought to have evolved as a result of competition. A complete undersigning of the properties of naturally occurring cellular material is critical to benefit and inform deigns of compatible biomaterials for orthopaedic uses. Gibson et al. [122], provided a comprehensive review of bio-mechanical properties of cellular solids, with focusing attention on wood cells, and general reviews of the mechanics of cellular materials found in Gibson et al. [122] and Gibson and Ashby et al. [123].

The array of available polymeric, metallic and ceramic foams demonstrates the significance of open- and closed-cell materials for engineering purposes. In addition to provision of materials with stochastic micro-structures, novel production methods, for example rapid prototyping, supply the potential to produce and assemble geometrically and period controlled micro-structures.

The major aim of this study focuses on Finite Element (FE) models for the micro-structure of man-made cellular materials, including titanium foams. Set up methodologies are described, and the micro-mechanical length scale, that is the transition between struts and cell walls, and the length scale of the entire component, produced from, or containing foam

are explained in detail. The majority of the provided information focuses on micro-mechanical topics, the final section touches on optimising the density distribution in components produced from a functionally graded foam; a specific macro-mechanical problem.

2.12.1 Homogenization and the Unit Cell Method

Microscopic assessment of the observed or predicted mechanical behaviours of individual struts and cell walls is a prerequisite to determining the physical behaviours of the structure at a macroscopic level, where it is considered to be a homogenous pseudo structure, as opposed to a discrete structure, is termed homogenisation. The process of homogenisation as described here is used to deduce the amount of motions of freedom in the mechanical model from innumerable displacements and rotations caused by individual micro-structures to a more convenient number of macroscopic displacements and rotations.

There are two main situations that are appropriate for homogenisation from the micro-scale to macro-scale to determine the mechanical behaviour of the microstructure [139]. Firstly, the mean field approach, a micro-geometric statistical analysis, which relies on estimates for the properties of the materials with a minimal numerical input as they largely depend on analytical interactions. This process is used to define the physical field variables at a microscopic level purely by assessment of volume averages of the individual components.

Secondly, the discrete microfield approach applies analytical or numerical methods to fully resolve the physical fields at the microscopic level, by predicting the specific behaviour of the micro-structure at the required level of detail.

Assessed by Li et al., mean field and Hashin-Shtrikman type methods, considered important in small pore volume fraction material, are used in a limited manner for cellular materials [140]. The Hashin-Shtrikman method can be determined by assigning a vanishing stiffness to the void phase, when determining the upper limits of the elastic modulus for macroscopic isotropic cellular materials. Standardly, the predicted elastic moduli of foams are significantly lower than these upper limits, and the lower limits do not provide beneficial data as they decrease to a meaningless level.

Given the limitations of mean field methods, cellular materials micro-mechanical behaviour predictions are preferentially studied using discrete micro-geometrical models.

For micro-mechanical modelling, cellular metal materials are standardly defined by one of two groupings, specifically open- or closed-cell materials. Open-cell materials are largely permeable and comprise of a solid scaffold of beam-like structures. Whereas, closed-cell materials are formed by interconnected cell walls, and are generally impermeable to fluids, although this is dependent on the porosity of the cell wall.

The elastic range of cellular material is generally restricted, and the resulting mechanical characteristics is largely a result of microscopic deformations, such as bent or fractured struts and cell walls, or formation of yield joints and folds. The mechanisms causing deformation are led by the micro-geometry which, in the solid, is vastly complex and significantly irregular. The actual micro-geometry must be dramatically simplified and idealised prior to application of analytical methods that describe the behaviour. As an example, beam theory had been used with a degree of success for open-cell foams; however, the limits of these methods are quickly reached, and therefore, the majority of generic micro-geometries have been further defined by numerical methods. Resulting from its robustness and large range of applicability, the finite element method is the most widely used numerical tool.

There are a number of controlling principles for micro-mechanical finite model that represent the micro-structure materials:

Representative of a real foam sample with the highest level of accuracy possible, considering the available computational access, a multi-cell model of finite samples aims to predict the behaviour of a real sample under possible loading conditions. In the majority of situations, the loading would correspond to uniaxial compression. This model facilitates comparison between the experimental data and the modelled data. This type of model may be beneficial in modelling the effect of boundary conditions on adjacent surfaces, which may be impacted in different ways. Indeed, the boundary layer may behave in a completely alternative manner to the rest of the sample which may result in a behaviour effect that is related to the number of cells per sample.

Unit cells standardly comprise of regular, structured set up of a restricted number of base cells, which are subjected to detailed modelling. Assessing both the un-deformed and deformed states, geometrical periodicity and periodicity boundary situations guarantee the unit cell spacing. This method is especially suited to determining the effect of changing geometrical parameters on mechanical behaviour. In the case of unit cells displaying random

39

cell geometry, application of one periodic constraint is beneficial as, based on the boundary conditions, it results in the optimal prediction of the mechanical response of a random but periodic, infinite material.

A hybrid model, the embedded-cell model comprises of a micro-geometrically fully resolved core that closely resembles the periodic unit cell model and is fixed within a material matrix. The behaviour of this model reflects the effective behaviour of the embedded cell. This facilitates investigation of micro-mechanical functions in partial sections of a component, eradicating the requirement to model the entirety.

The array of modelling strategies discussed herein, which have fully defined parallels in continuum micro-mechanics of composites, provide detail on the local deformation characteristics and the associated behaviours of the entire material, derived via homogenisation.

The following section, interrogates the periodic unit-cell in greater detail. This idea is based on the theory that the behaviour exhibited by an infinite periodic structure can be approximately represented by a finite sized model. Combining geometrical-representations ('building bocks'), which facilitate seamless, periodic tiling of space, and suitable boundary conditions, which guarantee the periodicity of the structure's displacement field. The original unit-cell is repositioned along linear combinations of the vectors of periodicity, to derive the representation of the space-filling structure. Standardly, two and three vectors of periodicity are needed for accurate descriptions of periodic 2 and 3 dimensional structures, respectively.

Coupling to kinematic constraints is necessary for assessment of mechanical issues relating to the displacement of the boundary points of the unit cell. The boundary points are mapped along a linear combination of integers and multiplies the vectors of periodicity.

The geometries of unit-cell models are highly idealized, particularly when compared to the geometrical complexities and irregularities of physical cellular materials.

Defining the periodicity boundary conditions of a rectangular unit-cell for displacement field is described below. Figure 2.14 depicts an originally rectangular 2D cell unit both in its un-deformed and deformed configurations. Using the first letter of the four cardinal directions, the four boundary edges of the unit cell are coded N, S, W and E, with the adjacent corners labelled NW, SW, NE, and SE.
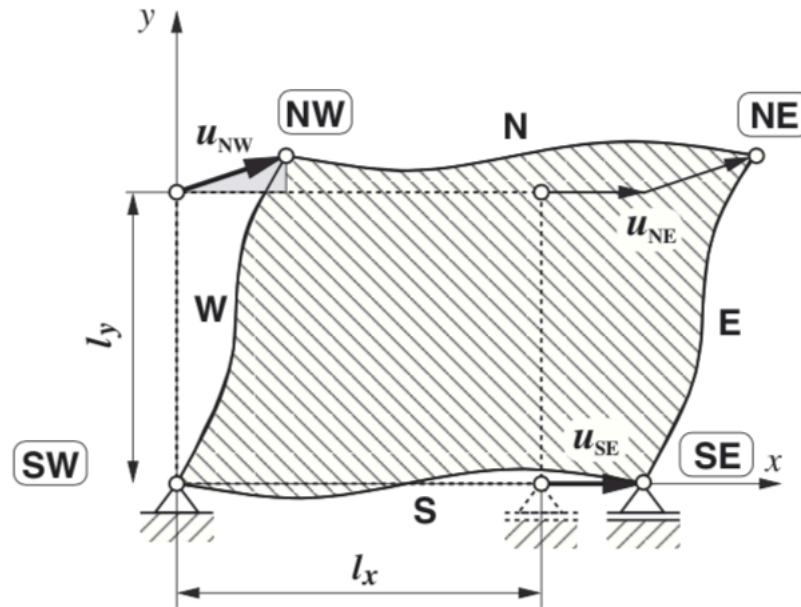
Figure 2.14. Idealized 2/D unit cell in the undeformed and a deformed configuration.

It is important to protect the unit-cell against rigid body movement modes [142].

As shown in figure 2.14, the corner node defined by NW / SW and its associated translational degrees-of-freedom are restricted to inhibit rigid body translations. Furthermore, the vertical displacement aspect of the finite element node (SE) is also restricted to inhibit rigid body rotation.

While the rigid body movements are prevented by application of these constrains, deformation of the unit occurs whilst maintaining the geometric periodicity conditions as a consequence of horizontal or vertical elongation, or as a result of a shear-like mode. The specific finite element nodes, termed master nodes, and include NW and SE, are relatable to the deformation modes of selected displacement components. In figure 2.14, the contribution of the master nodes to the deformation filed of the unit cell are shown by bold arrows.

Displacement of opposite boundary edges are coupled in the deformed state of a rectangular

unit cell, a prerequisite in maintaining the geometric periodicity. The degrees of freedom, 'master' DOF, associated with the coupled edges are unconstrained. The opposite edge of the unit cell is termed the 'slave' edge, and are partnered with a node on the master edge via their displacement vectors. Furthermore, an extra displacement vector is superimposed on the displacement field of the slave nodes. Overall, the displacement vector is associated with the macroscopic DOT of the unit cell. Then the components of these displacement 'vectors are related to the macroscopic strain tensor, which is described in vector notation by the vector of its components:

$$\varepsilon_{xx} = \frac{u_{SE}}{l_x}, \quad \varepsilon_{yy} = \frac{v_{NW}}{l_y}, \quad \gamma_{xy} = \frac{u_{NW}}{l_y}, \qquad (2.5, 2.6, 2.7)$$

The suggested master and slave relationship given here is not the only option, indeed the mater DOF can be derived from any suitable DOF in the finite element model, even if it does not correspond to a node in the unit cell. If this was not the case, automated generation for periodicity boundary would be certain to fail when no corner finite element nodes are available in the unit cell.

Slave edge and slave corner node coupling conditions require individual definition. In the descried 2D set up, displacement of the SW and SE nodes are fully and vertically constrained, respectively. This is to prevent rigid body translation (SW) and rigid body rotation (SE). The horizontal DOF associated with the SE node is associated with the macroscopic normal strain in the << direction, and both displacement directions, horizontal and vertical, of the SW node define the macroscopic shear- and normal-strain in the y direction. While S and W are unconstrained, the displacements of the slave edges, N and E are defined by the coupling equations:

$$\boldsymbol{u}_E(y) = \boldsymbol{u}_W(y) + \boldsymbol{u}_{SE} \qquad (2.8)$$

$$\boldsymbol{u}_N(x) = \boldsymbol{u}_S(x) + \boldsymbol{u}_{NW} \qquad (2.9)$$

Conversely, the displacement vector of the NE corner node is a simple linear addition of the master nodes' (NW and SE) displacement vectors, u_{NW} and u_{SE}:

$$u_{NE} = u_{NW} + u_{SE} \tag{2.10}$$

For finite element models incorporating structural elements that exhibit rotational DOFs, such as beams and shells, further coupling equations are needed. In the example case, the rotational DOFs for all corner nodes are constrained to endure uniformity:

$$\varphi_{NW} = \varphi_{NE} = \varphi_{SE} = \varphi_{SW} \tag{2.11}$$

In this case DOF Y_{SW} operates as the master for rotational DOF for the four corners of the unit-cell, and consequently the opposing edges' DOF are coupled as follows:

$$\varphi_E(y) = \varphi_W(y), \quad \varphi_N(x) = \varphi_S(x) \tag{2.12}$$

Slave node displacements from all edge nodes on the boundary are coupe to an individual master DOF, this means that the forces impacting on the master DOFs are then distributed across the entire edge that follows the mater DOF's movements. Therefore, the sum of the slave edge tractions is equivalent to the force acting on the mater DOF. Similarly, the forces at the constrained DOFs which enforce static equilibrium are equal to the sum of the master edge surface traction vectors.

On this basis, the unit-cell model responds to concentrated loads on the master DOFs in the same manner as an infinite periodic structure would respond to homogenised applied stresses. Derived from this, operates between the homogenised stress state, the concentrated horizontal and vertical node forces H and V, this relationship is dependent on the side lengths J and I of the rectangular unit cell, which are nominal stress components, or engineering-based stress measures:

$$\sigma_{xx} = \frac{H_{SE}}{l_y}, \quad \sigma_{yy} = \frac{V_{NW}}{l_x}, \quad \sigma_{xy} = \frac{H_{NW}}{l_x}, \tag{2.13, 2.14, 2.15}$$

Further elaboration to nonlinear stress measures in the large strain area is uncomplicated and required incorporation of the actual side lengths.
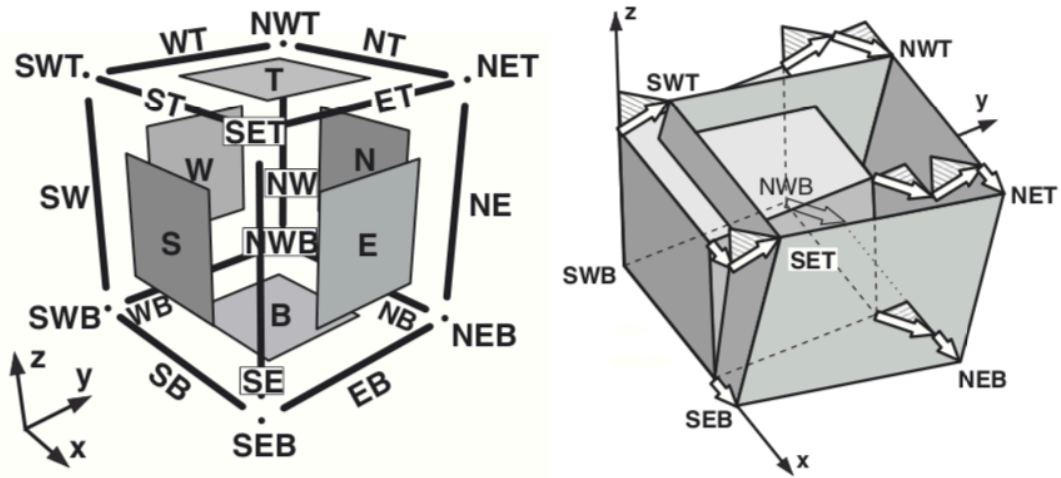
Figure 2.15. Default identifiers for the node sets on the unit cell cube (left) and general deformation state of the 3D unit cube (right).

The description of the 2D unit-cell can be extended to the 3D situation. Figure 2.15 (left) depicts the convention for naming of corners, edges and faces of the cube-like unit cell, and top and bottom are used for the third special dimension. In brief, single letters identify faces, double letters, edges and three show vertices. On the right of figure 2.15, we see the cube-like 3D unit cell depicted in a state of general macroscopic deformation, where three normal and three shear deforming DOFs are active.

Involving three independent DOFs, the associated constraint equation, which is the most complex possible can be determined for the z-displacement U_{NET} for the corner NEL:

$$u_{NET} = u_{SEB} + u_{NWB} + u_{SWT} \tag{2.16}$$

Figure 2.16 depicts the application of proposed kinematic boundary conditions to a multi-celled 3D unit cell model, that is containing tetrahedral topology. Figure 2.16 (left) depicts the predicted deformed situation, following uniaxial y-axis compression.
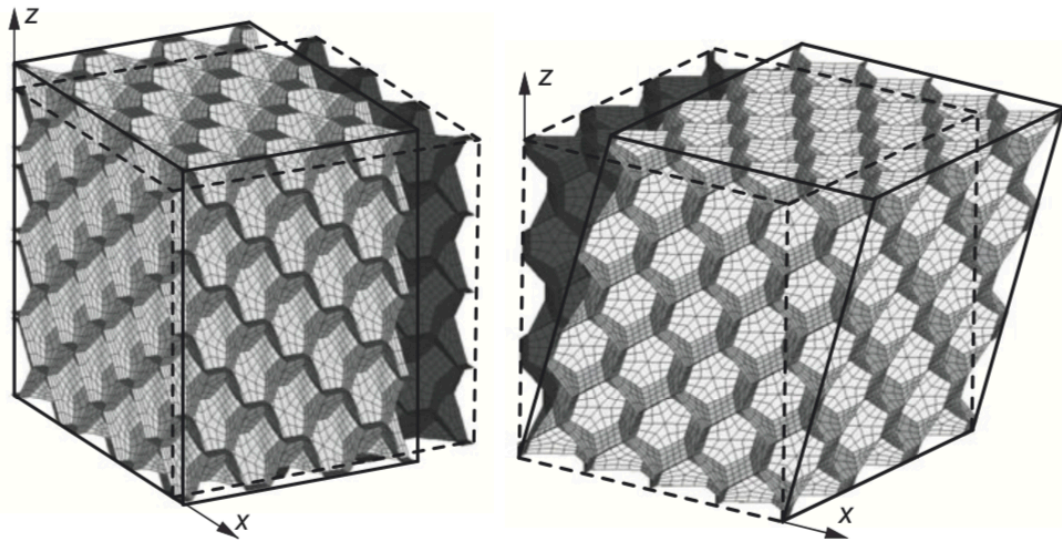
Figure 2.16 The deformed configurations for uniaxial compression (left) and combined shear (right) are shown

Undeformed elements are shaded dark grey and surrounded by dashed lines, while the deformed cube is light grey and surrounded by a solid line, and clearly demonstrates the Poisson effect. After subjecting to macroscopic shear loading, the resulting deformed set up is shown in figure 2.16 (right). Furthermore, the periodicity boundary conditions confirm that Roth deformation, uniaxial deformation and shear deformation are all handled appropriately. In figure 2.16, the predicted placements were scaled for plotting from the original finite element analysis.

Given that the unit cell model is not only a representation of regular, geometrically periodic micro-structure, but is necessary for determination of random, irregular materials, it is vital to consider how many cells are required for a unit cell to be truly representative of a complex micro-structure [48]. This contentious question, requires statistical intervention to deliver an answer. For example, it may use the maximum allowable standard deviation of a specific situation evaluates a defined series of unit cells. It is rather obvious that inclusion of as many cells as practicable while ensuring adequate detail for individual cells is the optimal situation; however, the balance of this is undefined.

The periodicities of unit cell models are critical and must be maintained during design.

However, it is important to remember that some occurrences, such as localised strain resulting from the collapse of weak cell layer or crack propagation are not stringently periodic in all directions. Densification of cellular material is always defined as periodic in unit cell models, and the collapse of a single cell layer necessitates simultaneous collapse in multiple layers in the period cell model, which is contrary to the real situation in the majority of examples. Tailored mathematical methods are applied in situations where the length of buckling modes are closely dependent on the size of a periodic cell unit. In addition, single crack tips cannot be managed by periodic micro-geometries.

2.12.2 X-Ray Microtomography (µCT)

Structural characteristics, including pore morphology and interconnection sizes, porosity, shape, distribution and surface roughness all impact mechanical performance and key cell growth parameters such as attachment and proliferation, as well as nutrient exchange, angiogenesis and bone ingrowth. Characterisation of these specific properties is critical to ensure optimisation of implant design.

X-ray computed tomography, (µCT), is a non-destructive technique to accurately determine the internal 3D micro-structure of an object [86]. Furthermore, as shown by Ran et al. [86], this method provides and outstanding level of visual differentiation between bone and soft tissue and can be used across multiple applications to image porous materials. The development of 3D image processing algorithms and analysis techniques in combination with the µCT images facilitates the quantitative description of complex, porous 3D structures.

µCT is based on the premise that x-rays, a form of electromagnetic radiation are attenuated as they pass through an object. The level of attenuation of x-rays on passage through an object are a function of the object's composition and the energy associated with the x-ray source. In CT imaging, when the x-rays meet the object, the resulting photoelectric effect is what generates the attenuate signal. The relationship between unattenuated x-ray and post exposure to the object is defined by:

$$I = I_0 e^{\left(-\frac{\mu}{\rho}\right)\rho x} \tag{2.17}$$

Where I_0 is the unattenuated X-ray power, I is the X-ray power after going through the object with a thickness, x. Varying along the beam, the linear attenuation coefficient is an energy-dependent material constant, μ, dependent on both mass density of the specimen and the incidental photon intensity.

For a monochromatic X-ray source, the linear attenuation coefficient is proportional to the material density, which is the basis of μCT imaging providing variable densities based on differing intensities. The ability of the material to attenuate the X-ray, per unit mass, (the mass attenuation coefficient) is described by division of the linear attenuation coefficient with the material density (ρ).

As dx is a limitlessly small augmentation, (μ/ρ) ρ is dealt with as a steady, assigned μ. Including the additions of lessening along the X-beam spread course determines the Beer-Lambert Law, an increasingly broad type of Equation 2.18:

$$\frac{dI}{I} = -\frac{\mu}{\rho}\rho dx \tag{2.18}$$

where $\mu(s)$ is the straight ingestion coefficient at position, s, along the X-beams. Hence, as characterized by Müller [34], a X-beam radiograph speaks to an image of the grouping of every constriction along the X-beam bar.

Rewriting the above equation leads to:

$$\int \mu(s)d\boldsymbol{s} = \ln\left(\frac{I_0}{I}\right) \tag{2.19}$$

This represents the explicit issue with computed tomography, that is the difficulty of assigning the real value of μ to each location, based on only the knowledge of the line integral values. To overcome this, many different potential measures (s) of I_0/I are required to adequately calcite the volume of the object.

CT collates multiple 2D radiographs whilst rotating the sample around a single axis in tiny increments of less than 1 degree. Using a filtered back-projection algorithm, the 3D volume

image is numerically built from the 2D radiographs to provide a complete 360 degree image set.

µCT picture quality is compelled by the X-beam vitality/power, X-beam center size, the extent of the finder and the article being examined.

µCT frameworks utilize two principle kinds of X-beam sources: synchrotron parallel radiation and Micro/Nano centre X-beam tube head. Standardly, research facility based µCT utilize the Micro/Nano centre X-beam tube heads which produce polychromatic X-beams. As the X-beam separates from the cone-formed source, just the regions of the item which are inside the pillar for the aggregate of the turns are utilized to reproduce the last pictures. A cone shaft framework utilized in lab-based µCT is represented in Figure 2.17.
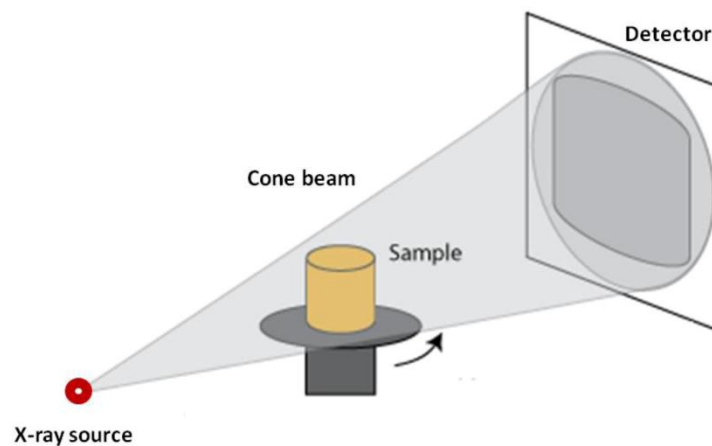
Figure 2.17 Schematic Representation of micro-CT scanning system.

Polychromatic X-beams are inclined to "beam solidifying", which happens because of the favoured retention of low vitality X-beams, which produces a higher mean vitality move esteem (beam solidifies) at the X-beam goes through the material. Streaks may be visible and the image will have brighter edges than in the central areas. A thin layer of metal can act as a filter to remove the low energy photons before they enter the object [34]. CT images are also prone to ring artefacts which can result from small specks of dust on the detector of individual defective pixels. The pixel issue can be overcome by replacing the defect with the average value of the neighbouring pixels.

Magnification of the beam of the CT can be manipulated by altering the location of the object. However, to ensure optimal resolution, attention must be paid to the X-ray focal spot size [102], where the smaller spot sizes produce higher resolution. However, the use of small

spot size may confound the intensity as it limits the X-ray energy that is applied. A need for higher X-ray energy requires a compromise of accepting a point of blur on the image.

Furthermore, detector and sample size also impact on the CT image quality, with the amount of pixels in the detector determining the total image resolution, while the maximum nominal resolution is directly associated with sample size. To ensure accuracy in image reconstruction, the object should not be greater than the field of view.

Using CT to characterise materials is finding use across multiple research areas, including bone structure characterisation [146], geomaterials and metal solidification. Recent innovations in tissue engineering have demonstrated the capabilities of combining CT with up-to-the-minute image resolution techniques to characterise scaffolds [144,145,146]. μCT outputs may be used for the accurate determination of both pore volume and interconnect area, as well as the internal structure. Many authors have demonstrated the application of μCT image information for computational fluid dynamics(CFD) and finite element models(FEM) for modelling [46,48]. This thesis exploits μCT 3D image assessment to investigate the mechanical properties of titanium-based structures.

2.12.3 Finite Element (FE) Modelling – Compression Test

Finite element analysis, which delivers comprehensive information of changes to structure under mechanical load, is a viable method for accurate evaluation of the impact of microstructure on the mechanical response of porous materials to compression.

Several researchers have investigated local failure and deformation of cancellous bone when load bearing, using FEA based CT imaging [86,143]. Similarly, Tanwongwan et al. produced 3D finite element models of human cancellous and compact bone to simulate loading conditions, showing that the predicted values for and compressive yield strength and elastic modulus at the point of fracture were close to the experimental findings, suggesting that FEA is a potentially, accurate method for investigating stress concentrations and failure processes [46]. Both 2-and 3D FEA simulations have demonstrated advantages when compared to experimental conditions and analytical methods, like the Gibson and Ashby's model [123].

The computerised model minimises experimental error and is capable of analysing the same model under a variety of loading situations. Analytically, the FEA model provides individual element analysis, so there is no requirement to assume that a single unit cell is representative

of the entire structure. Some studies indicate that this model is appropriate for delivering approximations of localised stress and strain. Thelen et al. [65] simulated three variants of porosity, smooth, elongated and representative pores, to determine the impact of morphology of the pore structure on the Young's modulus of a porous titanium scaffold, using 2D FEA. Results indicated that changing pore structure under deformation increased the elastic modulus in the elongation direction, and a doubling of Young's modulus in the structure of bone ingrowth. While these results are interesting, it is important to recognise the limitations caused by the two dimensional nature of the simulation.

Ryan et al. [43] conducted 3D FEA uniaxial compression simulations on Ti scaffold with a repeating cell unit, using a commercial FEA software, ABAQUSTM. Testing three scaffolds of varying porosity (51.3 – 66.9%) were compered in 2 seperate models – one unit cell and sizable macroscopic volume. Applying a nominal strain of 0.02 resulted in higher porosity samples exhibiting lower Young's modulus values and yield strengths in both transverse and axial direction. As a result of the homogenous nature of the structure, the differences between the single cell and macroscopic volume models were minimal. However, there were notable differences in plastic strain concentration locations in the failure modes applied along both axes. Lopez et al. conducted 3D simulations of vertical uniaxial compressions with axial strain of 0.01, using COSMOL Multiphysics^{TM}, using polycarbonate scaffolds with a porosity range of 51 to 81% [146]. They found agreement between the model and the experimental situation, with a percentage error noted at 30%.

2.13 Final Remarks

This section has shown that there is scant evidence on the mechanical attributes, and specifically the fracture mechanics of porous Ti structures for biomedical applications. It is therefore vital to further explore the impact tolerance of this material and determine their morphology, to inform the assessment of key characteristics of the foam's response. While recent years have seen substantial improvement in metal foam manufacture, titanium foams remain prone to imperfections and defects. Understanding the effect of loading on these foams, if we desire to apply them to structural solutions, including knee and implants, it is critical. Having identified a gap in the literature with respect to the mechanics of titanium foams, this major focus of this body of work is the mechanical behaviours of these porous materials and determining advancement strategies for improving the mechanical and material attributes of the foams. The accompanying sections present a point by point

clarification of the experimental and numerical examination led in this work so as to fill the gaps in the present body of literature.

3. EXPERIMENTAL PROCEDURE

3.1   Preparation of scaffolds

In order to produce porous titanium scaffolds, the powder metallurgy method was employed. The porous structure was limited by altering the ratio of magnesium to titanium powder used. The main matrix used Ti powder (> 99% purity (ASTM 1580-1)) with an average particle size of 53.6 μm (the distribution of normal particle sizes was between 50-60 μm).

Magnesium was selected to be used as the material from which the space holder was constructed from due to its low solid solubility levels when added to titanium [113]. Spherical Mg power (> 99.5% purity) was used with an approximate particle size of roughly 300 μm (the distribution of normal particle size was between 250-355 μm). This particle size was chosen after consulting existing literature which states that a pore size of 250 μm aids cell migration. On the other hand, a high sphericity of magnesium powder was discovered to attain the ideal mechanical properties resulting from the porous structure [113]. Consequently, the current research used a 250 μm pore size to achieve optimum osteointegration outcomes following after the porous samples were sintered.

The PVA-enhanced Ti powder and the Mg powder were mixed for an hour. This process produced mixtures of 60%, 70% and 80% magnesium by volume. Next, cylindrical samples (of 9mm diameter and 9mm height) were generated for characterisation. This was achieved through the use of uniaxial compression using a 12t manual hydraulic press with floating die operating at 600 MPa. The hydraulic presses were used to produce a minimum of three samples for each porosity examined, with identical production procedures used to generate each sample. This heightens the repeatability and accuracy of the study.

Figure 3.1 Atmospheric controlled vacuum furnace.

An atmosphere-controlled tube furnace was used to sinter the samples under highly pure argon gas heated to 1200 °C for 2 hours. Contamination was mitigated by placing the samples in titanium crucibles through the machining of titanium rods. Furthermore, the temperature was chosen to be higher than Mg's boiling point of 1090 °C because the melting and boiling of magnesium powders would cause erosion of scaffold integrity. It would also decrease the removability of the space-holder. The temperature was increased gradually at a rate of 4 °C / min.

3.2 Microstructural examination

Before examination of the microstructures was conducted, the surface damaged layer of each sample was detached through grinding the samples with SiC paper of grit size 600. Next, the samples were each mounted using epoxy resin (where hardener and resin were mixed at the ratio 1:2) to allow for polishing: each sample was positioned in a levelled container and the container was topped up with the resin mixture. By allowing the resin to cure wholly, a better polish and clearer image was achieved under the metallographic microscope. To allow for complete curing, the specimens were left to set overnight. After the samples had set, they were extracted from their containers and polished using SiC paper of grit size 800, 1000 and 2500 on a Metcon Forcipol 2p polishing. A rotation speed of 100 rpm was applied, and each sample was polished for 180 seconds.

Figure 3.2 a) Metcon Forcipol 2P polishing station b) Silicon carbide paper of grid size 800, 1000 and 2500.

Following the polishing procedure, each sample was rinsed for 10 minutes with acetone using an ultrasonic cleaner before being thermally dried. This process ensured that each sample was appropriately prepared for metallographic observation through optical and / or electron microscopes. To analyse the distributions of different pore sizes, an optical microscope was used to observe specimens showing lathering. These images were recorded using a digital camera attached to the microscope. To analyse the microstructures of the samples, Kroll's reagent (2.5% HF, 5 % HNO_3 and 92.5 % H_2O) was applied to the specimens for roughly 10 seconds. Next, each sample was washed with H_2O and dried in a fume cupboard. An electron microscope was then used after the samples were mounted to the device using carbon conductive tape.

3.2.1 Morphology, porosity and phase analysis

The foam produced in the samples was analysed using the optical and scanning electron microscopies (SEM, Jeol JSM 6400), which evaluated both morphology and microstructure. To do so, each sample was ground so that the pore structure was observable. They were also mounted and metallographically prepared as each sample was dissected length-wise along the compaction axis. Kroll's solution was then applied to expose the foundational microstructure of the porous structures. The effect of the subjection to a small compressive strain was also investigated to identify the pore structure of samples under compressive deformation.
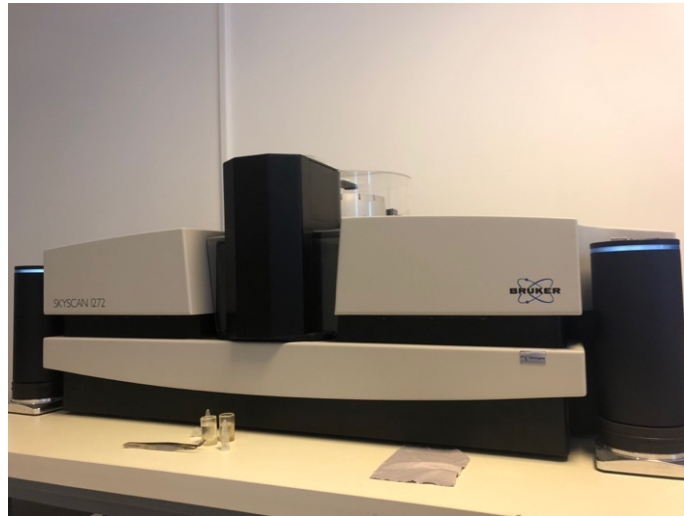
Figure 3.3 Micro-CT Scanner (Brüker GmbH, Germany).

The micro computed tomography (Micro-CT) system used was a Brüker Skyscan 1272 micro-CT scanner (Brüker GmbH, Germany), providing a resolution of up to 0.35 μm (16Mp). This procedure allowed examination of both the internal and external pore structures of sample. It further facilitated evaluation of volume and surface and volume attributes relating to bone morphology such as pore distribution and porosity. The specimens side structural views were analysed in three directions using incrementations of 0.01 mm.

3.2.2   Pore size distribution and Porosity determination

To investigate the distribution patterns of micropores, ImageJ and the image threshold technique was applied to SEM images. This measured the overall porosity level and microporosity rates as well as determining the following: mean pore diameter and pore morphologies. After samples were scanned with ImageJ, the resultant micrograph images were sharpened to produce clearer images. Clearer images were needed as the imaging program uses colour threshold changes and these need to be cleaned for more accurate analysis: a clean image leads to ease of detailed investigation of the minutiae of the images. The images were cleaned using a technique by which each optical micrograph of a polished flat surface Ti foam was recorded using an optical microscope.
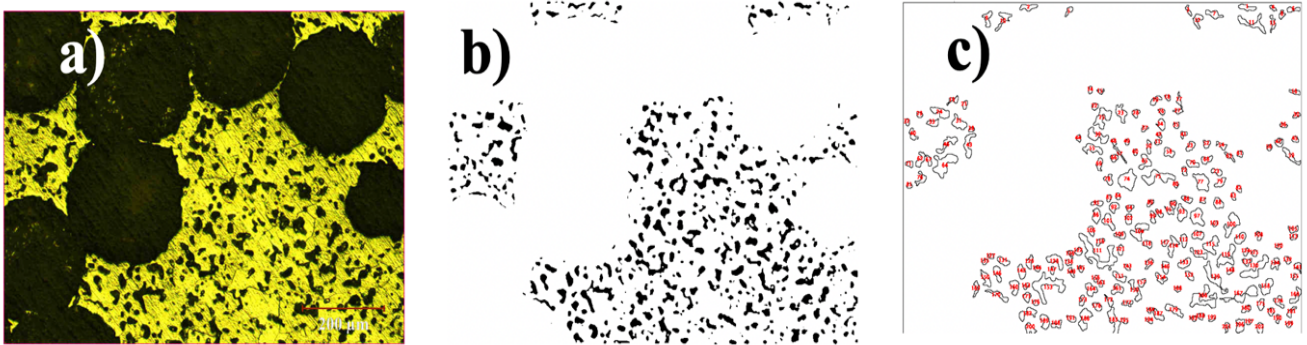
Figure 3.4 Micro size porosity evaluation via imageJ.

After this step, as can be seen in Fig 3.4 and 3.5, the micrograph images were converted into grayscale 8-bit images so that the image thresholds could be altered. They were altered such that the particular level they were calibrated to resulted in black and white image. Following this, the images were further analysed by using a running pore analysis to produce the pore fraction of the micrograph and a list of every pore structure.
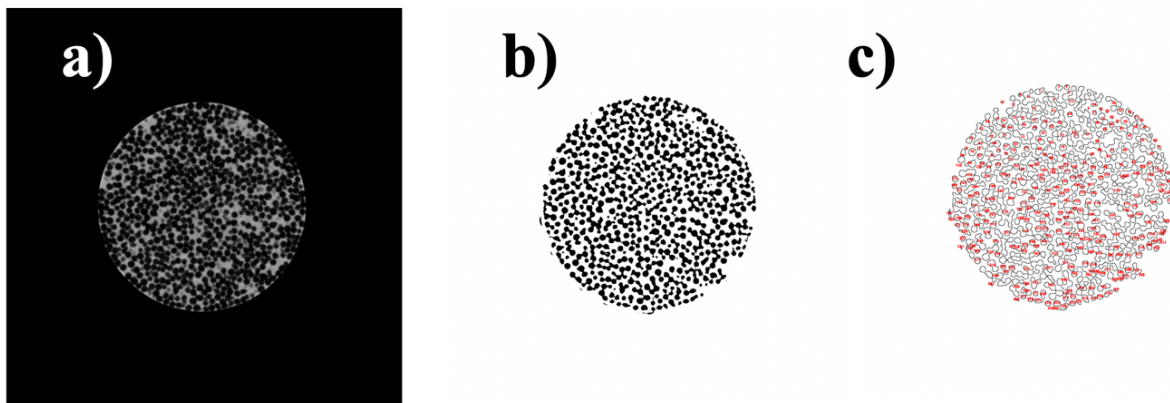
Figure 3.5 Macro size porosity evaluation via imageJ.

Once the recorded images were analysed, the data produced was recorded in a spreadsheet using Microsoft Office Excel to allow for quantitative analysis and graphic presentation. The transfer of data into a spreadsheet allowed pore distribution to be determined, which led to analysis to determine the connection between micropore morphology, size and immersion period.

An imager analyser was also used to compute average neck size and porosity through quantitative metallography studies. The determination of these facilitated the analysis of the relationship between mechanical properties and neck and pore size. From the optical

micrographs produced, a minimum of 30 necks and their surrounding particles were evaluated to ensure statistical reliability (Fig 3.6).
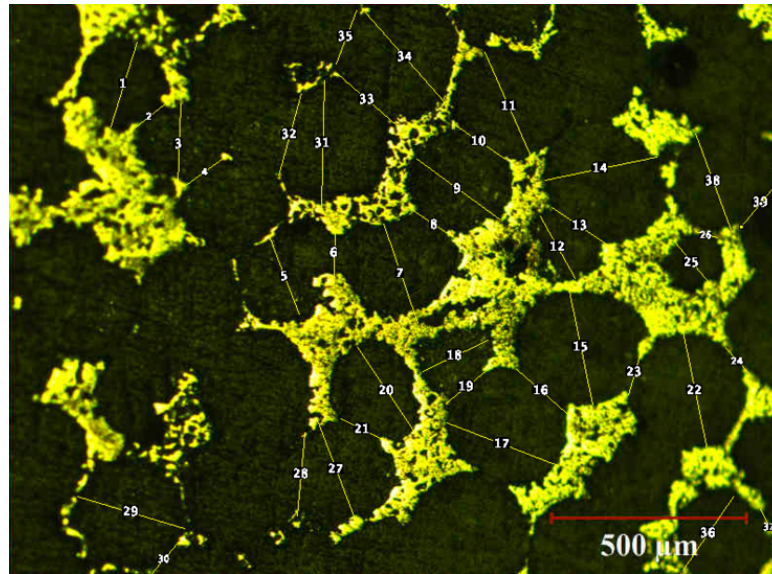
Figure 3.6 Neck size measurement.

3.3   XRD (X-ray diffraction) analysis

The phases of titanium foams produced in the course of the fabrication process were found through diffraction analysis. X-Ray Diffraction (XRD, RigakuD/ Max2200) was used to determine the primary phases in the specimens. Each sample of porous titanium was formed into plates of 9 mm x 9 mm with a depth of 1 – 2 mm and positioned in specimen holders, with their positions maintained using a light adhesive. Each holder had a diameter of 25 mm. The XRD was then applied between 30 and 90° 2θ angles using a Cu- Kα radiation source at 40 kV. The identification of main phases was achieved through analysing the elemental starting powders and the foamed specimens. It was ensured that the effect of preferred orientation was mitigated by rotating the specimens. The following section will lay out the details of how the instruments were programmed to collect the data needed.

3.4   Density Measurement

Archimedes' principle of weight measurements was used to measure the density and the total, open and closed porosity content of the foamed Ti samples. To do this, Xylol reagent by Precisa XB220a balance was applied in conjunction with a density determination kit.

Firstly, each dry sample was weighed in air. Next, they were submerged in xylol solution in desiccators. The desiccators were then subjected to vacuums for 30 minutes to allow the

xylol solution to fully permeate through the foam pores. After this process, the foams were extracted and positioned in beakers of xylol reagent and were weighed while present in the solution. Lastly, the sepcimens were removed from the xylol reagent and the weights were measured as quickly as possible in air.

To calculate the total porosity percentages of the foam samples (P_{total}, %), by Eq. (3.3), the foam volumes (V_{foam}) were first calculated using Eq. (3.1). Next, Eq. (3.2) was used to calculate the foam densities (ρ_{foam}) where the density of xylol (ρ_{xylol}) and density of bulk Ti are taken as 0.861 g/cm^3 and 4.506 g/cm^3, respectively.

$$V_{foam} = \frac{m_{a,x} - m_{x,x}}{\rho_{xylol}} \tag{3.1}$$

$$\rho_{foam} = \frac{m_a}{V_{foam}} \tag{3.2}$$

$$P_{total}(\%) = 100 - \left(\frac{\rho_{foam}}{\rho_{Ti}} \text{x} 100\right) \tag{3.3}$$

Where,

m_a: mass of the specimen

$m_{a,x}$: mass of xylol reagent immersed specimen in air

$m_{x,x}$: mass of xylol immersed specimen in xylol reagent

Percentages of open and closed pores, P_{open} (%) and P_{close} (%), of the Ti foams were determined by Eqs. (3.4) and (3.5).

$$P_{open}(\%) = \frac{\text{volume of xylol in pores}}{\text{volume of the foam}} \text{x} 100 \tag{3.4}$$

$$= \left(\dfrac{m_{a,x} - m_a / \rho_{xylol}}{m_{a,x} - m_{x,x} / \rho_{xylol}} \right) x100 \qquad (3.5)$$

$$P_{closed}(\%) = P_{total}(\%) - P_{open}(\%) \qquad (3.6)$$

3.5 Surface Processing

The next stage of the study involved activating the surfaces of porous Ti foams by the triggering of the sodium rich titanate phase ,a bioactive substance which interacts with living bone to create an apatite layer which is similar to bone on its surface when it is in body fluid. To conduct this hydrothermal surface process, two steps are required: it must be submerged in NaOH aqueous solution and then the coating layer must be heated. However, the factors in this process such as NaOH solution temperature and concentration must be optimised. Additionally, the temperature used in the heat treatment must also be carefully controlled to produce artificially homogenous uniform sodium titanate stage on the permeable surfaces.

As the majority of porous structures are the most advantageous materials to be used for bone formation, existing studies have used 80% porosity foam samples when carrying out research on the optimum parameters to use. The hydrothermal surface procedure in NaOH arrangement was led in high temperatures (max. 300 °C) and weight (max. 200 bar). The holder utilized was the Parr 5500 reactor with stirrer, appeared in Figure 3.7. 80% porous specimens were at first submerged in 5 M NaOH solution at 60 °C for 24 hours.

Figure 3.7 Hydrothermal treatment reactor.

3.5.1 In vitro Studies

The success of artificial materials bonding to human bone depends on the generation of a bonelike apatite on the material's surface upon insertion into the living body [102]. The surface apatite is a widely recognised precursor of bone and it functions by encouraging rapid bone formation and the inhibition of surface fibrous tissue development [106]. As a result, it is more beneficial to conduct in vitro rather than in vivo studies in order to examine the relative biocompatibilities of the specimen surfaces and the materials themselves before they are inserted into living animals.

Figure 3.8 SBF Solution and immersed foam samples with 60%,70% and 80%.

When the materials are tested in vitro, SBF is used because it has a similar ion concentration to blood plasma so can accurately recreate a body-like environment. The tested materials will be identified as bioactive if they promote the formation of bonelike apatite upon immersion in SBF. Therefore, the porous Titanium samples treated with 60, 70, 80 and 80 NaOH in the current research were immersed in SBF (36.5 ± 0.5 °C, pH 7.4) for varying

lengths of time. The SBF used is known as Ringer's solution (B. Braun AG, Germany) for ageing. It consists of different salts dissolved in water to imitate animal and human bodily fluids. The active substances present in Ringer's solution are displayed in Table 3.1 (amounts in 100 mL).

Table 3.1 Summary of active substances in Ringer's Solution for infusion from B. Braun AG

Active substances	100 mL contains
Sodium Chloride	8.6 g
Potassium Chloride	0.3 g
Calcium Chloride Dihydrate	0.33 g

When the materials are tested in vitro, SBF is used because it has a similar ion concentration to blood plasma so can accurately recreate a body-like environment. The tested materials will be identified as bioactive if they promote the formation of bonelike apatite upon immersion in SBF. Therefore, the porous Titanium samples treated with 60, 70, 80 and 80 NaOH in the current research were immersed in SBF (36.5 ± 0.5 °C, pH 7.4) for varying lengths of time. The SBF used is known as Ringer's solution (B. Braun AG, Germany) for ageing. It consists of different salts dissolved in water to imitate animal and human bodily fluids.

Table 3.2 Simulated Body Fluid Immersion Groups and their subjected timelines

Specimen Type	Immersion days in Simulated Body Fluid
As Received Samples 60%,70%,80% porosity levels	0
	14
	21
	28
5 M NaOH, for 24 hours immersion, 60 °C 80% porosity level	0
	14
	21
	28

Once the immersion times in SBF was formulated, different surface treatment processes were applied to the as-manufactured porous samples and the 80% porosity samples treated with NaOH. All samples were then submerged in SBF for 14, 21 and 28 days, with the SBF temperature controlled to be at 36.5 ± 0.5 °C. The solution was replaced with a new batch each two days to maintain a stable ion concentration for the experimental environment. After the samples were submerged in SBF, they were carefully washed using deionised water and dried in a furnace overnight at 30 °C. The different immersion times in SBF for each process are displayed in Table 3.2.

3.6   Mechanical Testing and Properties

The mechanical attributes of the Ti samples were examined. To do this, compression testing was applied to cylindrical porous samples (9 mm by 9mm) at room temperature via a universal testing system (Instron 3369, Illinois Tool Works Inc., USA) with a crosshead velocity of 0.005 mm/s. The yield strength , strain at fracture and maximum compressive strength were measured by applying increasing loads to each sample until the sample fractured completely. The 0.2% offset method was used to evaluate the elastic moduli and yield strengths.

Figure 3.9 Universal testing system (Instron 3369, Illinois Tool Works Inc., USA).

After the compression tests were complete, data collection was conducted over the course of the loading interval. The extension values of the specimen recorded were then converted through the use of a particular dimensionless strain value so that each singular set of data could be analysed and compared holistically and comprehensively. This allows a compressive stress-strain curve to be plotted.

3.6.1 Hardness testing

The Emcotest Duravision 2000 microhardness tester with Vickers diamond pyramid indenter machine was used to test indentation hardness. The samples tested were produced by extracting three groups of foaming specimens. The samples measured approximately 9 mm x 9 mm and after extraction were prepared by applying SiC paper to grind the samples with a grit of up 1200. After this, the samples were mechanically polished with diamond paste. To measure the Vickers hardness of each sample, the surface of each sample was subjected to a load of 100 gf for 20 seconds. This was repeated and recorded for an average for 15 instances in each sample.

Figure 3.10 Emcotest Duravision 2000 microhardness tester.

3.7 FEA Model Theory

The FEA technique can be utilized to calculate the approximate solution of governing differential equations in the mechanics of deformable solids. First of all, the area of interest

is dissassembled into a selection of 2D or 3D elements (meshing). The meshing components are associated by sharing normal points (nodes) and each node is related with the unknowns (for example temperature) to be comprehended. A definitive result is to change the ODEs or PDEs into a linear combination of a finite set of arithmetical functions.

FEA model hypothesis is established on the 'rule of virtual work' which can be spoken to as far as equilibrium equation of loads, where the work done by outer loads for a virtual displacement should be equal to the internal virtual work consumed by the component amid that displacement. Numerically, it very well may be communicated as:

$$\delta \vec{v}^T f = \int_V \varepsilon^T \sigma \, dV \qquad (3.7)$$

σ: A group of internal stresses.

ε: Internal strains.

Written in the form of virtual displacement:

$$\varepsilon = [B]\delta\vec{v} \qquad (3.8)$$

[B]: The matrix of strain-displacement.

Written in the form of the stress:

$$\sigma = [D][B]\delta\vec{v} \qquad (3.9)$$

 [D] : The elasticity matrix.

$$\delta \vec{v}^T f = \int_V \delta\vec{v}^T [B]^T [D][B]\delta\vec{v} \, dV \qquad (3.10)$$

Written after it has been rearranged:

64

$$\delta \vec{v}^T f = \delta \vec{v}^T \int_V [B]^T [D][B] \, dV \delta \vec{v} \qquad (3.11)$$

The above equation could be reduced to:

$$f = [k] \delta \vec{v} \qquad (3.12)$$

Comprising of n equations for dv n selections to be calculated, the governing equation now has turned into a matrix equation system.

3.7.1 Numerical Procedure

The three-dimensional structure of the titanium specimens were evaluated through a micro-CT machine (Skyscan 1272, Brüker GmbH, Germany), with a resolution of up to 0.35 μm (16 MP). From the images produced by the micro-CT, 3D FEM models were constructed so that the mechanical characteristics of porous Ti samples could be evaluated. To produce the 3D specimen structures, 650 2D images were aggregated for each porous sample using the commercial Seg3D2 and ImageVis3D image-processing packages.

Figure 3.11 shows the reconstructed models of the crushable foam models formed from the Ti-foam samples with 60%, 70%, and 80% porosity. The commercial finite element program LS-DYNA was applied to all the simulations extracted from the 3D models. They each had a volume of 9 mm x 9 mm and signified the overall sample in compression testing.
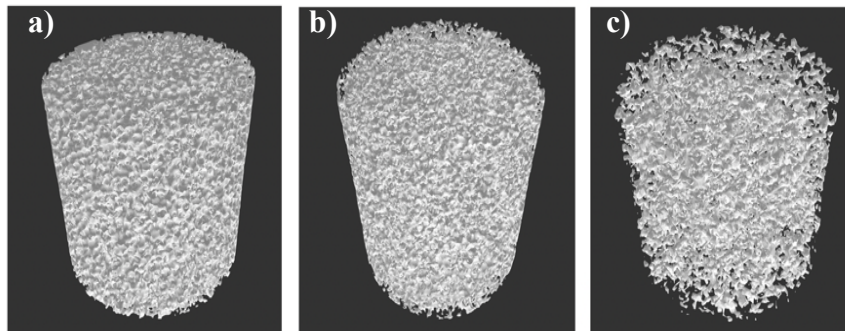
Figure 3.11 3D solid models of porous Ti samples with (a) 60%, (b) 70%, and (c) 80% porosity.

To conduct the compression tests, the bottom nodes of the sample mesh were attached and a displacement boundary condition (maximum engineering strain: 15%) was placed onto the upper section. This is shown in Figure 3.12. The flat dies were represented as rigid surfaces, with the bottom die fixed and the top die flattened uniaxially with a crosshead velocity of 0.005 mm/s. Axisymmetric elements were applied for the cylindrical workpiece, and the coefficient of friction between the contact surfaces was set at 0.5 [20]. The Ti-foam matrix was modelled as an elastoplastic material with isotropic hardening.
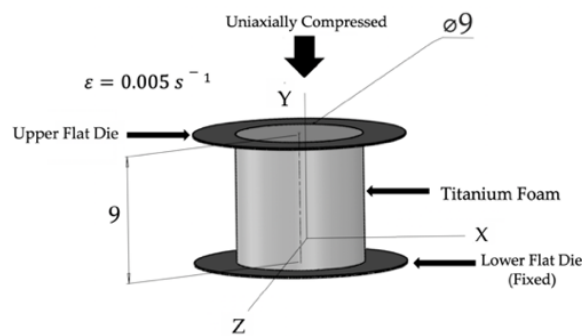
Figure 3.12 Figurative representation of FEM uniaxial compression test simulation.

3.7.2 Application of Ti-Foam Model to Dental Implant with Simple Shape

A possible solution for the existing issues surrounding stress shielding and bone fracture may be the employment of fully porous metals [6]. To investigate the success of such a solution, a 3D finite element analysis of a Ti-foam dental implant design was conducted, and the implant model was combined with a finite element model of a simple human tooth. The 3D model used comprised of the dental implant and the surrounding cancellous bone and cortical bone (as displayed in Figure 3.14). Boundary conditions were imposed to limit all forms of translational movements.
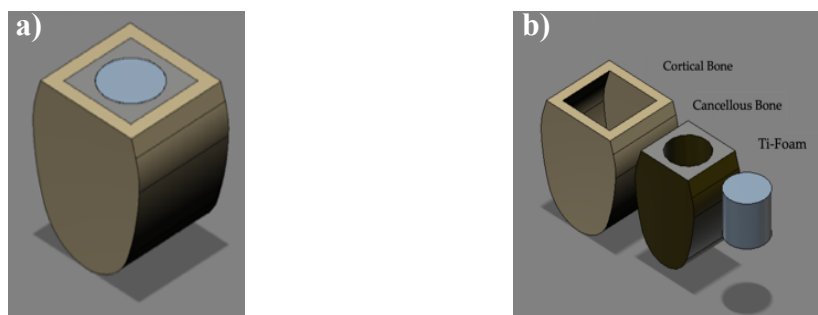
Figure 3.13 Dental implant and cancellous and cortical bone around Ti-foam implant.

At the intersection points between bone and implant and compact bone and trabecular bone, it was assumed that perfect bonding occurred. Forces of 17.1, 114.6, and 23.4 N in lingual, axial, and mesiodistal directions, respectively, were applied to the implant [9, 10]. The material parameters used for the compact and trabecular bone are displayed in Table 3.3. Both types of bone were approached as if they were linear elastic materials [21]. On the other hand, the solid Ti foam was handled as an elastic-plastic material.

Table 3.3 Summary of mechanical properties of bone types used in dental implant application.

Material	Young's Modulus, E(MPa)	Compressive Strength (MPa)	Density (g/cm^3)	Reference
Cortical Bone	16500	155	1.24	[4]
Cancellous Bone	935	8	1.19	[4]

4. RESULTS AND DISCUSSION

4.1 Introduction

Titanium foams are perfectly suitable for use as biomedical applications due to their properties: they are compatible with biological material, resistance to corrosion and low elastic modulus. Porous titanium foams have been researched as a substance with high osseointegration and congruity with bone stiffness. In the course of the research conducted, it has been found that porous titanium foams can be generated using a space holder method in which powdered elemental metals are applies as the initial materials. This chapter will present the results obtained relating to the physical, morphological, phase composition and development, and mechanical properties of the porous titanium foams formed. Furthermore, analysis will be conducted with use of finite element analysis. To obtain these results on the characteristics and properties of the porous foams, x-ray diffraction was operated at room temperature. The additional methods used were: EDS (Energy-Dispersive X-Ray Spectroscopy), SEM (Scanning Electron Microscopy), optical microscopy, image analysis, compressive tests and FEM (Finite Element Method).

4.2 Raw material Evaluation

Pure titanium powder (> 99% purity (ASTM 1580-1), the powdered metallic element, was the raw material used in this process. The powder had an average particle size of 53.6 μm and normal particle size distribution of between 50-60 μm. The structures of the elemental powders were evaluated prior to the blending procedure. The corresponding EDS energy spectra measurement is presented in Figure 4.1.

Figure 4.1 EDS (Energy-Dispersive X-Ray Spectroscopy) measurement of a) 60% porosity, b) 70% porosity, c) 80% porosity titanium foams.

After the blending procedure was applied to the titanium powder, X-Ray Diffraction (XRD) was the method used to analyse the crystal formation of the titanium powders and to determine whether other phases were present. Figure 4.2 displays the diffraction patterns of the mixed powders obtained from XRD. As can be seen in Figure 4.2, the different peaks correspond to individual elements and the structure can be described as hexagonal close packed (hcp). This shows that α-titanium was present. No other phases were found to exist in the mixture following blending.
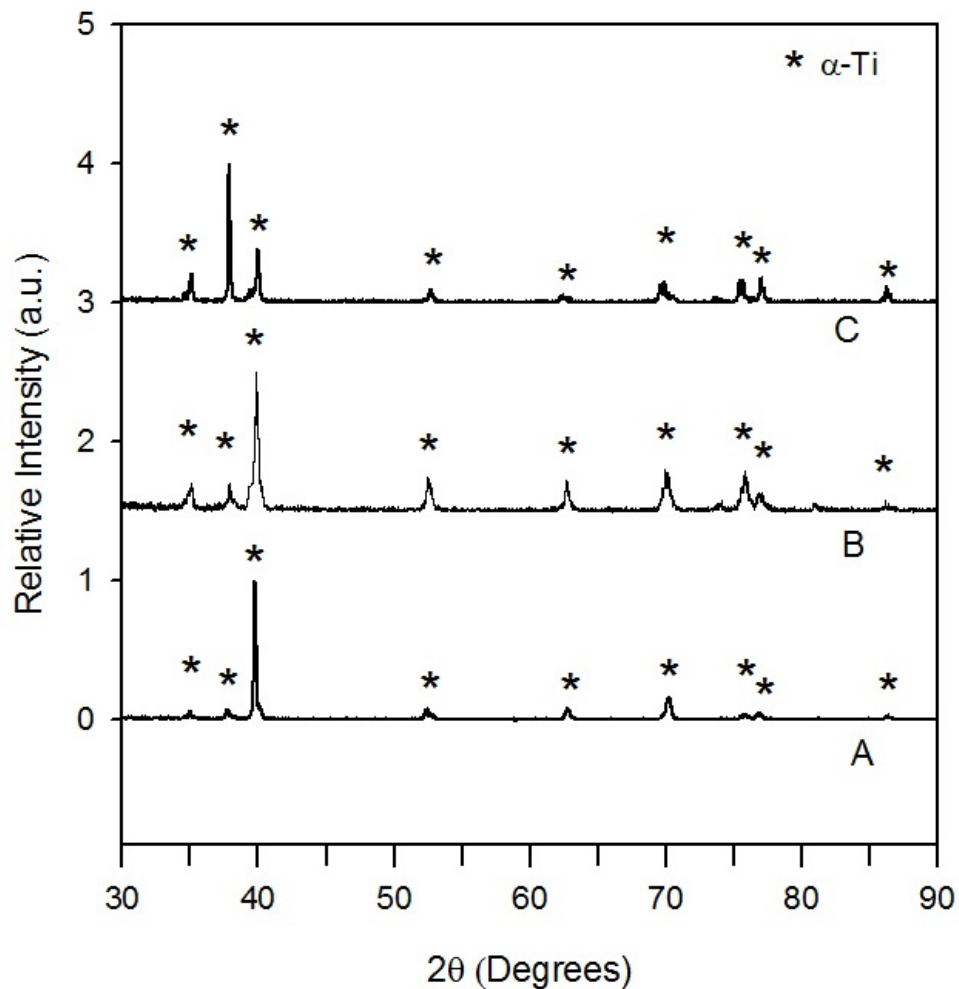
Figure 4.2 X-Ray diffraction patterns of manufactured titanium foams with a) 60%, b) 70% and c) 80% porosity levels.

Many different characteristics of titanium foams need to be controlled to ensure that they are suitable for biomedical applications. For instance, the porosity, morphology, and the types of pores present are all important in ensuring that appropriate titanium foams are produced. Additionally, it is critical that the foams manufactured to do not contain any oxides, binder residue or magnesium. Therefore, magnesium was wholly extracted from all of the specimens used in this research during the production process to ensure that the ultimate

samples contained no binder residue. The magnesium is observable in diffraction patterns in Figure 4.2. Furthermore, the evaluation of the samples showed that there were no titanium oxides present; indeed, the production method only produced α-Ti phase as was revealed by grains of α-phase and by diffraction patterns.

4.3 Microstructure and Pore Characterisation

When analysing the characteristics of the microstructure of the foam produced, there were two primary factors to evaluate. Firstly, it was important to determine pore properties (size, shape and orientation); secondly, topological factors needed to be investigated. The latter included arrangement and relationships with neighbouring pores.

To determine the density of the cellular materials, the volume fraction of material in nodes, edges and walls needed to be measured. This was crucial because the mechanical properties of samples are highly affected by the number of nodes, cell edges and walls per cell, length, thickness and curvature of cell edges, and shape of cell edges. However, it is difficult to accurately measure these in real life, therefore, an alternative is to evaluate a mass of solid material [7].

It was discovered that the pore structures of 60% and 70% porosity titanium foams were relatively smooth with an even distribution of pores with both open and closed morphology. Furthermore, the cell walls showed high levels of definition and all displayed similar thicknesses. On the other hand, in the 80% porosity titanium foam samples, there was a partially sintered system of spherical powders present on the cell walls. Furthermore, pore structures were discovered to be relatively uneven and complex. Characteristics relating to the cell wall and edge (e.g. thickness) were discovered to vary contingent on the total pore volume fraction and the size and shape of titanium powder used. These features are important as they influence the mechanical properties of the foam. In accordance with predictions, the 80% porosity Ti foams exhibited the thinnest walls, varying in accordance with pore size.

The shape of struts in manufactured foams typically demonstrate an hour glass shape whereby the material is gathered at the cell nodes instead of the cell edges. Consistently with this, cell wall and edge thickness tend to decrease from the cell node to the cell edge centre. The samples with 60%, 70% and 80% porosities were subjected to SEM imaging prior to deformation. These images are exhibited in Figure 4.3.

71
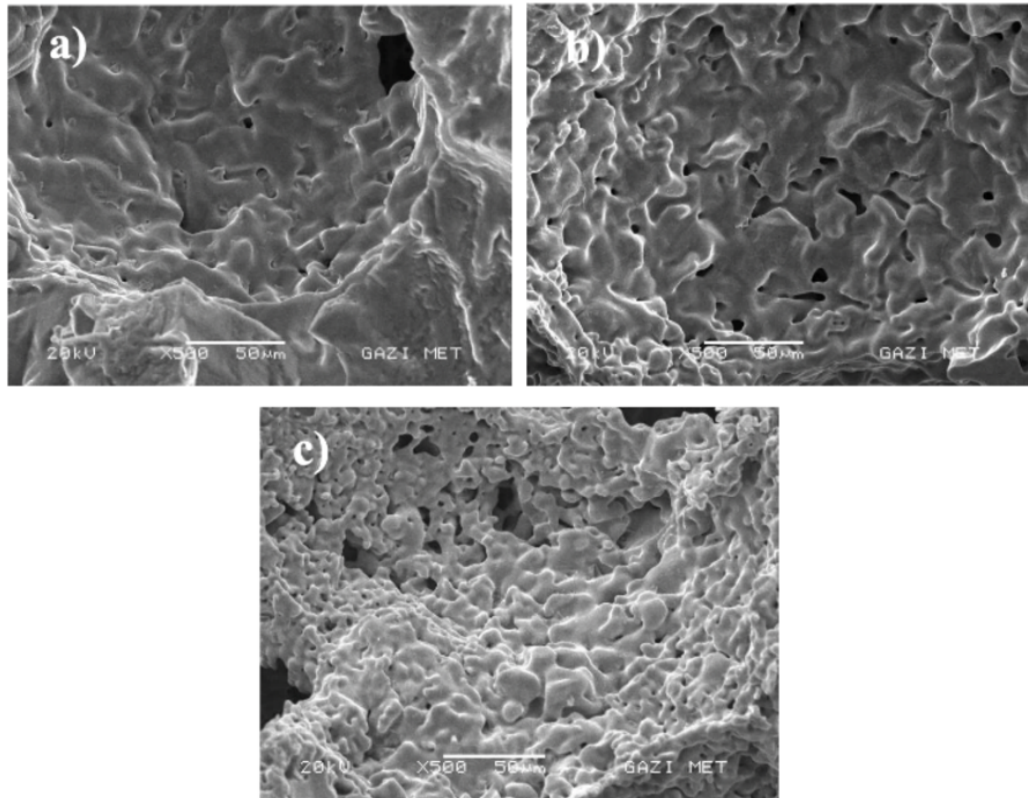
Figure 4.3 SEM macrostructure of porous titanium samples at 500x magnification with porosities of: (a) 60%; (b) 70%; (c) 80%

The observed average pore diameters (~ 264.01 μm) were consistent with the space-holder size distribution. It was predicted that Mg residue concentration would either remain relatively consistent or otherwise would decrease where samples were produced with smaller quantities of Mg. Where the samples were prepared with less magnesium, it was found that the resultant pores were generally rounder with smoothly curved pore walls. Figure 4.4 demonstrates both the large macropores which occurred as a result of the space-holder particles and the micropores which resulted from the incomplete sintering of titanium powders. This characteristic is commonly found in the microstructures of sintered Ti.
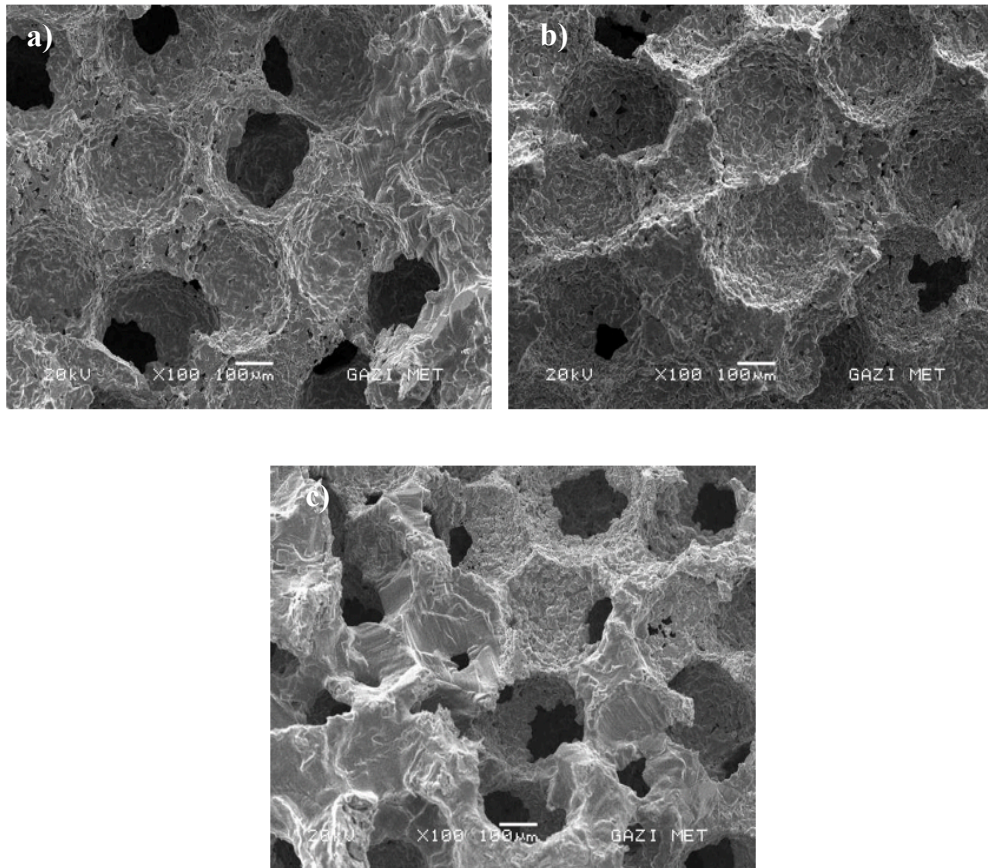
Figure 4.4 SEM macrostructure of porous titanium samples at 100x magnification with porosities of: (a) 60%; (b) 70%; (c) 80%.

It was also shown that the surface displayed debris, discharge craters and microcracks. The microcracks may have resulted from a rapid cooling rate [138]. Furthermore, the surface also shows globules of recast material. These materials had been heated to melting point before they returned to a solid state on the surface. Images of the macrostructures are displayed below.

Figure 4.5 presents the large macropores which resulted from the extraction of magnesium particles. It also demonstrates that the cells walls exhibit micropores, caused by incomplete titanium sintering. This is often observed in the microstructures of sintered titanium. While the cell walls were microporous, it can be seen that the sintering process resulted in the formation of bonds between the titanium powder particulates, as demonstrated by the grain boundaries of α-Ti in Figure 4.5(b).
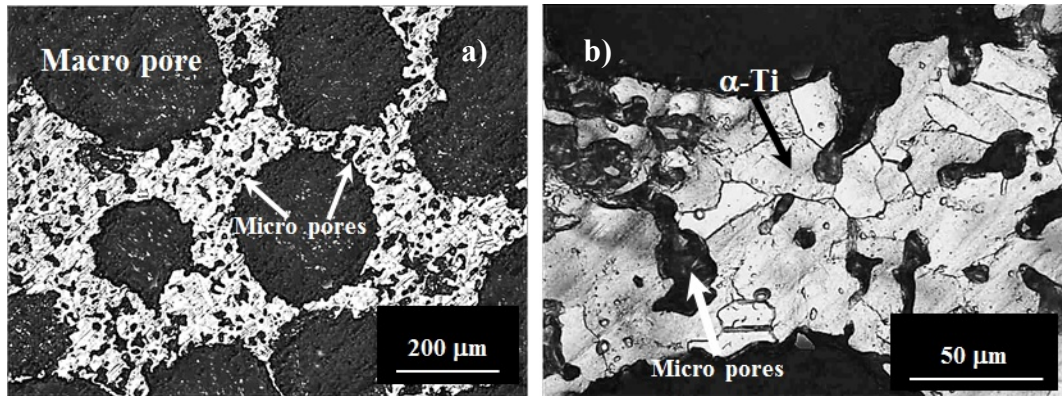
Figure 4.5 Polished cross-sectional optical microscope images of Ti-foam with 55.9 % porosity showing (a) macro-pores formed by evaporation of Mg and microporous cell walls (b) cell wall containing micro pores and grains of α-Ti phase.

Figure 4.5 shows the images obtained from micro-CT scans of 60%, 70% and 80% porosity titanium powders. From the micro-CT images obtained, it was possible to construct 3D solid models by imitating the actual specimen structure. These are displayed in Figure 4.6.

Through the use of micro-CT scans, it was discovered that the porosity of the manufactured foams was congruent with the porosity aimed for when the process began. ImageJ was used to measure the diameters of the pores. The diameters were found to be around 253 μm, 267 μm and 273 μm for the samples with targeted porosities of 60, 70 and 80%, respectively. Therefore, the pore size in all samples was smaller than that of the starting average Mg particle size (at 300 μm). This may have resulted from the sintering procedure as sintering can cause bonds to form, therefore increasing the density. As a result, the pores are likely to decrease in size. However, in samples where higher initial quantities of Mg were used, the average pore size of the manufactured foams was generally larger due to the increase in interconnections between pores following Mg extraction (Figure 4.6(c)).
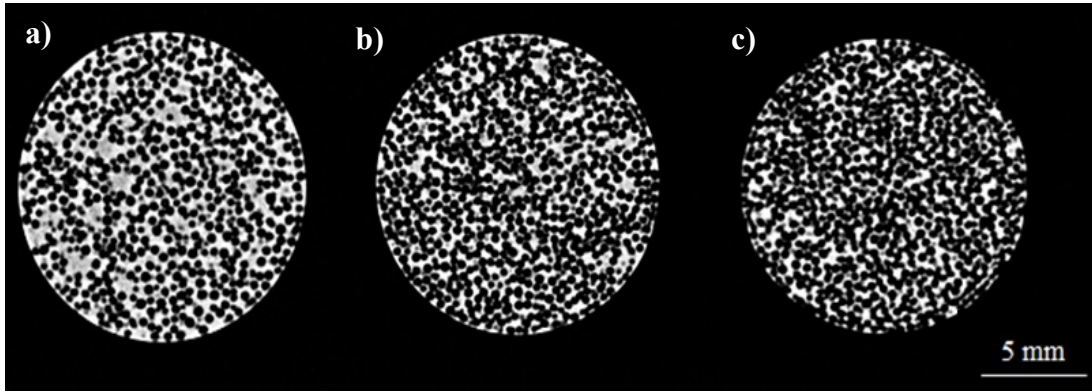
Figure 4.6 Micro-CT Scan microstructure of porous titanium samples with porosities of: (a) 55.9%, (b) 68.4%, (c) 78.0%.

4.3.1 Porosity Size Analysis

The micropores exhibited on the foam cell walls and edges were generally sized between 0-30 μm. The average micropore size were discovered to vary between 12-17, 17-25 and 23-30 μm for foams of 60,70 and 80% porosity titanium foams respectively, displaying total porosities in the range 55.9%, (b) 68.4%, (c) 78.0%. As was predicted, the 60% and 70% porosity samples exhibited the smallest micropores in the cell walls and edges due to the lower quantity of space holder material, which inhibited the amalgamation of different pores. In contrast, the average macropore size was found to depend on the total porosity of the sample or the quantity of magnesium used initially. In the 80% porosity Ti foam samples, some macropores were found with sizes of 586 μm. These are likely to have formed due to the integration of several macropores.
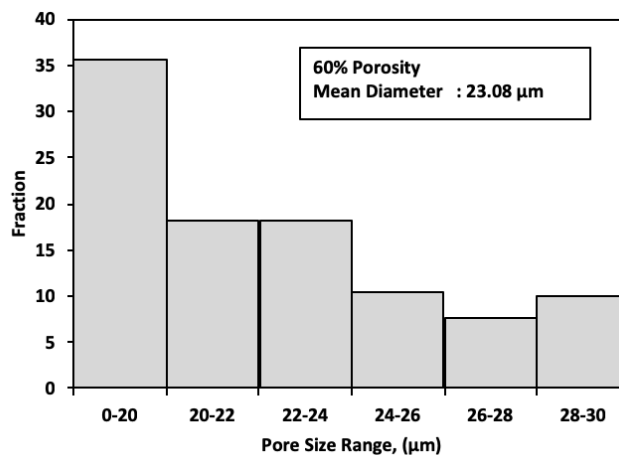
Figure 4.7 Micro size porosity analysis data performed by imageJ image analyzer with 60% porosity.
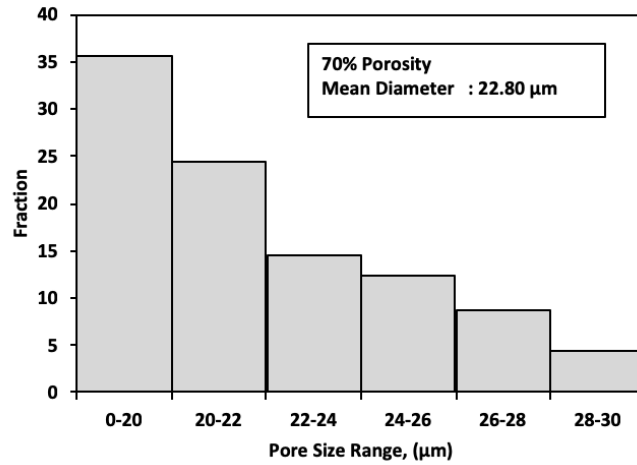
Figure 4.8 Micro size porosity analysis data performed by imageJ image analyzer with 70% porosity.
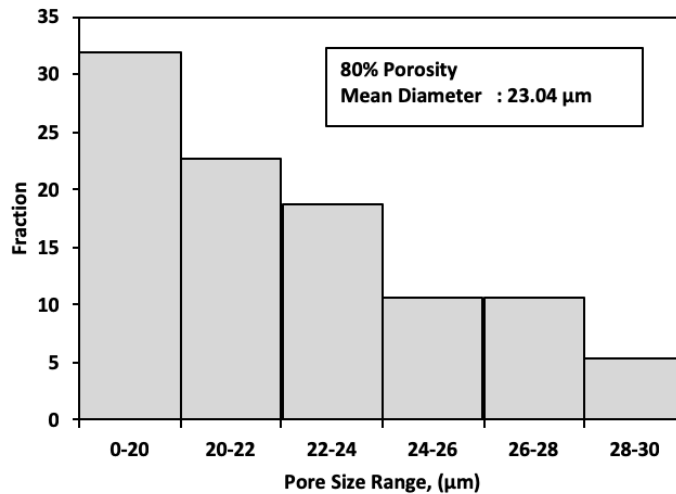
Figure 4.9 Micro size porosity analysis data performed by imageJ image analyzer with 80% porosity.

In relation to the macropores in the manufactured Ti foam samples, the average macropore size was measures to be ~252.32 µm (at 60 %), ~267.05 µm (at 70 %), and as high as ~272.66 µm at 80 % porosity. This variation is most likely due to the shrinkage of cell walls and edges which tends to occur in samples with lower porosity. On the other hand, where there is a high porosity, there is also a high rate of macropore interconnection. This amalgamation of macropores will then create pores which are larger than the expected pore size. As displayed in Figure 4.10, where the samples had a porosity of 60%, the macropore size varied between ~ 150 and 300 µm, while macro pores as high as 567 µm were observed to exist in the samples with a higher porosity at 70%. As macropore size increases, it suggests

that there was a higher rate of macropore interconnection, as exhibited in the SEM micrographs.
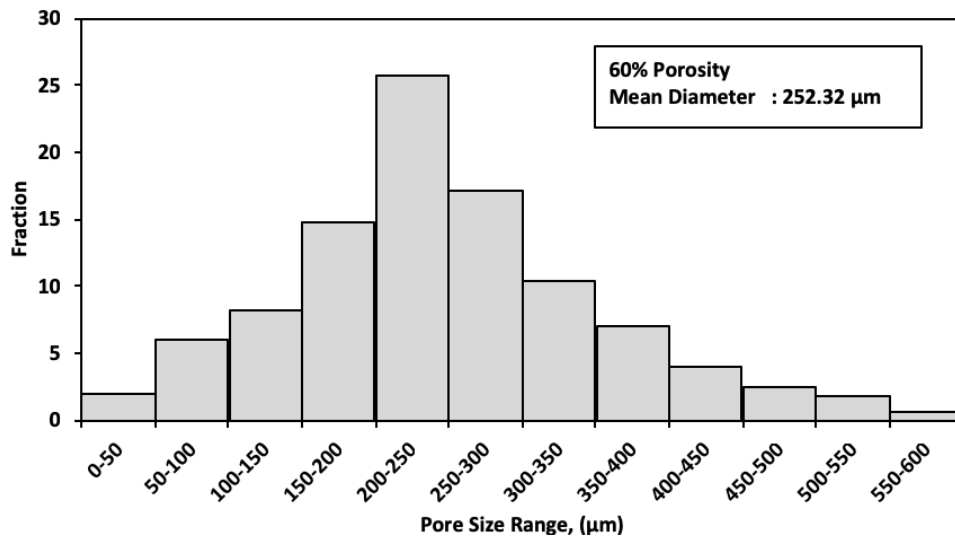
Figure 4.10 Macro size porosity analysis data performed by imageJ image analyzer with 60% porosity.
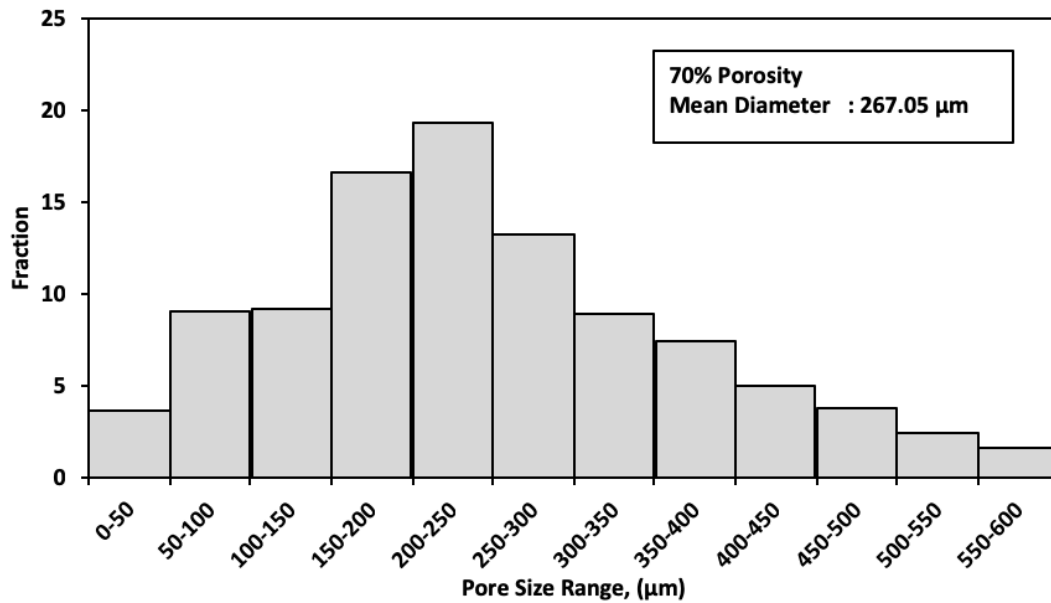
Figure 4.11 Macro size porosity analysis data performed by imageJ image analyzer with 70% porosity.
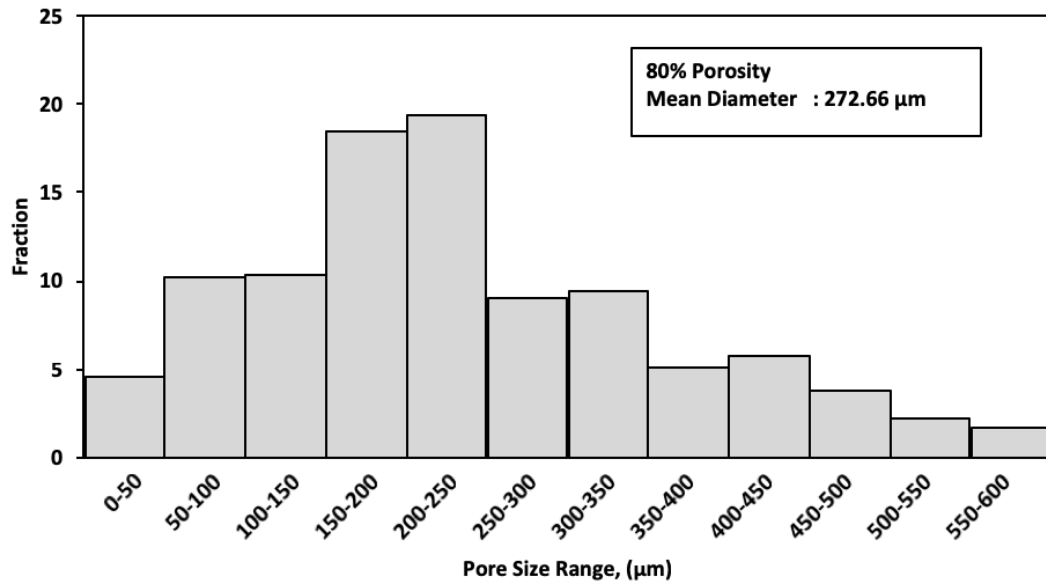
Figure 4.12 Macro size porosity analysis data performed by imageJ image analyzer with 80% porosity.

This relationship between macropore size and porosity rates was also demonstrated in samples of 80% porosity. Thus, the samples demonstrated that the average pore size decreased initially before it increased again. The presence of this trend in titanium foam samples with 80% porosity is likely to have been caused by the amalgamation of macropores. However, in both the 80% and the 70% porosity samples, a wider distribution of sizes was observed, namely between 50-350 μm.

After statistically analysing the pore sizes demonstrated in the different foam samples, it was found that the average size of space holder particles at 53.6 μm during sintering tended to result in porous Ti materials with pores sized between 18.6–567 μm. Any resultant pores which were smaller than the magnesium particles initially used were most likely produced as a result of the shrinking of the material during sintering. All titanium samples with porosities of 60%, 70%, and 80% showed an even distribution of pore diameters in the range of 150–300 μm. Use of an SEM has also shown that there is good interconnectivity between the surface and inner porous structure.

4.3.2   Interparticle Neck Size

Measurements of interparticle neck size, density, porosity and shrinkage (as well as reduction in surface area) can aid determination of the degree of sintering conducted in solid state sintering. To measure the reduction in surface area of the metallic powders, either gas adsorption or gas permeability methods can be employed. However, the particular sintering

mechanism used may still result in increased interparticle necks and decreased surface area regardless of shrinkage. This will provide data on the pattern of atomic motion across the surfaces, along grain boundaries, or through the crystal lattice.
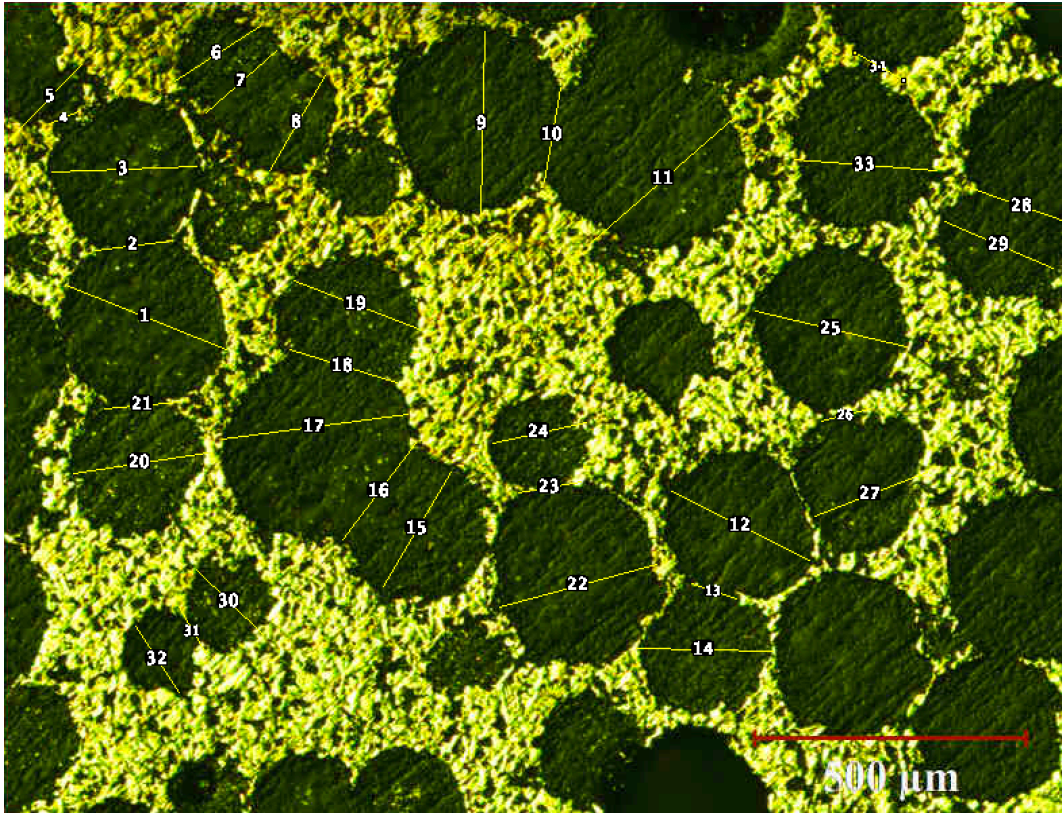
Figure 4.13 Neck Size interparticle measurement of 60% porosity titanium foam sample.
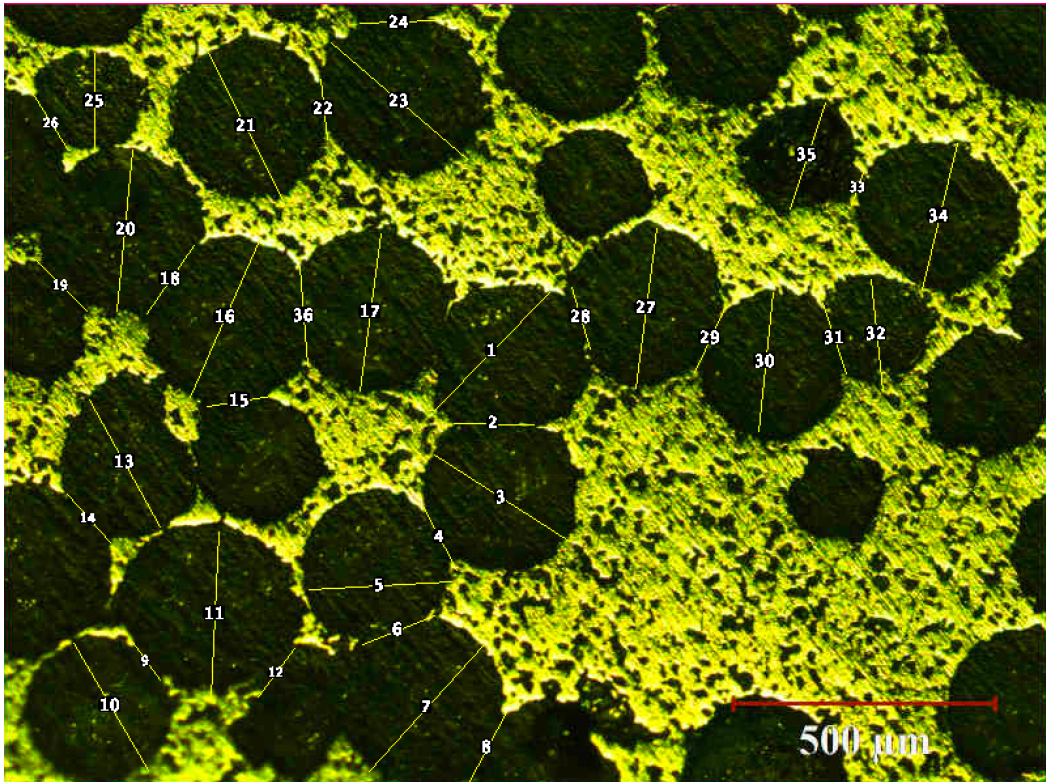
Figure 4.14 Neck Size interparticle measurement of 70% porosity titanium foam sample.
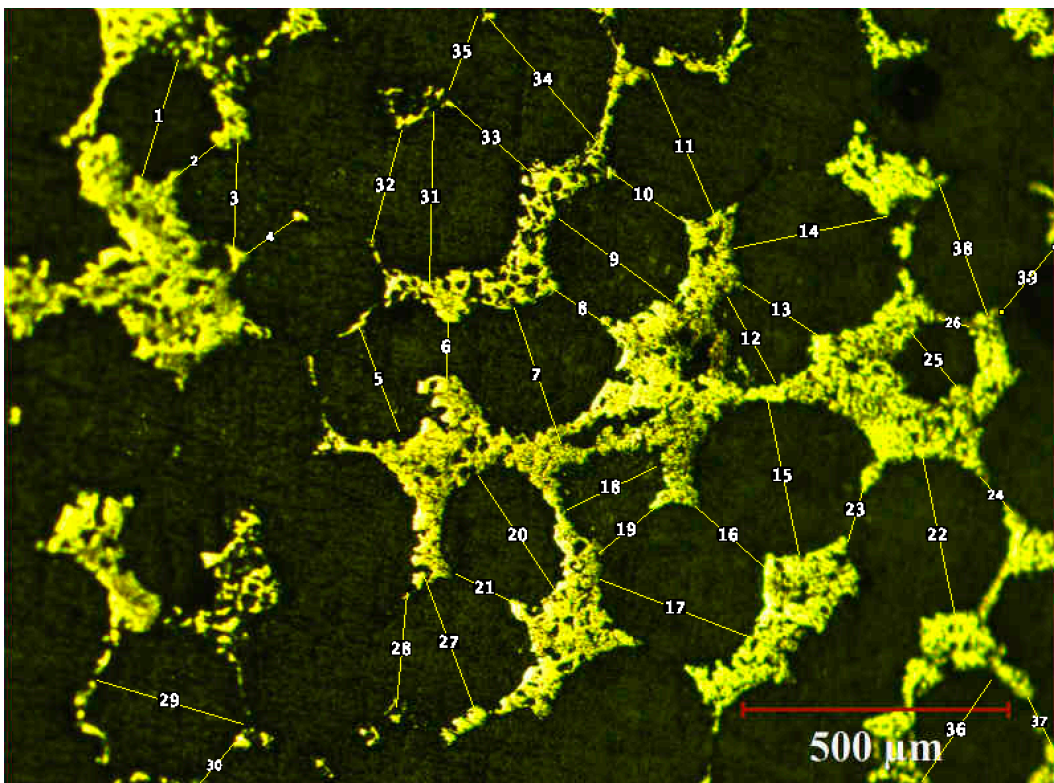
Figure 4.15 Neck Size interparticle measurement of 80% porosity titanium foam sample.

The neck size measurements of 60%, 70% and 80% porosity samples are demonstrated in Figures 4.13,4.14 and 4.15. The relationship between neck size ratio and porosity is shown in Figure 4.10. In line with predictions, there is a positive relationship between neck size ratio and porosity due to the amalgamation of pores. However, a slight decrease in neck size was observed between 60% to 70%. This is likely to be caused by unsuccessful integration.

Samples with 60% porosity showed an average neck size ratio (X/D) between 0.446 and 0.484; samples with 70% had an average neck ratio between 0.391-0.558; and for 80% porosity, the average neck size ratios were significantly larger at 0.457.
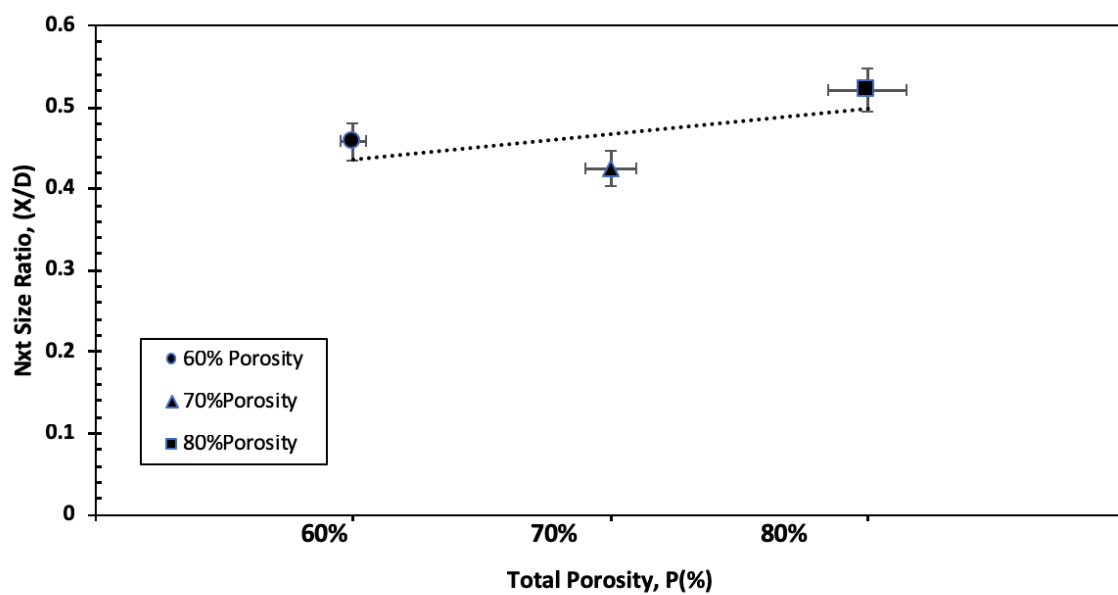
Figure 4.16 Change of neck size ratio with porosity content for 60%,70% and 80% porosity foams.

Notably, as can be observed in Fig 4.16, at 60% porosity, the observable neck sizes were larger than those displayed in foams with 70% porosity. The reason for this may be that in foams with 60% porosity, the magnesium space holder materials were better sintered than in foams with 70% porosity. In comparison, where the foam was at 70% porosity, the resultant smaller neck sizes may have resulted from a lower sintering temperature and a limited contact are prior to and during the sintering process.

Moreover, not only did neck sizes vary across the different porosity levels, region neck curvatures were also found to be inconsistent with each other. Thus, in 60% porosity foam, the neck curvatures were observed to be very sharp as a result of the impacts of different transport mechanisms during the sintering of the powder.

There may also be a relationship between neck size and strength levels in the manufactured foam. This relationship is presented in Fig 4.17. However, regardless of this, the strength of the interparticle bonds will also vary depending on the internal structures of the powders. As a result, even if powders are prepared using similar or identical methods, the resultant products may display variations in their mechanical properties due to differences in porosity.
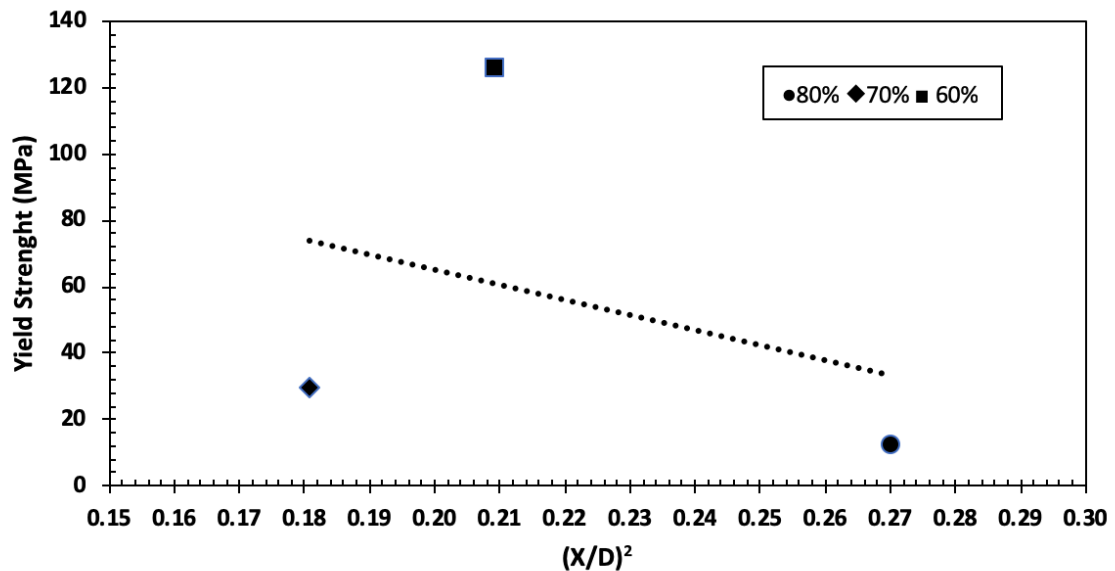
Figure 4.17 Yield Strength with function to neck size ratio for 60%,70% and 80% porosity foams.

The graph above demonstrates that yield Strength with function to neck size ratio for 60%,70% and 80% porosity foams. Where the porosity of the sample was 60%, the average yield strength was found to be 125.759 MPa while at 70% this value was observed to be 29.631 MPa. In contrast, for samples with 80% porosity levels, a lower yield strength resulted, at just 12.241 MPa.

During the initial sintering process, a rapid increase in interparticle neck size is observable, with a maximum neck size ratio (X\D) typically being measured at 0.467. During the sintering process, both surface and bulk transport mechanisms usually occur, with the dominant mechanism depending on the sintering temperature; at lower temperatures, surface transport is favoured whereas bulk transportation is more likely at higher sintering temperatures. The effect of surface transport mechanisms is usually to increase neck growth while leaving particle spacing unaffected. Examples of surface transport mechanisms are evaporation, condensation and surface diffusion. In contrast, bulk transport mechanisms tend to shrink compacts. Examples of such transportation include plastic flow, grain boundary

diffusion, viscous flow and volume diffusion. At the stage following this, the pore structure often becomes smoother and forms a cylindrical shape in which the pores are interconnected. At the last stage of the manufacturing the process, the structure of the pores alters again so that they become more spherical and closed. At this stage, grain growth can usually be observed.

4.3.3   Fracture Surface Analysis

Figure 4.18 exhibits a range of different fractured surfaces of the 60,70 and 80% porosity titanium foams. It shows that the fractures generally occur at the necks of the powders upon sintering. Furthermore, fractures generally occur over very small surface areas. A detailed inspection of the images in Figure 4.18 demonstrate that fracturing can also form dimples in the surface; these vary in size between 0.5 to 5 μm. This suggests that ductile fractures have occurred, as dimples are a general indicator of these types of fracture. Furthermore, this also shows that any oxide formation which may have occurred on the surfaces of the pores were ineffective at preventing fractures. Note that surface oxide formations are undetectable by EDS or X-ray analysis.

Figure 4.18 SEM microstructure of compressed porous titanium samples at 250x magnification with porosities of: (a) 60%; (b) 70%; (c) 80%.

83

The fractured surface area is extensive, as can be seen from Fig 4.18 (a,c). This indicates that sintering occurred at many points of interconnection between powders despite the large particle size of the powder and the low sintering temperature used in this process.

4.3.3.1 Macroscopic deformation band

Figure 4.19 exhibits the surfaces of the deformed titanium samples at 60%, 70% and 80% porosities. In these samples, the pores demonstrate minor deformations along their edges. Furthermore, while deformation bands appear in the 80% porosity samples, none appear in the samples of 60% porosity. Regardless of this, it is clear that the samples with low porosity show a degree of local deformation around the pores.

Previous research has demonstrated that deformation bands can often be strong indicators of the presence of a plateau in the compressive stress-strain curves for porous materials [22]. Such a plateau was observed in this study, and this region depicted in Figure 1, the plot for the low porosity specimens, is likely to indicate the layer by layer deformation of the sample. This process then results in the formation of deformation bands which can be observed in internal microstructures. This is in line with existing research [13].
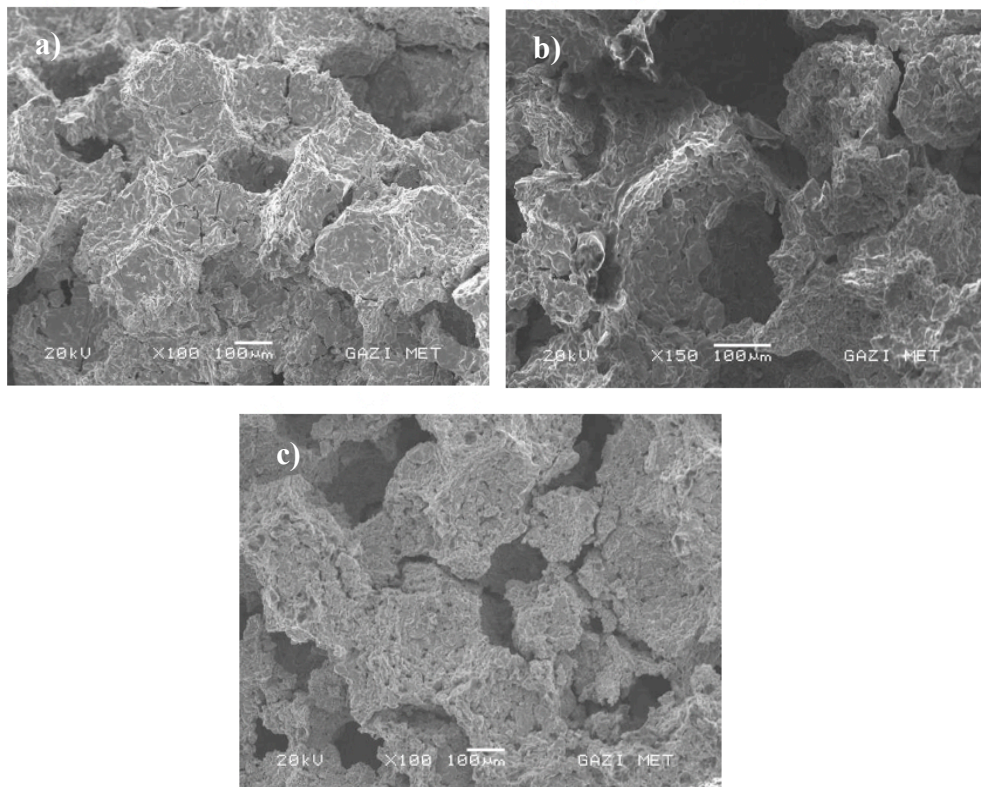
Figure 4.19 SEM microstructure of compressed porous titanium samples at 100x magnification with porosities of: (a) 60%; (b) 70%; (c) 80%.

The lack of a plateau in the stress-strain curve for the sample with 70% porosity (Fig. 4.19(b)) is likely to indicate only partial deformation around the pores and a smaller deformation band. Therefore, it is clear that there is a relationship between the porosity of the titanium and the level of deformation.

4.3.3.2 Microscopic deformation mode of cell wall

Existing studies have demonstrated that the cell wall can exhibit three separate types of deformation: bending, buckling and yielding [14]. These deformation processes are all observable in the titanium samples for all porosities, as shown in Figure 4.20.

As shown in Figure 4.20(a), bending, buckling and yielding were present in the 60% porous specimen, which is consistent with existing research on this area which has recorded bending and buckling in each cell, resulting in localised deformation [15]. On the other hand, there was no buckling and only small amounts of bending in the 80% porous sample, although the majority of the cell walls showed yielding. Visible cracks are also present in the cell walls after yielding with a 45° angle to the cell wall.
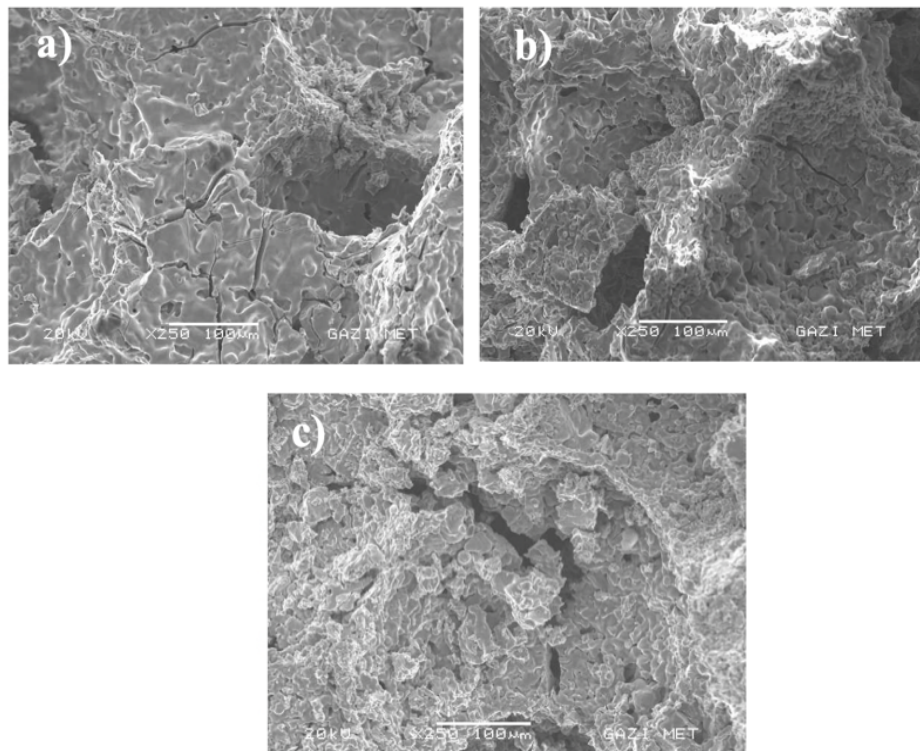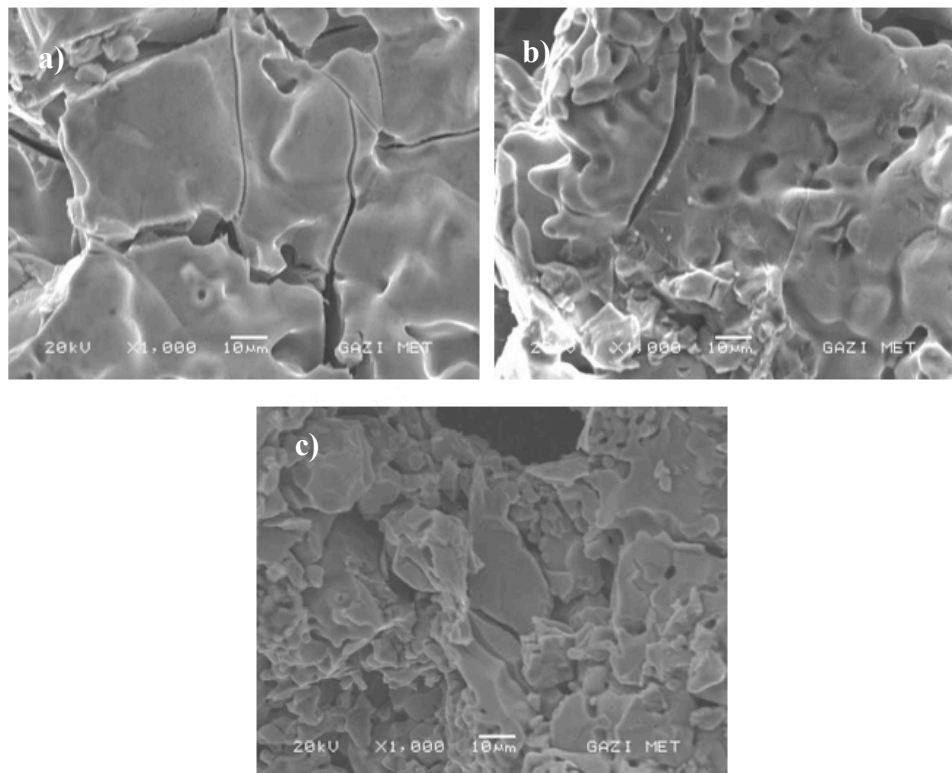

Figure 4.20 SEM microstructure of compressed porous titanium samples at 1000x magnification with porosities of: (a) 60%; (b) 70%; (c) 80%.

While the 60% and 70% porosity samples demonstrated all three forms of deformation, the 80% sample was only subject to cell walls bending and yielding. Past studies have found significant associations between microscopic and macroscopic deformation [8], showing that porous metal deformation comprises of three stages: (1) localised strain at cell nodes, (2) development of discrete concentrated strain bands, and (3) total plastic collapse. Strong local deformation typically results from cell wall buckling and bending rather than yielding, and results in deformation bands.

4.3.4 Micro Pores and Shrinkage

The present research did not specifically measure the impact of sintering factors such as time and temperature. However, the impact of porosity with regards to the sintering process were monitored.

Figures 4.21, 4.22 and 4.23 demonstrate the microstructure of pure Ti samples at 60%, 70% and 80% porosities. From these images, it is evident that pure titanium powders sinter well, as the sintering process results in the deformation of particle boundaries such that each powder particle cannot be distinguished from another powder particle. The images also display a colour gradient across the surfaces. This is likely to be caused by the presence of oxides prior to sintering, which are then spread across the surface area during the sintering process.
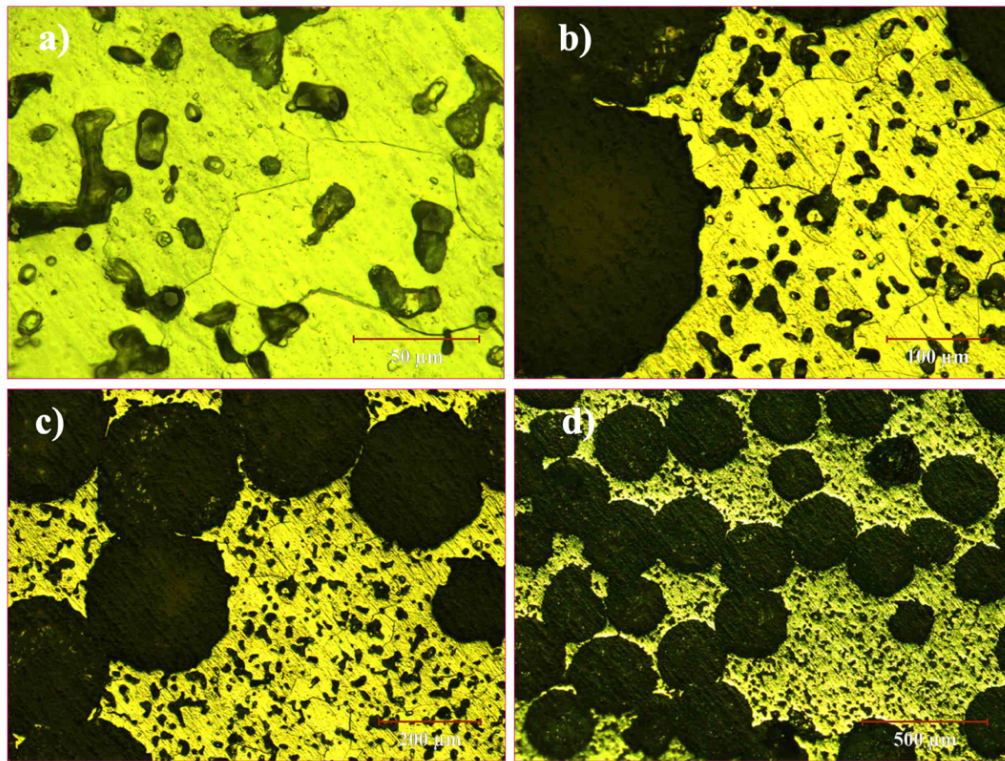
Figure 4.21 Optical macrostructure of porous titanium samples at a) 10x, b) 40x, c) 100x, d) 400x of 60% porosity titanium foams
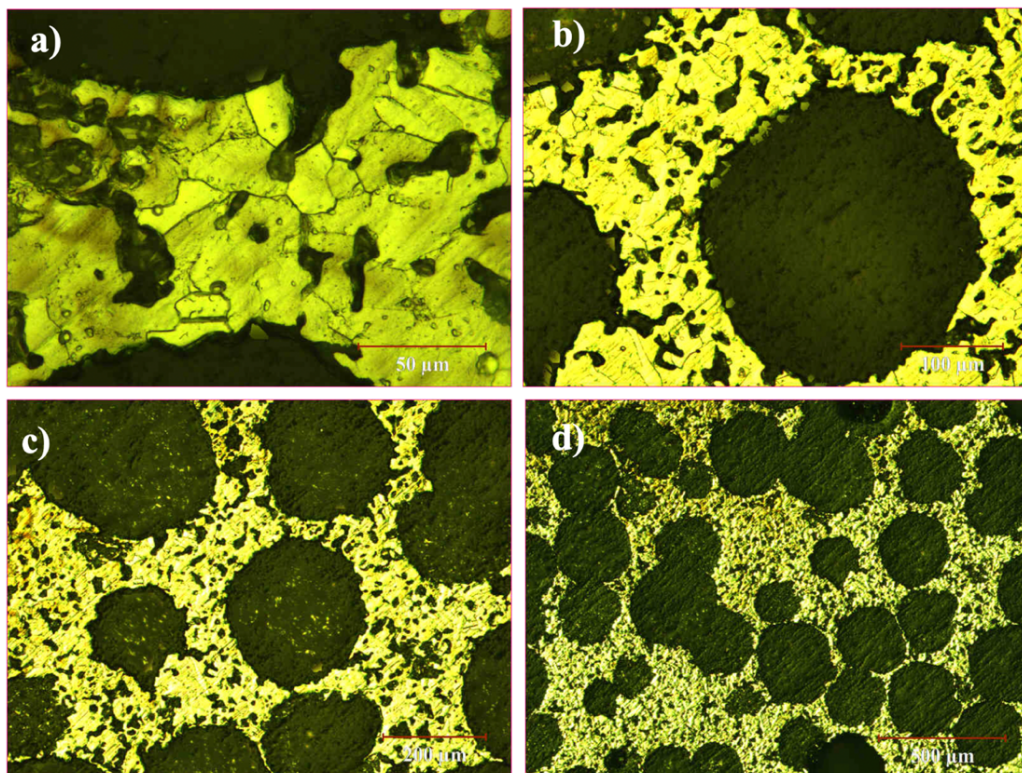
Figure 4.22 Optical macrostructure of porous titanium samples at a) 10x, b) 40x, c) 100x,d) 400x of 70% porosity titanium foams

87
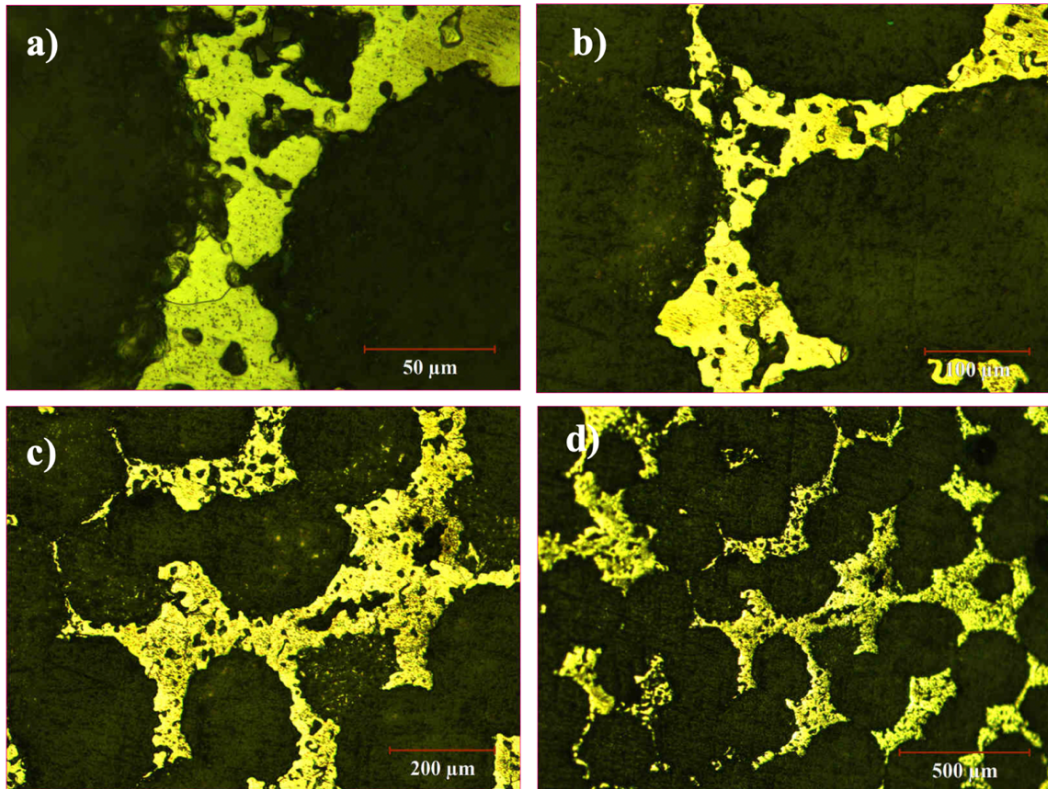
Figure 4.23 Optical macrostructure of porous titanium samples at a) 10x, b) 40x, c) 100x,d) 400x of 80% porosity titanium foams

The images also display the micropores which formed between the particles; the low compaction pressures used during sintering resulted in the generation of a high quantity of micropores. Micropores are formed as a result of vacant spaces between power particles after sintering.

Furthermore, the titanium foams of 60% porosity displayed greater shrinkage due to a smaller quantity of micropores. This is likely to have occurred because of more efficient sintering resulting from the use of smaller powders.

Through analysis via an optical microscope, it was discovered that sintering did not comprehensively deform all powder boundaries. This is evident from Figure 4.21 (b) and it is suggested that this occurred due to the particle size of the magnesium used. However, this is not conclusive, and more research is needed to confirm the specific impacts of larger spacer elements on sintering and the cooling period between beta phase to alpha phase resulting in phase transformations.

In foams with 80% porosity, the micropores were observed to be both higher in quantity and larger in size compared to the micropores formed in the 60% and 70% porosity samples: the largest micropores observed in 60% and 70% porosity samples was measured at 30 μm whereas the largest size in 80% porosity foam was 60 μm. Furthermore, in the 80% porosity samples, greater interconnection of micropores was discovered, causing the resultant shapes to be formed irregularly (Figure 4.23(a)).

These differences in micropores in the different samples is very evident when Figures 4.21(a) and 4.23 (c) are compared. It can be observed that the micropores present in the 80% sample are both bigger and more in quantity compared to those in the 60% sample. This is also the cause of the differing rates of shrinkage and variations in mechanical properties.

4.4   Effect of Immersion in Simulated Body Fluid

Simulated body fluid (SBF) (at $36.5 \pm 0.5^{\circ}C$ and pH=7.4) was used to test the biocompatibility of titanium foams. NaOH solutions were applied using the parameters identified as optimal by previous studies to generate a sodium titanate layer on the foam surfaces. The substrate used were the titanium foams with 80% porosity because of its particular mechanical properties: the open porous structure of this foam facilitates the effective transfer and penetration of the NaOH solution throughout the foam to generate homogenous coating layers. Furthermore, the elastic modulus of 80% porous foam is consistent with the elastic modulus of cancellous bone. This prevents the stress-shielding in load bearing applications. The SEM microstructures of the different samples of foam treated with NaOH-processed 80% porosity foam are presented in Figure 4.24.

Figure 4.24 SEM microstructure images of a) 60% b) 70% c) 80% d) 80% with NaOH coating titanium foam samples at 1000x magnification in as received state.

As previously noted, the porous nature of titanium foams is useful in facilitating the regulation of mechanical properties. They can therefore alleviate the stress-shielding problem which often occurs in titanium foams. Furthermore, the porous structure allows for the ingrowth of bone and the transport of body fluids in biomedical applications due to the open nature of the foam. However, the titanium foams are inefficient inducers of the direct attachment of bone tissue to surfaces. Therefore, the pore surfaces must be altered by surface processing to encourage the attachment of bone tissues.

When bioactive materials come into contact with SBF, they form apatite layers which allow artificial implants to attach to living bone [76]. The different samples were therefore tested for bioactivity by measuring the surface apatite formation over 14, 21 and 28 days in SBF.
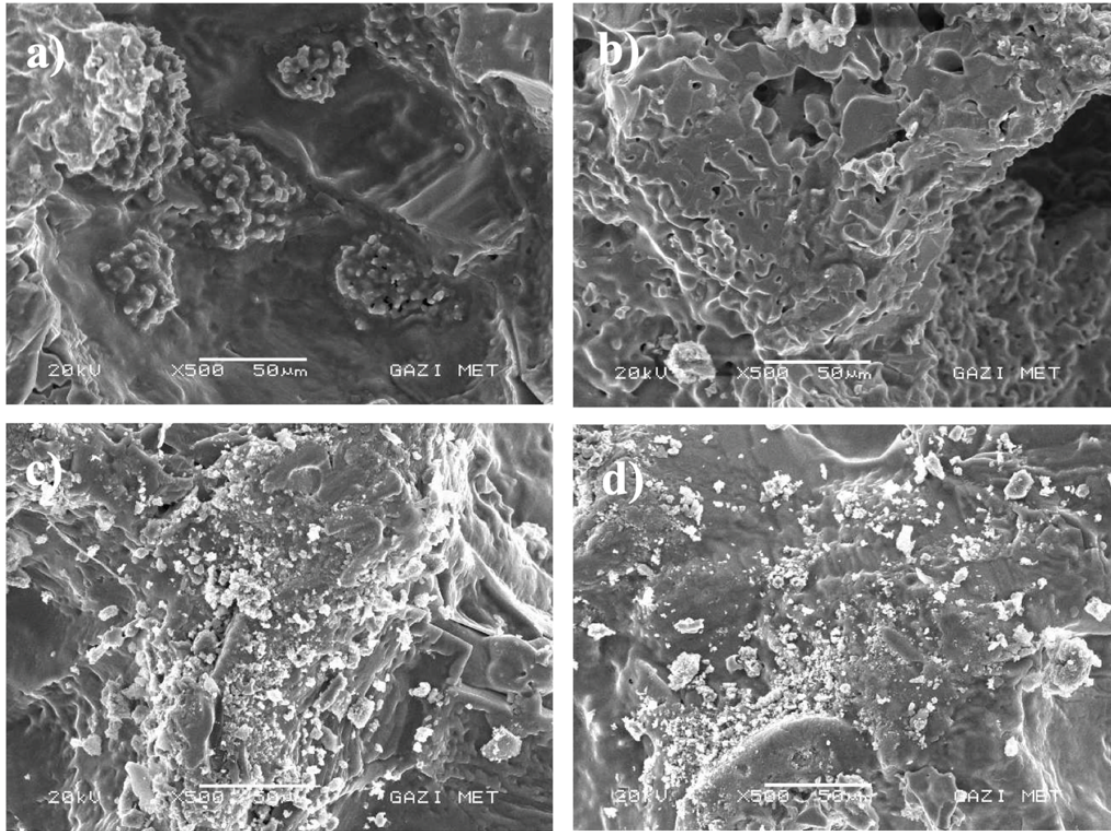
Figure 4.25 SEM microstructure images of a) 60% b) 70% c) 80% d) 80% with NaOH coating titanium foam samples at 1000x magnification with 14 days of immersion.

Figure 4.25 displays the surface structures of the titanium foams both prior to and following immersion in SBF for 14 days. It can be seen that the surface morphologies of all the porous samples were altered in some way following the exposure to SBF for 14 days, with a particularly significant lack of formation of white precipitation in the 70% sample in particular. The number and size of the precipitate formed was greatly contingent on whether the surface was treated with NaOH; in untreated samples, there were relatively small particles on the surfaces of the 60% and 70% porosity samples. On the other hand, the treated samples displayed the formation of coarser particles. This is evident from the images of both the 80% porosity and the NaOH-treated 80% porosity foams.

The formation of precipitation requires a nucleus to grow around. Therefore, it was expected that the initial precipitates would be uneven on the surface of the foam samples. After the process had begun, the lower surface energy facilitated that formation of precipitates at the sites where precipitate already existed. Therefore, the precipitate tended to form in clusters. The rate of growth is then measured in relation to the changing morphology and size [18, 19]. This was observed in the samples submerged for 14 and 21 days due to the first rate of

deposition. In the 80% porosity sample, the high porosity microstructure is observable as a larger number of stress concentration points resulted in better mechanical properties.
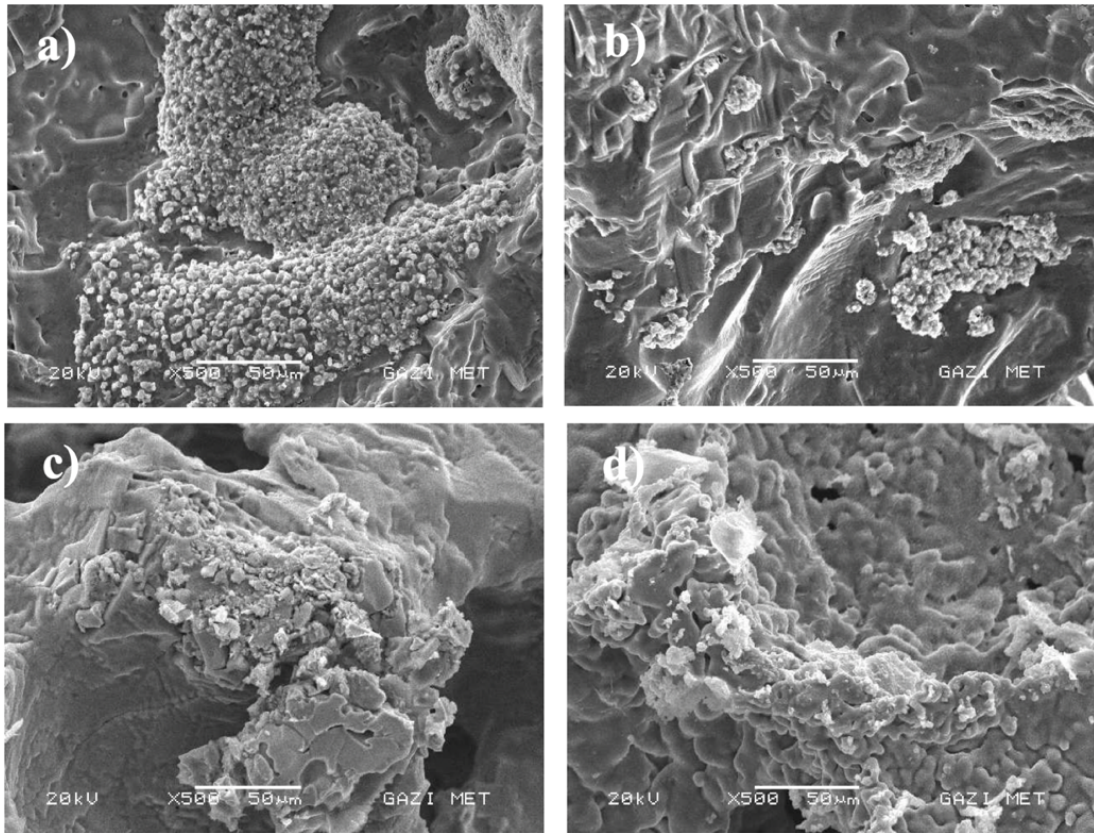
Figure 4.26 SEM microstructure images of a) 60% b) 70% c) 80% d) 80% with NaOH coating titanium foam samples at 1000x magnification with 21 days of immersion.

When examining all samples across the 14, 21 and 28 timespans, the prevalence of precipitation produced was used to indicate the rate of positive change of the osteointegration of the samples. As evident from Figures 4.25 and 4.26, the precipitate which formed between day 14 and day 21 was rather uneven on the surface of the titanium foam. Analysis of the development of the precipitation showed that the precipitation formation became increasingly uniform as time progressed. The morphology of the apatite precipitate formed by contact with SBF depended on the composition of the titanium foam [20].
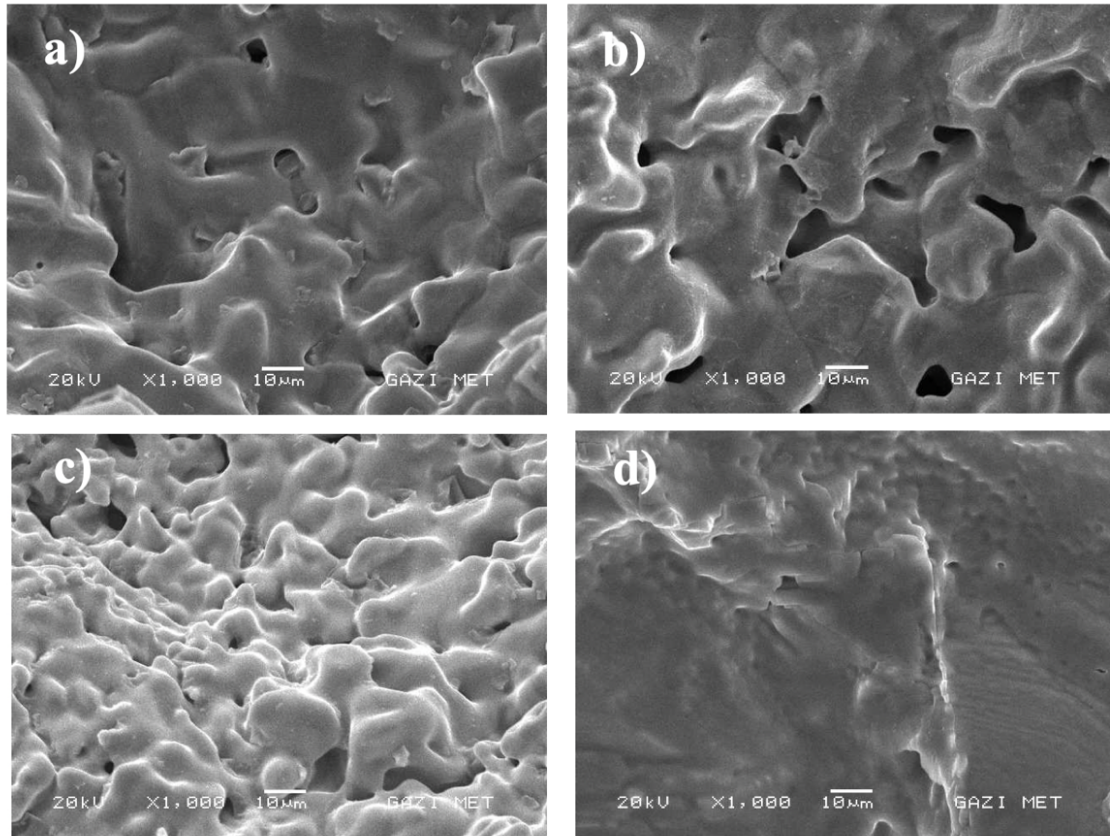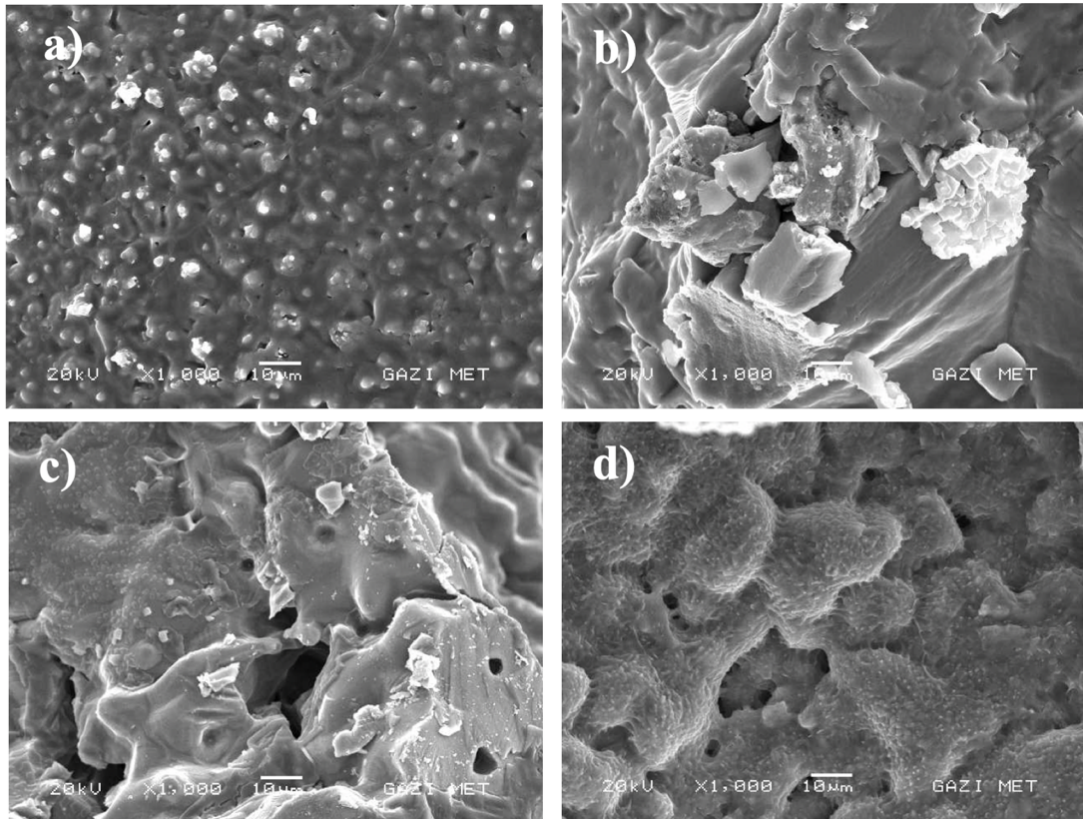
Figure 4.27 SEM microstructure images of a) 60% b) 70% c) 80% d) 80% with NaOH coating titanium foam samples at 1000x magnification with 28 days of immersion.

Between days 21-28, there was significant variation in the amount of precipitation produced. Therefore, the direct relationship between the cycles of deposit and the period of immersion was not determinative in this case, in contrast to the research conducted by Hsu et al [22]. As is shown in Figure 4.27, the subsequent 28-day immersion resulted in an almost homogenous filling of pores and significant in-growth on the foam surfaces. The boundaries between the particles of the 60% and 80% porosity samples were very clear, meaning that these samples behaved as bulk materials rather than porous materials with areas of stress concentration.

The amount of precipitation produced was dependent on when the sample was removed from the SBF. This is because deposition arose in a cyclical pattern. As immersion time increased, the precipitates altered in structure from irregular to regular rhomboid shapes. This resulted from the generation of energetically beneficial nucleation sites on the particles. However, following this deposition creating a smooth surface with well-defined boundaries, the deposition cycle initiates again on the resultant precipitate surface.

4.5   Mechanical Properties

Compression tests were used in this study to measure the mechanical properties of the titanium foams. Resultant stress-strain curves were produced which present the elastic moduli and the strengths of foams. Typical stress-strain curves for the 60, 70 and 80% porosities are shown in Figures 4.28,4.29 and 4.30 respectively. A significant difference in stress-strain properties were clearly seen in the figures below.
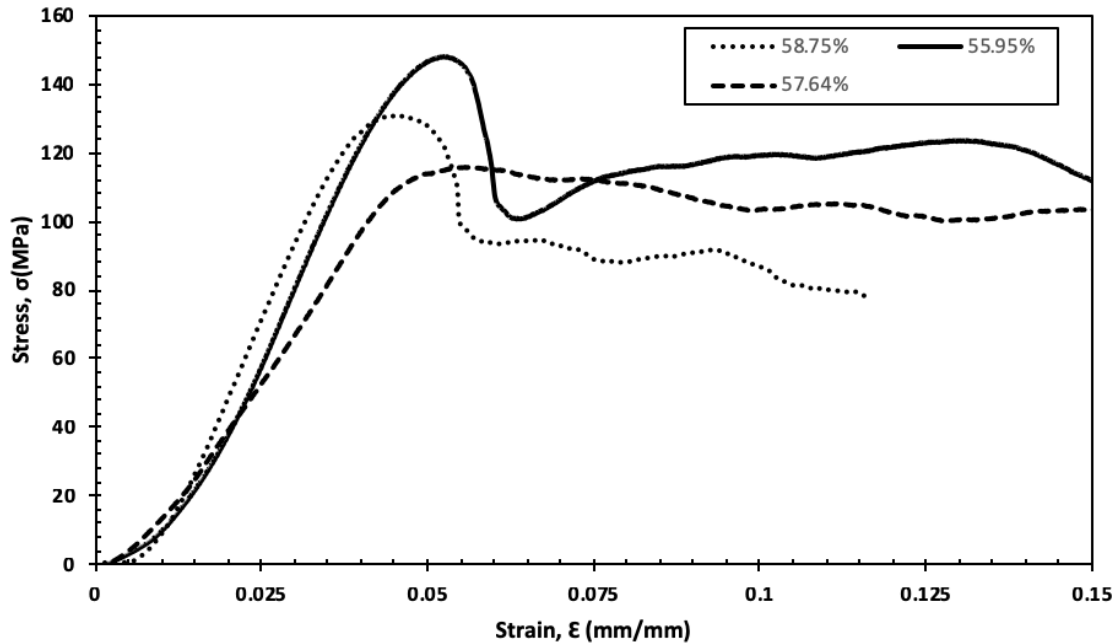
Figure 4.28 Compressive stress-strain curves of 60% porosity titanium foams.
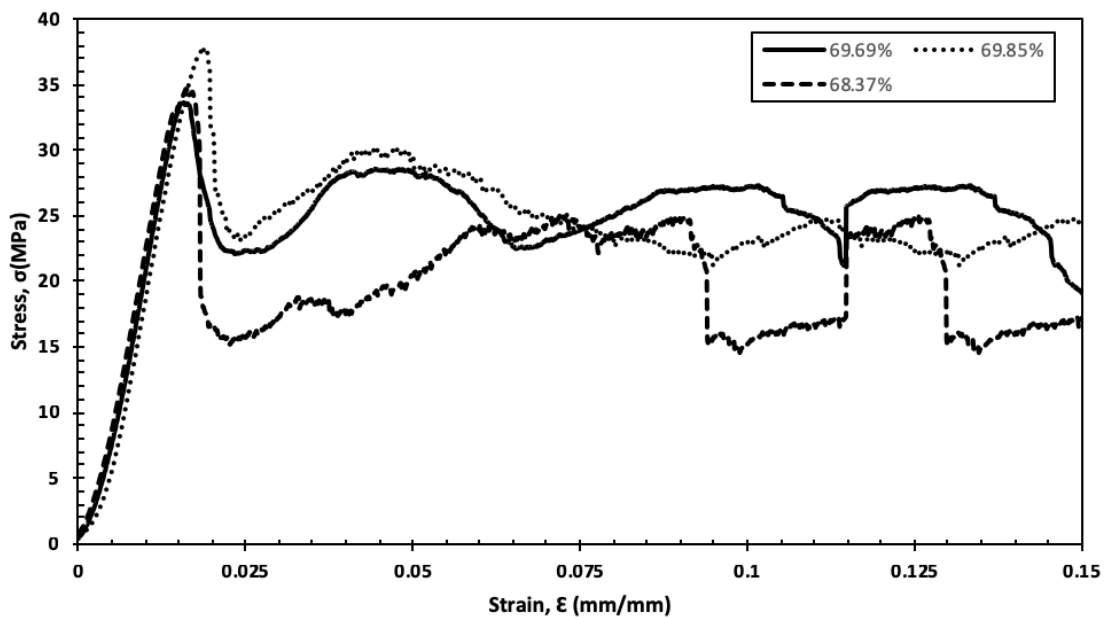
Figure 4.29 Compressive stress-strain curves of 70% porosity titanium foams.
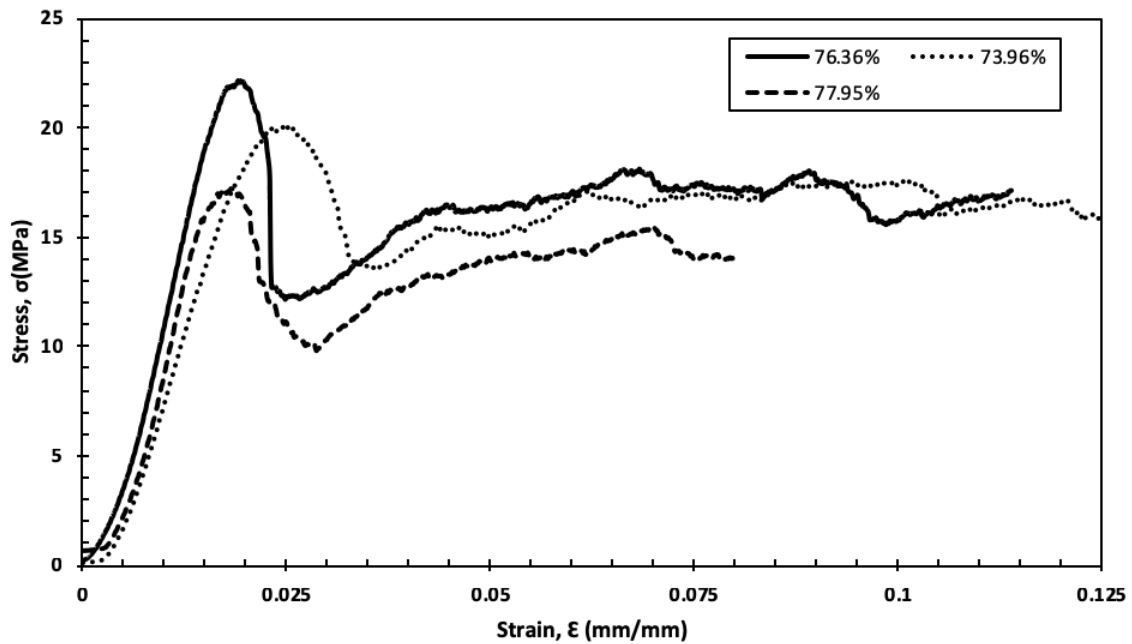
Figure 4.30 Compressive stress-strain curves of 80% porosity titanium foams.

As load is increased, the cell edges and walls of weaker areas in the foam will begin to buckle. This results in a deformation band perpendicular to the loading direction as the plasticity of cells begins to collapse. This can be identified in the stress-strain curves as the plateau region. Open-cell foam will exhibit plastic collapse where the force on the cell walls is greater than the fully plastic moment creating plastic hinges. However, in the case of closed-cell foam, plastic collapse may be affected by a range of factors such as the bending and stretching of cell walls and the effect of fluid within cells. The cellular structure and the properties of the solid will determine the shape of the plateau on the stress-strain curve, as it can vary between flat and sloped, or a mix of both.

The maximum compressive strengths were measured at 147.814 MPa (60% porosity), 37.874 MPa (70% porosity) and 22.103 MPa (80% porosity). The minimum measured compressive strengths were 115.963 MPa (60% porosity), 33.631 MPa (70% porosity) and 16.027 MPa (80% porosity). Thus, the mean compression strength rates were calculated as 131.889 MPa, 35.752 MPa and 19.065 MPa for 60%, 70% and 80% group porosity samples, respectively. The low strengths of 80% porous samples is due to the high porosity of the foam.

As strain increases in the plateau region, more deformation bands develop as increasing numbers of cells collapse to reach maximum densification. The densification occurs following a plateau due to the compression of the solid as opposing cells collapse. The

95

resultant increase in the compressive stress on the strain curve is known as the densification strain [67]. The densification strain formed will depend on cell structure. From analysis, it can be seen that densification began earlier in all lower porosity samples than was predicted.

The stress-strain curves plotted for the 60% porosity foam samples were relatively smooth, showing more defined plateau regions than the graphs of 70% and 80% porosity samples. This is because of the malleable nature of pure titanium. Furthermore, as was predicted, a decrease in sample porosity resulted in a decrease in densification strain because foams with an open-cell structure are more likely to collapse during compression.

As is observable in the 60% porosity samples, a decrease in sample porosity also results in a decrease in plateau region. Simultaneously, the stress after yielding increases significantly. This may signal of closed cell morphology as the cell faces are subjected to membrane stress.

Similar effects were observed in the 80% sample; there was an increase in stress subsequent to yielding with an increase in strain at low porosities. As is evident from the imaging, the compression stress-strain curves of the 80% porosity foams showed linear elastic behaviour when small strains were applied. This was then followed by yielding and increase of strain until the ultimate stress was reached. After the maximum stress, fracturing occurred rapidly. These internal breakages may then cause the material to soften.

The foams at 70% porosity behaved differently as they exhibited a drastic decrease in stress following plastic deformation (Figure 4.29). As the porosity was decreased, the appearance of a number of serrated regions were observable. When compressed, the cell walls of the 70% foam generally fractured locally in a brittle manner. The fractured material then dispersed to the surrounding areas as compression continued. In some foam samples, during the plateau region a zig-zag shape was seen.

The deformation mechanism and plastic response of the foam samples are affected by the cell wall geometry and material characteristics during compression loading. Titanium foams tended to exhibit a number of deformation of bands when compressed which were formed in the direction of the applied load. On the other hand, when cells collapsed, these occurred in discrete bands. It is likely that the presence of weak cell walls begins the strain localisation process. Following this, the deformation process continues to spread throughout the foam. This produces a band of collapsed cells. After all of the cells have collapsed in a particular

region, there will be further deformation as new bands are developed in new positions. It was further discovered that a decrease in foam porosity resulted in fewer surface cracks as well as the formation of larger pores which were positioned at a 45º angle to the loading direction.

4.5.1 Elastic modulus

Figure 4.31 shows the elastic moduli of the titanium foam samples. In the current study, the elastic moduli were measured from the slopes of the linear elastic regions. Thus, for the first group of samples (55.95%—58.76% porosity) the elastic moduli were 3.059—4.468 GPa, while the second group of samples (68.37% to 69.69% porosity) had elastic moduli of 2.537—2.821 GPa and the third group of samples (76.36%—77.95% porosity) displayed elastic moduli in the range 1.163—1.709 GPa. The conclusions drawn from this evaluation that there was an inverse relationship between elastic modulus and porosity, as the greatest elastic modulus of 4.468 GPa was obtained for the sample with 58.76% porosity. Furthermore, as the porosity increased to 77.95%, the resulting elastic modulus was a mere 1.168 GPa. This pattern was consistent through the porosities 69.69%—73.96% as they displayed elastic moduli less than or equal to 2.8 GPa. The mean elastic modulus rates were calculated as 4.016 GPa, 2.826 GPa and 1.383 GPa for 60%,70% and 80% group porosity samples, respectively.
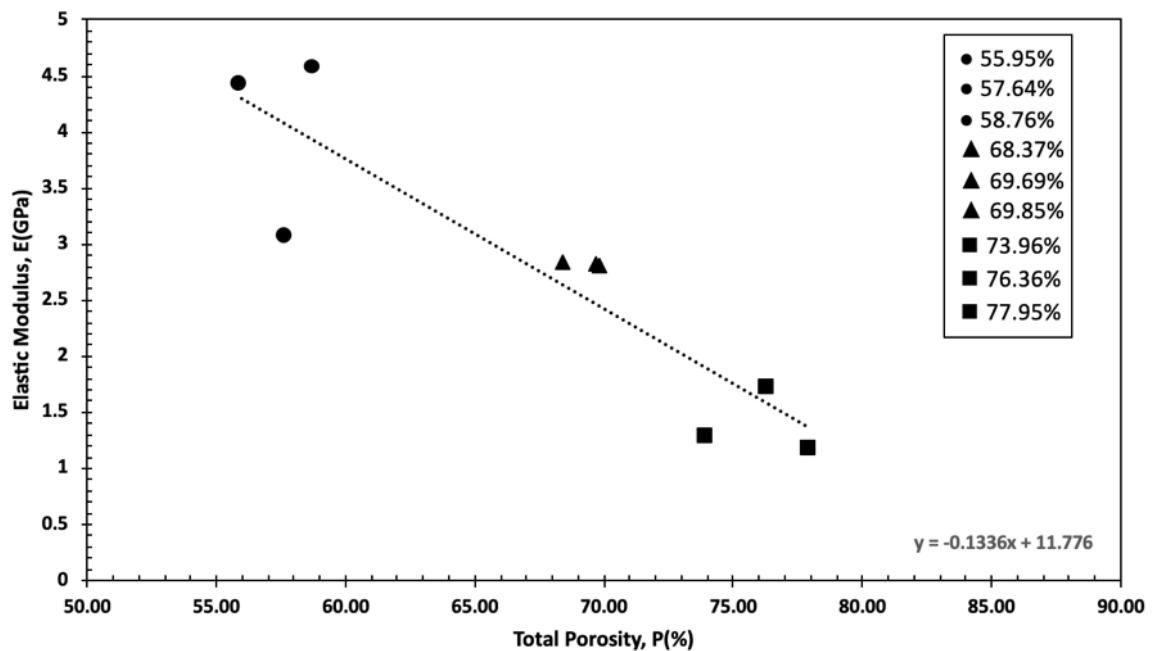
Figure 4.31 Elastic modulus of porous titanium with as function of porosity.

As can be seen from the stress-strain plots of all foam samples, while the initial loading is elastic, it is not optimally linear. This is because of the presence of imperfections in the foam which decrease the stiffness and strength of the sample. These decreases may have resulted from cell edge curvature, uneven density, and concentration of materials at cell nodes instead of at cell edges. To calculate the actual modulus, dynamic measuring must be carried out. Alternatively, the foam could be loaded into the plastic range before it is unloaded, to measure the module from the unloading slope.

Moreover, when the foams were loaded, there was a concentration of stress upon the porous structure which resulted in early yielding at isolated locations. This produced smaller slopes in the elastic regions than was anticipated. Therefore, the unloading modulus, E, is predicted to be significantly higher than the initial loading line after a plastic strain of 0.2% is applied. Even where strain is applied to bulk polycrystalline materials, the elastic modulus has a lower value than the expected value because dislocations occur more naturally in some grains than in others. Thus, the calculated yield point at 0.2% strain is an average yield point of the titanium particles.

Regardless, the unloading moduli at 0.2% strain are greater than the initial loading value due to the elimination of stress on the weak areas during the first compression process. On the other hand, the unloading moduli were found to decrease in all foam samples as the strain was increased because of deformation mechanisms such as bending, buckling, stretching and cracking of cell edges and cell walls. As a result, the unloading Young's Modulus varies depending on strain. Typically, the Young's Modulus value will decrease faster when measured in relation to compression strain than in relation to tension. As cell edges and walls deform, stiffness will decrease. On the other hand, stretching increases stiffness which can lead to fracturing of cell walls during tension loading.

4.5.2 Yield strength

Figure 4.32 shows the yield strength of the different titanium samples. The graph displays that increased porosity results in decreased yield strength: the specimens with porosities of 55.95% to 77.95% displayed yield strength of 14.063—90.263 MPa. The first group of samples (55.95%—58.76% porosity) demonstrated yield strength in the range of 75.373 — 90.263 MPa, while the second group samples (68.37% to 69.69% porosity) had yield strength between 24.744—17.346 MPa. Finally, the third group of samples (76.36%—

77.95% porosity) displayed yield strength in the range of 17.080—14.063 MPa. The mean yield strength rates were calculated as 871.336 MPa, 20.053 MPa and 15.733 MPa for 60%, 70% and 80% group porosity samples, respectively.
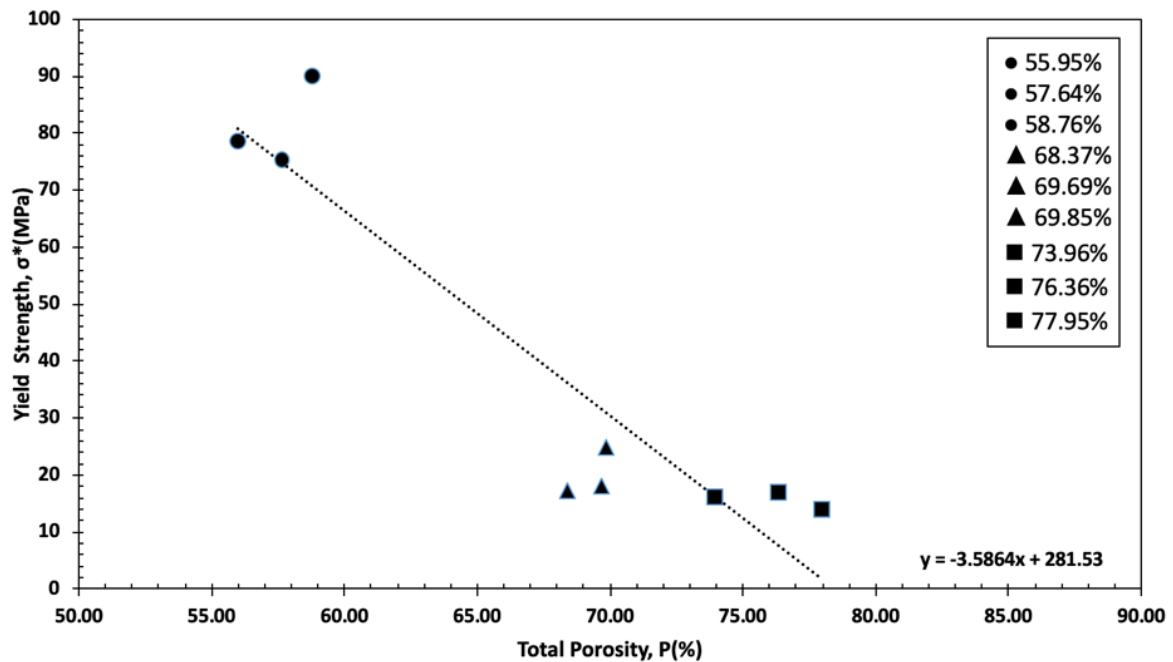
Figure 4.32 Yield strength of porous titanium with as function of porosity.

Analogous to the graphical representation of the relationship between porosity and elastic modulus, yield strength and porosity also display a negative correlation. This exhibits that implants constructed from bulk materials with greater compressive strengths than bone ae inefficient in transferring the requires stress to adjacent bone. As a result, the surrounding bone is more likely to reabsorb any stress, causing the implant to become loose and less effective. This will ultimately lead to revision surgery. Therefore, it is crucial that materials with comparable mechanical properties to human bone are used to create implants. These properties will need to demonstrate high strength and a low elastic modulus [13]. The bulk materials currently used to create implants are stiffer than the surrounding human bone. As mentioned above, these are ineffective at transferring the necessary amount of stress to the bone around the plant, resulting in desorption of the bone, ultimately causing the implant to become loose. To remedy this, ideal implant materials must be found which have the idea combination of high compressive strength and low elastic modulus to reduce the likelihood of necessary revision surgery [5].

Human bone has compressive strength values between 4 and 180 MPa [12] and human cortical bone has elastic moduli of 12-17 GPa. This value for human cancellous bone is

generally below 3 GPa [1]. The titanium samples tested in this study exhibited similar compressive strengths and elastic moduli: the porous Ti samples displayed decreasing compressive strengths of 147.814 MPa - 16.027 MPa along with elastic modulus of 4.468 GPa – 1.163 GPa and yield strength of 90.263 MPa—14.063 MPa with increasing porosities (60%,70% and 80%). The porous titanium samples therefore may be useful as biomedical implants given the wide range of compressive strengths measured and the similarity of the titanium elastic moduli and yield strengths to human bone.

4.5.3 Hardness testing

To measure indentation hardness, an Emco Test Duravision 2000 microhardness examiner machine was used in conjunction with a Vickers diamond pyramid indenter. For each sample, an average of 15 readings were taken. The results of these tests are demonstrated in Figure 4.33.
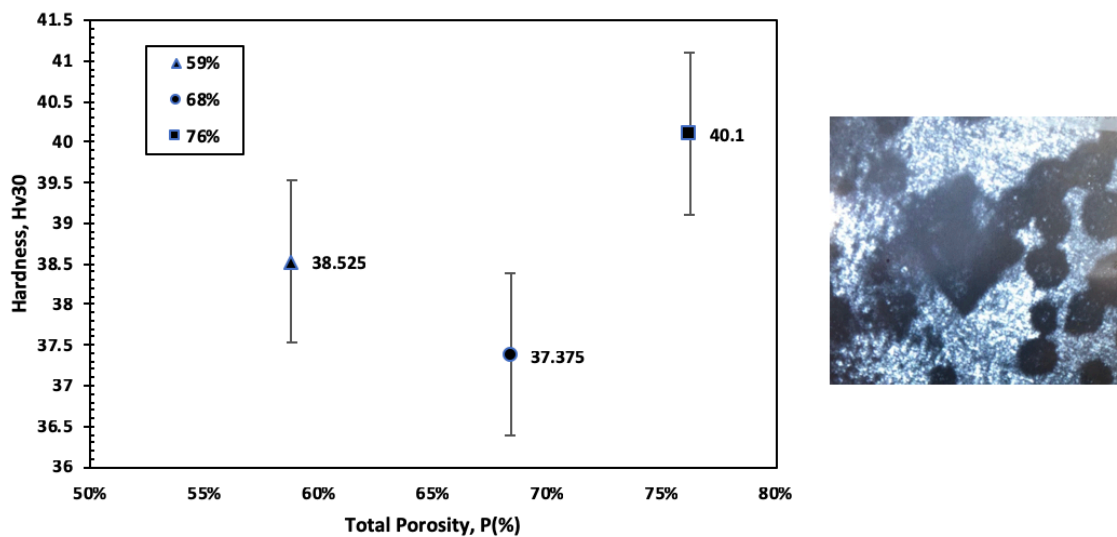
Figure 4.33 Hardness values of specimens with 60%,70% and 80% porosity foams and their optical image micrograph of the Vickers indentation.

The surfaces of the polished samples were subjected to testing by the Vickers hardness test. These tests were performed on random areas of the surface. A load of 100g was applied. As has been graphically demonstrated, the there was a strong positive correlation between porosity and hardness, as was predictable due to the effect of the proportion of α phase: α phase is widely recognised as having a greater elastic modulus than β phase. 70% porosity foams demonstrated the lowest hardness (37.375 HV), with 60% porosity foams showing a moderate hardness (38.525 HV), and 80% porosity foams exhibiting the greatest hardness at

40.1 HV. This pattern may have been caused by the closer proportions of α phase in higher porosities. This leads to a greater likelihood of measuring higher hardness levels. The result also indicates that the specimens are more homogenous in α phase.

4.6 Finite Element Modelling

4.6.1 The structure of porous Ti

The FEM structures of the titanium samples at 60%, 70% and 80% porosity are demonstrated in Figures 4.34 and 4.35. It shows that pores were observable with a similar size and morphology compared to the magnesium space holders. Both macropores (caused by the magnesium particles) and micropores ($\sim 11\mu$m) are present, with the latter being caused by voids between titanium powder particles.
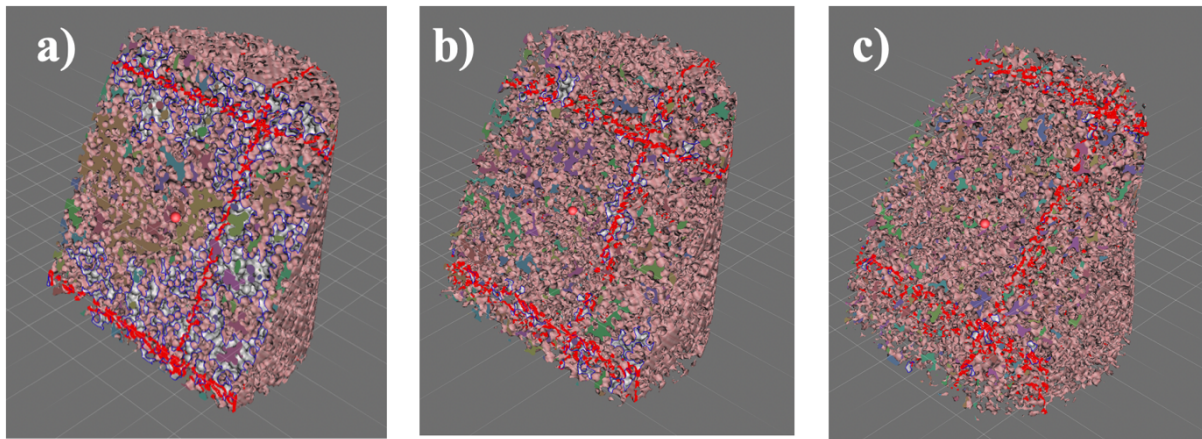
Figure 4.34 FEM microstructure of porous titanium samples at 45 degree angle with porosities of: (a) 60%; (b) 70%; (c) 80%.

The 3D model reconstructed from the micro-CT images can be used to calculate the relative density of each sample as 44.04% (60% porosity), 30.13% (70% porosity) and 23.64% (80% porosity), which further supports the presence of macro-pores. The difference in the values of porosity obtained from the experimental and micro-CT data can be explained by the presence of the micropores, which the micro-CT machine was unable to resolve due to its resolution level.
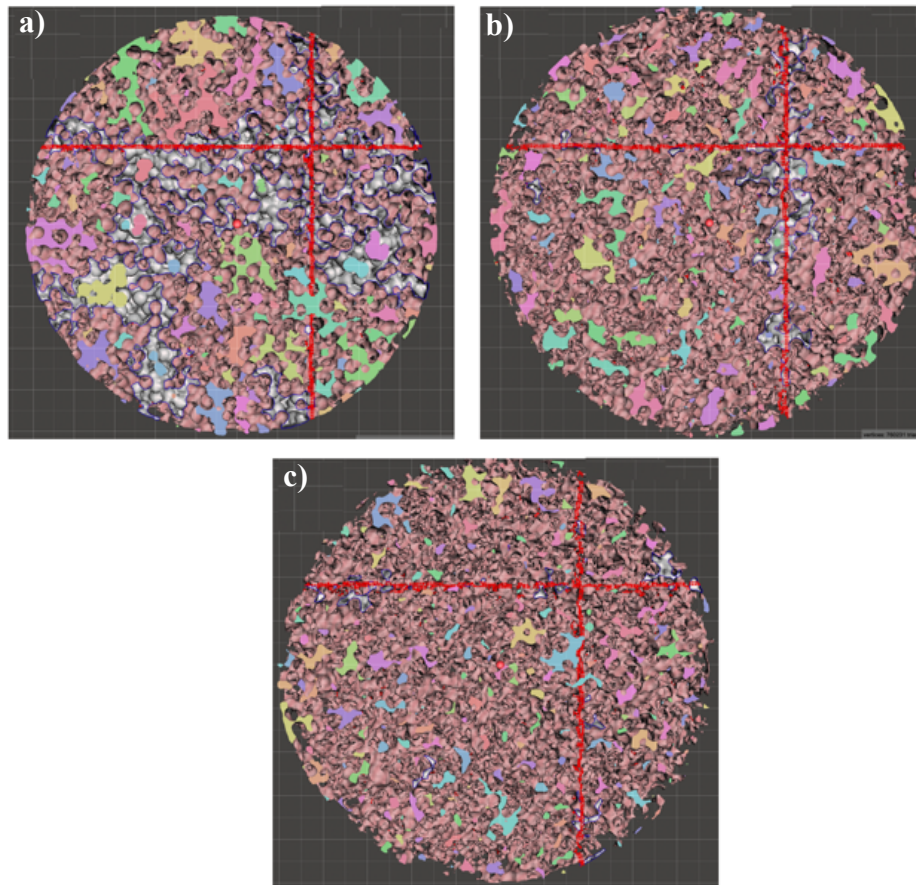
Figure 4.35 FEM microstructure of porous titanium samples with porosities of: (a) 60%; (b) 70%; (c) 80%.

4.6.2 Compression test and FEM simulations

The measurements obtained from experimental tests were inputted to create FEM simulations in order to investigate the elastoplastic properties of the titanium foam samples. Figure 4.36 displays the results obtained of both the experimental and FEM simulated compression tests on the 60%, 70% and 80% porosity samples. The experimental compressive strengths were 147.81 MPa (60% porosity), 33.54 MPa (70% porosity) and 17.24 MPa (80% porosity), while the compressive strengths of the corresponding FEM simulated Ti foams were respectively 145.5 MPa, 36.2 MPa, and 15.6 MPa. As can be observed, the samples with the highest porosities also exhibited the lowest compressive strengths in both forms of test.
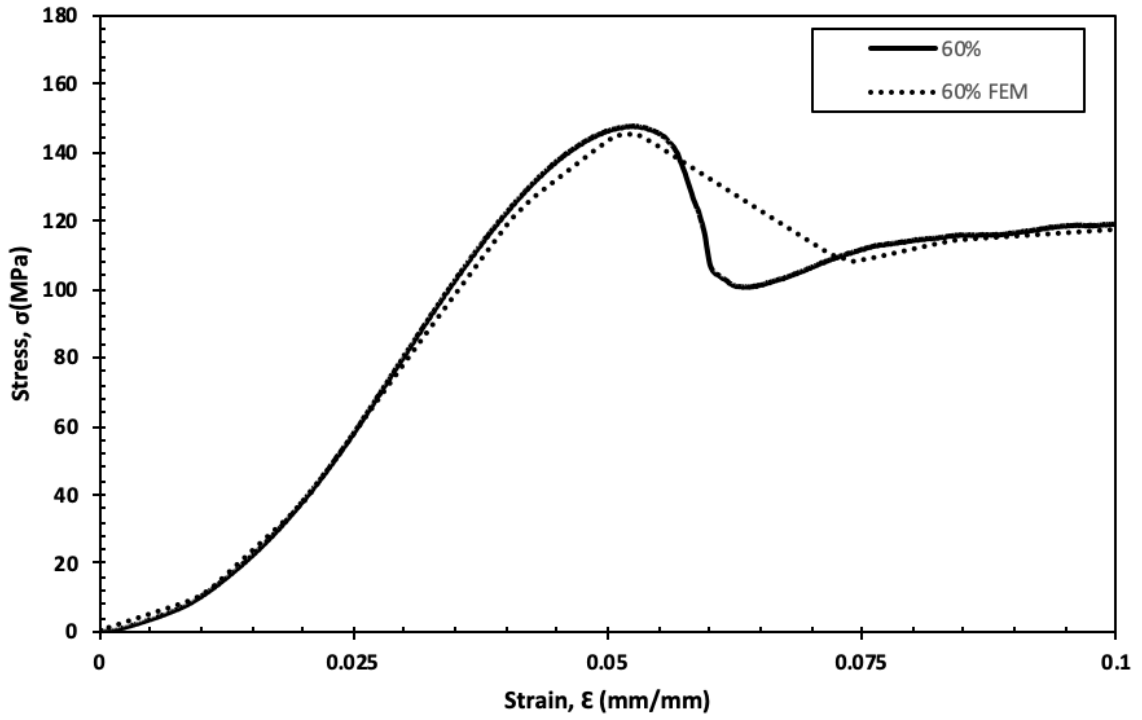
Figure 4.36 Compressive stress-strain curves of porous titanium samples vs FEM Models with 60% porosities.
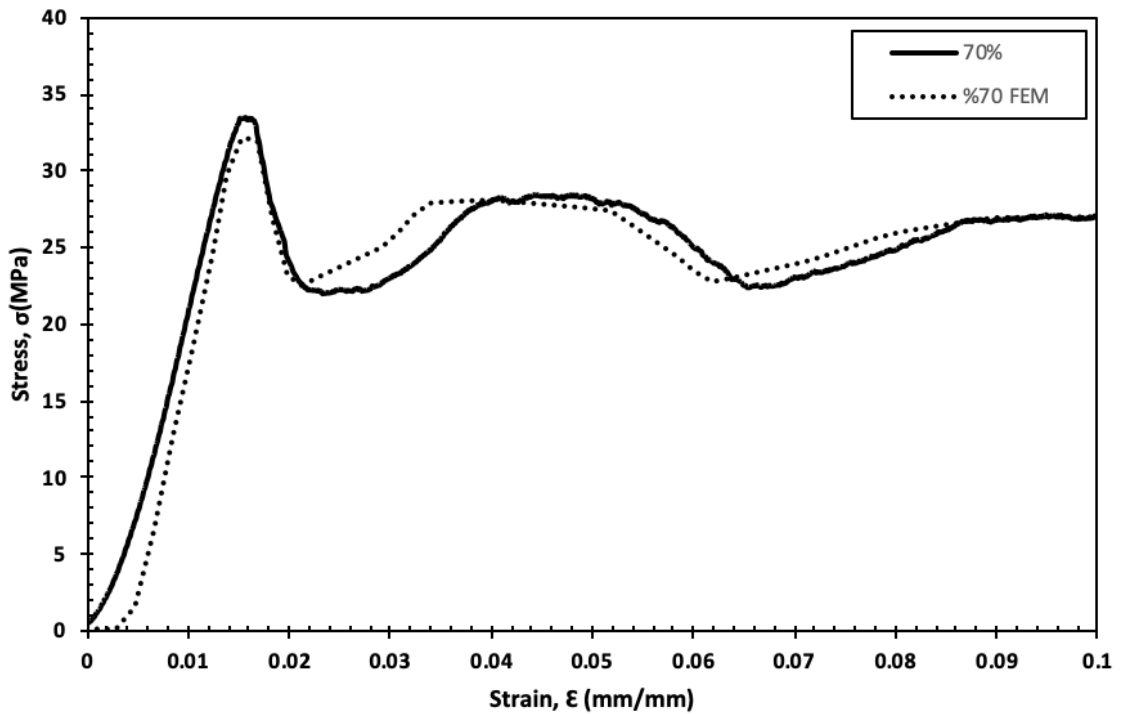
Figure 4.37 Compressive stress-strain curves of porous titanium samples vs FEM Models with 70% porosities.
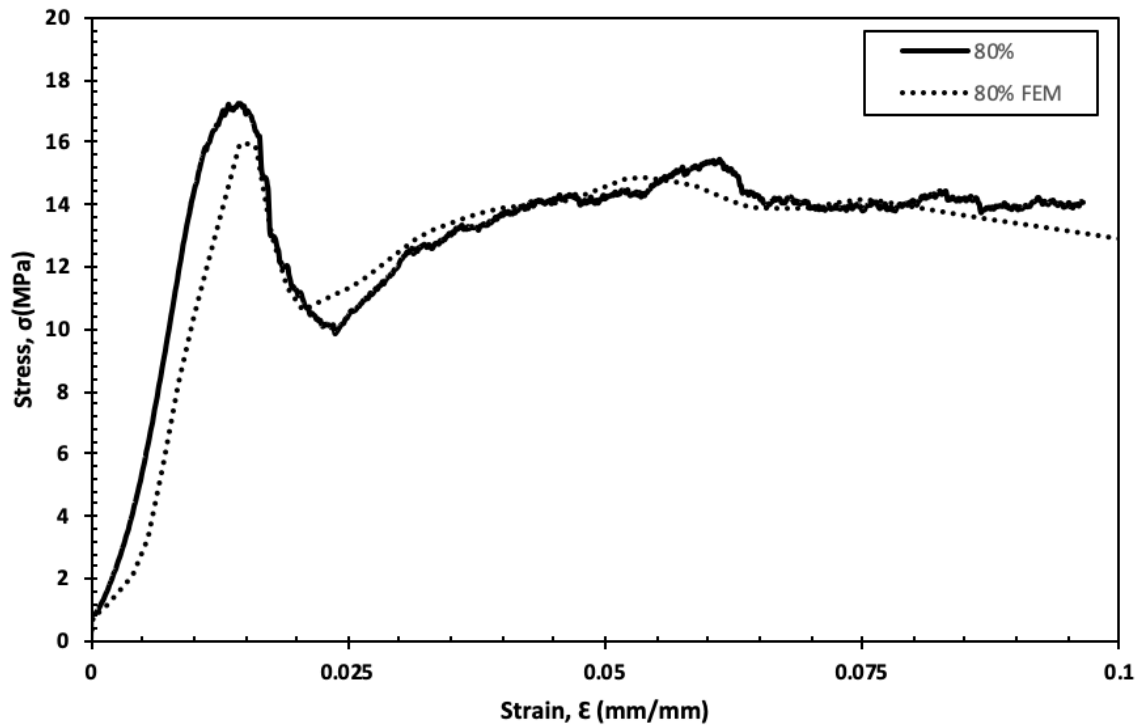
Figure 4.38 Compressive stress-strain curves of porous titanium samples vs FEM Models with 80% porosities.

As is evident from the figures above, the compressional stress-strain curve obtained in relation to the 70% and 80% porosity samples were consistent with measurements from experimental data. The experimental yield strengths were represented in figure 4.39. The experimental tests resulted yield strengths of 85.75 MPa (60% porosity), 19.54 MPa (70% porosity) and 13.88 MPa (80% porosity), while the corresponding FEM model yield strengths were 80.34 MPa, 22.82 MPa and 10.63 MPa, indicating relative errors of 6.73%, 16.54% and 23.46%, respectively. Thus, the FEM model predictions for the 70% porosity titanium sample were higher than the experimental value obtained. The opposite was the case for the 60% and 80% porosity samples as the experimental values were higher than the FEM predicted values. This is likely to have been caused by the variance in the experimental test yield point and the FEM simulation yield point.
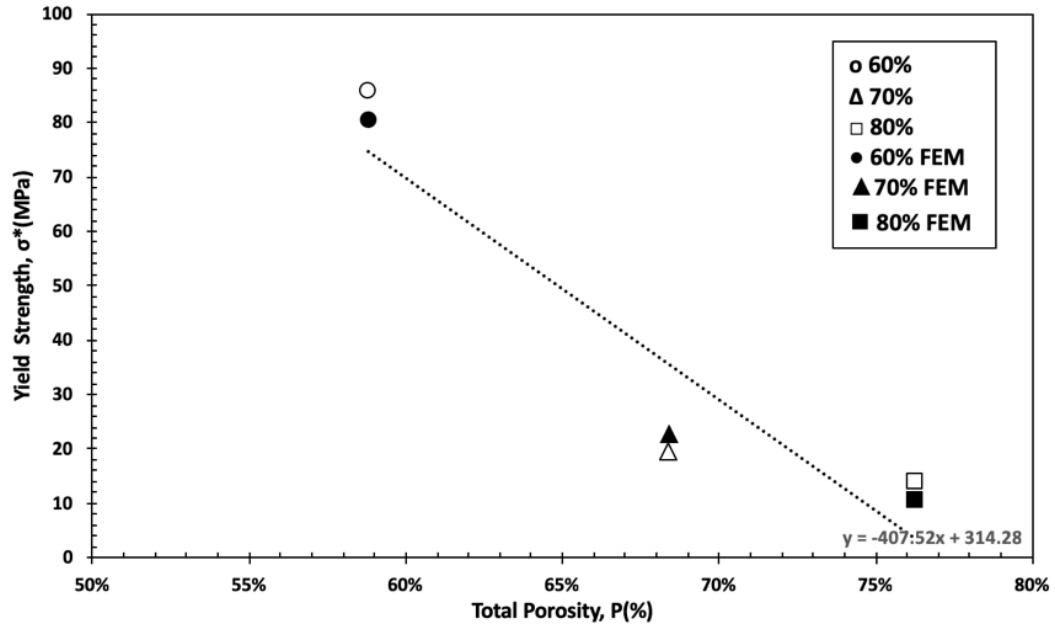
Figure 4.39 Yield Strength of porous titanium samples vs FEM Models with porosities: a) 60%; (b) 70%; (c)80%.

Figure 4.40 demonstrates the data of the experimental elastic modulus and the FEM elastic modulus. The experimental tests indicated elastic moduli of 3930.56 MPa (60% porosity), 2754.36 MPa (70% porosity) and 1455.10 MPa (80% porosity), while the FEM model predicted corresponding elastic modulus values of 3763.27 MPa, 2866.68 MPa and 1307.16 MPa, respectively. Therefore, as was found when investigating yield strength, a lower value of elastic modulus was found by the FEM model than the experimental value in the case of the 70% porous samples. The errors in the FEM model compared to experimental data were 4.445%, 4.07% and 10.67% for the 60%, 70% and 80% porous samples respectively.
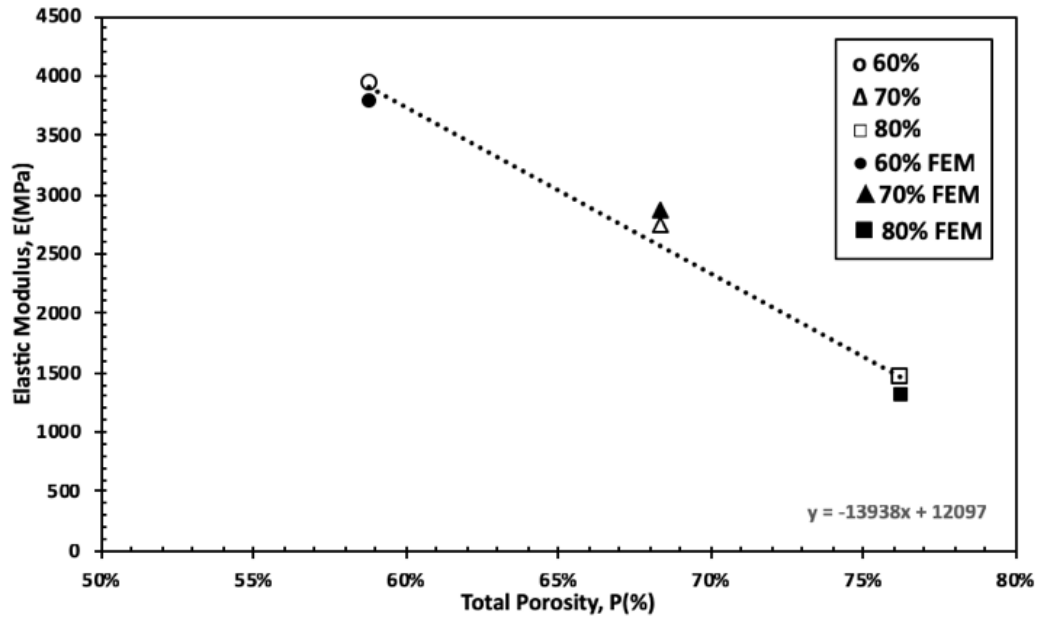
Figure 4.40 Elastic modulus of porous titanium samples vs FEM Models with porosities: a)60%; (b) 70%; (c)80%.

For samples of 80% porosity, maximum error levels were observed for both yield strength and elastic modulus measurements. This demonstrates that an improved pore structure is required in future studies. Furthermore, the 60% porous titanium foam exhibited significantly higher yield strength and elastic modulus compared to samples with 70% or 80% porosity. Therefore, it is evident that porosity strongly affects the yield strength and elastic modulus of titanium foam.

4.6.3 Comparison

The overall compression tests provided average load readings and a sample cross-sectional area from which compressive stress, displacement and initial sample height were calculated, ultimately producing the strain value. The stress-strain curve obtained is displayed in Fig 4.41.
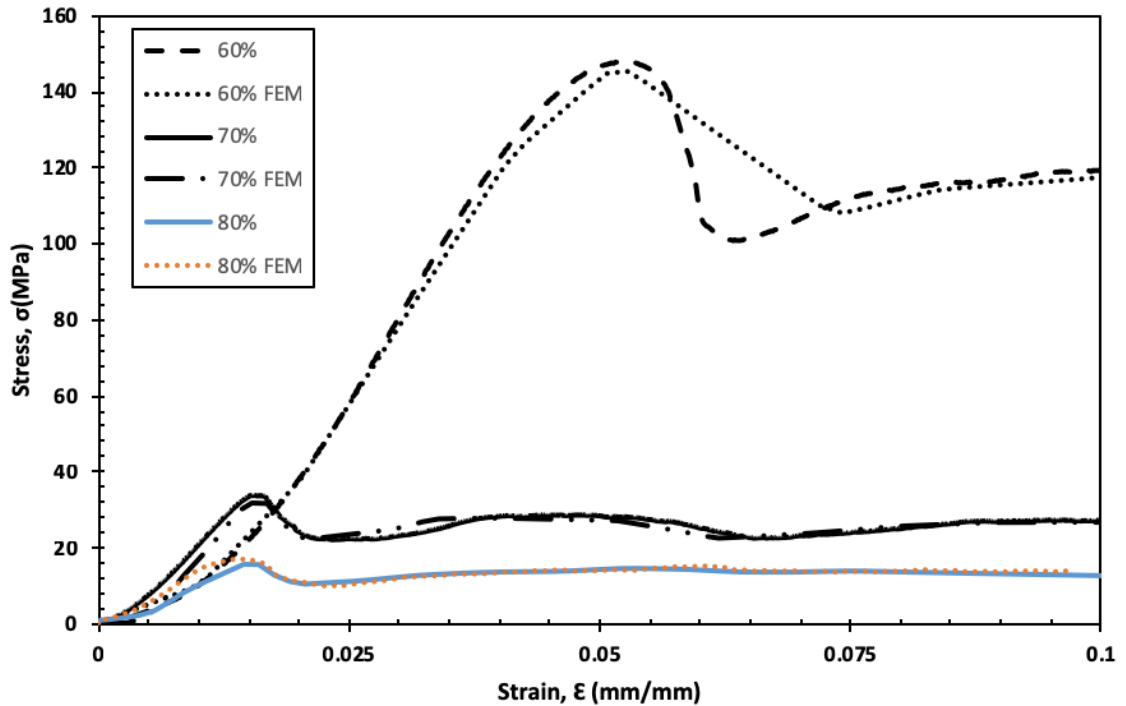
Figure 4.41 Stress-Strain of porous titanium samples vs FEM Models with porosities: 60%; 70%; 80%.

The stress-strain curve displays the orthodox effect of compression on porous metals. The first linear section illustrates the elastic deformation of the structure up to a strain of 0.02. After this, there is a region of plateau, indicating strut collapse and densification processes. The elastic modulus calculated based on this curve was 3.9-1.3 GPa, which corresponds with the range of stiffness of human trabecular bone (1 – 10 GPa) [21]. The yield strength was between 85.75-10.63 MPa, which was taken as the stress at the intersection of the linear regression lines corresponding to the elastic and the plateau regions. The stress-strain curve obtained from the static compression test is shown in the same figure for comparison.

This study has used both experimental and computational modelling to evaluate the mechanical properties exhibited by titanium samples under compression loading. A clear representation of the deformation and failure mechanism of the specimens was obtained using the μCT imaging technique along with the compression test. FEA models were produced from this data which demonstrated a more detailed representation of the relationship between the foam's internal microstructure and the implant's mechanical performance during elastic deformation.

107

4.6.4 Compression Tests and mechanical behaviour of the titanium foams

Both experimental and computational modelling has produced stress-strain curves which display the compressive behaviour of porous metal foam; the results of both were consistent with the other. However, the samples displayed significant differences in yield strength, with error rates of up to 23.46%: the yield strength value obtained by test was more than three times greater than the yield strength obtained through the static compression test. However, the yield strength value measured via the static compression test was affected by non-planar surfaces and the contact compliance between the test sample and the two metal compression plates. As a result of these interactions, the titanium foam exhibited non-linear behaviour prior to yield strength was reached on the stress-strain curve. This suggests that the initial compression stage involved a degree of inelastic phenomena [86]. Alternatively, there may have been alterations in the strut alterations during the process, which would have affected the observable yield strengths at moderate strain levels.

The FEA model produced a more similar match to the compression test results for elastic modulus than the static compression test. Nonetheless, the experimental study demonstrated that the elastic modulus of the titanium foams was almost 1.025 times higher than the value obtained through FEM modelling. This difference may be due to the torque in the strain-locking procedure when the compression load was applied manually via turning the screw at the top of the compression rig. During this process, the sample slipped on the platform and its spatial position became rotated. This would have affected the similarity between the FEA model and the experiment due to variations in the FE boundary conditions in the experimental process [99]. Therefore, the parallel plate compression test will need to be altered to correct the error resulting from the contact boundary behaviour. This may be achieved by attaching the sample to the end-caps of the compression rig such that the bottom surface will no longer cause the sample to slip.

To test consistency with existing literature, the current study investigated the mechanical properties of the same regular and 30% randomised structures. It found that both the Young's moduli, and the yield strengths were higher than the predicted values by FEA models (3.5 – 6.5 GPa and 49 MPa for the regular and 56 MPa for the randomised respectively) [83, 90]. Aside from the limitations of the mechanical tests as discussed above, there are further drawbacks which may have resulted in inaccuracies in the FEA model, as will be noted below.

In conclusion, this study has found that the elastic modulus of the titanium samples tested are within the range of human trabecular bone (1 – 10 GPa). Furthermore, the samples displayed an appropriate yield strength for orthopaedic applications (~ 40 MPa) [66]. Therefore, the samples tested are likely to be appropriate for biomedical implants.

4.6.5   Limitations of the Titanium Foam FEA model

FEA simulation are useful to avoid both the machine contact compliance issue linked to the static compression test and the difficulty associated with reaching low strain deformation in the stepwise compression test. Thus, the FEA simulation can be used to obtain a linear elastic behaviour of foam at a low level of strain. While the FEA model produced yield strength and elastic modulus values which were most consistent with those in existing literature, the method does have a number of limitations which can be resolved for more accurate results.

Firstly, the accuracy of the FEA model was heavily impacted by the original resolution of the μCT images [86]. The resolution was set at 15 μm per voxel as a result of the limited field of view in the μCT, meaning that the images did not accurately capture the appearance of the fine micropores and internal surface roughness. Furthermore, the low resolution also impacted the accuracy of the images of the strut surfaces. Moreover, the μCT images were resampled to 30 μm to promote computational efficiency. This can therefore result in inaccuracy when predicting material strength because of the altered strut properties captured; rough strut surfaces may have been smoothed, altering the apparent thickness of the struts. The effect of this was contingent on adjacent voxels. Accuracy was also affected by the threshold value selected for imaging processing: it has been reported that a variation of 0.5% in threshold resulted a difference of 9% in stiffness of the trabecular bone (porosity > 85%) and 3% when porosity is less than 80% [89]. Accuracy of estimations of mechanical properties can therefore be heightened by selecting the optimum threshold. Therefore, where images are of low resolution, the optimal method is advance thresholding instead of plain thresholding.

A second limitation relates to the mesh quality of the FEA model in determining accuracy [64]. The impact of the element size on accuracy of the FEA model has been researched by a number of academics previously [60, 61, 62] and it has been found that in addition to mesh resolution, the accuracy of the FEA model is affected by the selected element type. Thus, where images have low resolution, linear elements or reduced integration methods resulted

in inaccurate predictions of the stress distribution. This can be attributed to both stiffening errors and the severe smoothing effect. Therefore, low resolution models are better benefited by the use of quadratic elements when conducting stress field estimation. However, if this element is chosen, significant cost implications will ensue.

4.7　Mechanical response of the dental implant

3D solid continuum elements were used to produce a finite element mesh. Compression tests were conducted on this porous dental titanium implant using LS-DYNA software. Figure 4.42 demonstrates the distributions and levels of stress experienced throughout the implant and surrounding bones. The stress was distributed unevenly across the implants, with the greatest concentration of stresses at the neck regions of the implants.

The stress measured in the titanium foam implants was less than that recorded in the cortical bone. The stress around the implant necks was typically lower than the surrounding bone where there was 60% porosity compared to 70% and 80% porosity samples. This implies that titanium implants with 60% porosity transfer less load to surrounding bones than the other samples; where the porosity was 80%, the titanium foam spread more stress to the surrounding bones. This therefore suggests that titanium foam implants can be used as a solution for the stress shielding problem. However, more research would need to be conducted on this possibility as the present study has not considered the shape of the implant and the consequential complicated interlacing patterns required.
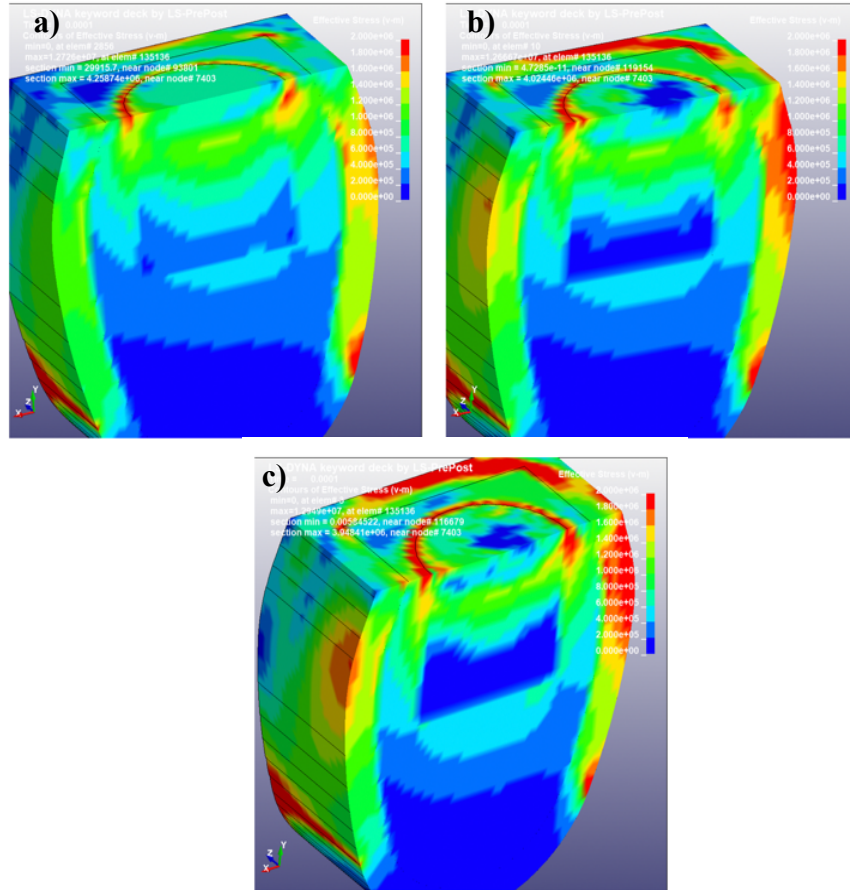
Figure 4.42 Distribution of von-mises stresses of porous titanium samples within the dental implant with porosities of: (a) 60%; (b) 70%; (c) 80%.

4.7.1 Evaluation of the Results

Figs 4.43 and 4.44 demonstrate the distributions of mesh sizes in the implants. Shear stress values corresponding to all the interfacial cells are counted and normalised by the total volume. It was found that foams with 80% porosity displayed more local cells with greater shear stress. In contrast, in 60% porosity samples, the shear stress values shifted from 4.16 to 10.25 MPa during the early stage and 18.19 to 20.56 MPa at the final stage. These shifts are larger than those typically seen. The concentration of shear stress in the distributions were measured using skewness. It was found that higher shear stresses in 70% and 80% porous foams caused modest alterations from almost symmetric to slightly positively skewed distributions. In the 80% porosity foams, as length of time increased, the shear distribution became more significantly skewed towards the higher stress region. This shows that high shear stress concentrations can result from the presence of a higher number of pores, which is the case in higher porosity samples.
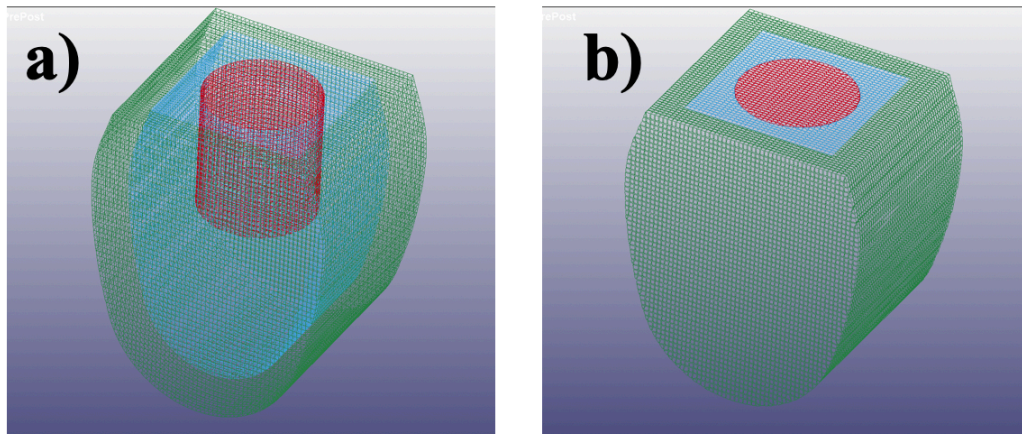
Figure 4.43 3D mesh patterns of the FEM Titanium foam dental implant showing the overall meshing throughout the tooth and the implant.
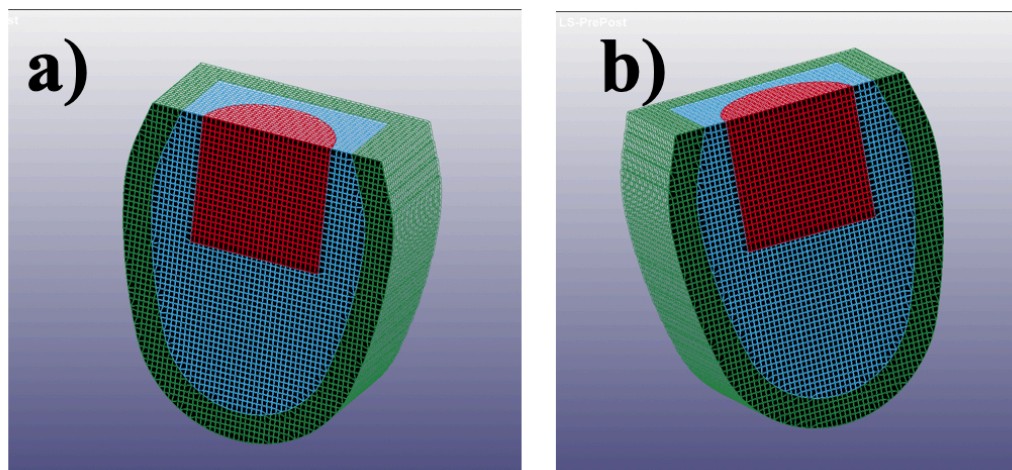
Figure 4.44 3D cross-sectional mesh patterns of the FEM Titanium foam dental implant showing the overall meshing throughout the tooth and the implant.

Both the 70% and 80% porosity samples exhibited stress values lower than 18 MPa. However, through examination of the shear distributions at the boundary between the tooth and the implant, factors may have been considered which would have inhibited the stress shielding effects of the implant.

After evaluation of the shear stress values of the 60%, 70% and 80% porosity samples, it seems that at shear stresses above 18 MPa, the 80% porosity foam is more effective in stress shielding.

4.7.1.1 Influence of the Strut Architecture on Mechanical Properties

While the compression test produced an image for strut deformation, it was difficult to obtain either the visualisation of the initial elastic behaviour at low strain levels or the stress concentration in the structure. On the other hand, the FEA model could predict both the mechanical properties of the implant and the initial elastic deformation and localised internal stress distribution.

The structure produced demonstrated that there was elastic deformation up until a strain of 1%, after which local plasticity changes occur. The implant modelled with 60% porosity was subjected to a greater load during compression, and the struts in the implant broke faster in the bottom randomised section. These effects agreed with the homogenous model proposed by Gibson and Ashby whereby the first pore collapse typically causes adjacent pores to collapse consistent with the loading direction. Therefore, the local plasticity deformation was observed to develop layer by layer towards the compression direction. Furthermore, there were lower concentrations of stress present in the regular struts internal to the U-shaped model where it appears that the tooth behaves as a load-bearing structure. This functions to retain the overall structure of the implant subject to loading.

Use of FEA modelling of the foams were useful in providing clearer comparisons of the stress distributions in different implant models. While the foam model exhibited more evenly distributed stress, the dental implant model exhibited a more localised distribution. The regular foam more easily facilitated the axial transformation of load as a result of the orientation design which causes failure in the whole cross section, differing from the randomised structure. When examining the dental implant model, it was found that random initiation of strut failure resulted in areas of high stress concentration. The load was propagated locally in both the tooth and the implant, leading to isolated strut collapses instead of comprehensive collapse of the load bearing features in the regular structure.

4.7.1.2 Local Shear Stress Distribution

80% porosity foams experienced a much broader range of shear stress. In contrast, there was a regular pattern with comparatively high local stress concentrations present in the boundaries between the tooth and the implant in 60% porosity samples, but low shear stress in the surrounding bone. While the implant structure benefits from stress shielding, the entire structure does not.

Examination of shear stress histograms at different time stamps reveals that in the 70% porosity foam, there was a more significant variation in shear stress distribution compared to both the 60% and 80% porosity foams, particularly at later time points. Where compression was lower, there was a increasing mode of the shear stress increased by 200% in conjunction with length of time during early stage of compression in 70% porosity foams. On the other hand, at higher compression rates, 60% porosity foams exhibited almost a 200% increase in the mode of shear stress. As greater compression was applied, the implant structure was found to exhibit more high stress regions.

It was observed that there was a positive correlation between shear stress in surrounding bone and porosity, suggesting that uniquely designed implants may need to be based on different internal structures. For instance, at the initial implantation stages, the desired implant model must be based on a 3D template with appropriate porosity. As the process progresses, a more uniformly distributed shear with a stable average magnitude may be needed.

4.7.1.3 Limitations of the Dental Implant Model

This study has used a dental implant model based on shear stress. However, this feature can be amended in the model as more data comes to light relating to factors such as porosity level and mechanical shear. Furthermore, to investigate the relationship between shear stress and porosity more carefully, different modelling techniques may need to be applied to mitigate the effects of possible artefacts in compression behaviour of models.

Future studies could also use statistical analysis on various samples of the same porosity to heighten the accuracy of the model. Such analysis could also be used on samples formed from different materials including apatite foams and bioglass foams.

A lack of quantitative experimental validation data for these dependencies also limited this investigation. Currently, the average shear stress values provided by macroscopic computational modelling results are the only values available for comparison.

In conclusion, the present study has conducted a microscopic evaluation of shear stress experienced within dental implant structures. As a result, quantitative data has been produced recording the relationship between porosity and shear stress distribution. Simulation of compression in dental implants consisting of varying internal structures has

discovered possible guidelines to be exercised when producing implants in the future which aim to mimic bone ingrowth.

4.8   Discussion of the FEA Models

In this study, the space holder method was employed to formulate porous titanium foams for use as biomedical applications in dentistry as teeth implants which simulate bone. It was found that the Ti foam with 60% porosity demonstrated similar compressive characteristics, elastic modulus and yield strength to cortical bone, while the 80% porous foam was wholly incompatible with the mechanical properties of cancellous bone. The structure of the titanium foams consisted partly of macropores resulting from space holder particles and micropores resulting from voids in the titanium powder. Only the macropores were visible through micro-CT imaging. Although a higher resolution micro-CT imaging could capture the micropores, this would limit the specimen size used.

Data obtained from FEM models were compared with experimental data to examine the mechanical performance of the specimens when subjected to uniaxial compression. The results were very pleasing, demonstrating surgically beneficial effects. These can be obtained using a 3D model reconstructed from micro-CT. However, there were some inaccuracies in the FEM models due to the inconsistency of distribution of pores of varying sizes and shapes in the actual samples which were not translated into the FEM model which assumed a uniform spherical shape of pores. This explains why the relevant mechanical properties, elastic modulus and yield strength, predicted by the FEM model were consistently lower for samples with 70% porosity relative to those with 60% and 80% porosity. Regardless of this, FEM modelling is still a useful tool in accurately reconstructing representative porous metal structures.

Another difficulty encountered when modelling Ti foam characteristics was the bimodal pore size distribution in the samples. While the FEM simulations captured the macropores in the structures, the micropores were not identified. Therefore, the greatest degree of agreement with the results of experimental uniaxial compression would only be attainable by combining CT imaging with FEM simulations based on the bimodal matrix properties.

5. CONCLUSIONS

This thesis has examined the morphology and mechanical properties of porous titanium foams to determine the appropriateness of their use as biomedical implants. There was an emphasis on finite element analysis to determine their suitability through the use of theoretical models, finite element simulations and experimental investigations regarding the morphological and mechanical characteristics of the titanium foams. All investigations conducted complied with ASTM standards. The data were then analysed to determine the micro and macro structural behaviour of the metal foams.

The titanium foam samples produced for this study had porosities within the range 55.95 and 77.94%. These samples were found to contain two types of pores: macropores and micropores. The former was created due to the evaporation of magnesium particles acting as space holders in the process; the latter were generated in cell walls as a result of insufficient sintering. In samples with higher porosity, both the macropores and the micropores caused an interconnected network of pores to arise, while such a network was formed only of micropores in low porosity foams.

All the samples demonstrated a standard compression stress-strain curve typical of elastic-plastic foams displaying three key stages of deformation: an initial period of linear elasticity, a long plateau stage, and a densification stage. During the densification stage, the flow stress was observed to increase rapidly.

When the foams were subjected to compression loads, the concentration of stress within the porous structures resulted in early yielding at a number of areas, causing smaller than expected slopes in the elastic region. Therefore, the unloading modulus was chosen to be used, which is measured after a plastic strain of 0.2%.

The measured elastic moduli of the 68.3% and 76.3% porosity foams were close similar to the elastic modulus of human bone: the elastic moduli of those foams were observed to be 1.08 – 3.93 GPa while that of bone is 1-30 GPa. The alignment of the mechanical properties of the foams and cancellous and cortical bone indicates that the titanium foams would be effective as stress shielding features.

The samples were submerged in SBF for 14, 21, 28 days, following which it was observed that the surfaces of the samples became supersaturated with calcium elements. Surface

processing was conducted on the foam samples, enhancing their bioactivity as the surfaces exposed to sodium titanate formed apatite formations. These were then more effective than untreated surfaces: after 21 days, the surfaces of treated foams with 80% porosity exhibited the production of a flower-like hydroxyapatite phase whereas untreated surfaces facilitated the precipitation of Ca-P rich particles other than hydroxyapatite.

In this research, three computational models of titanium at 60%, 70% and 80% porosity were generated using X-ray microtomography (μCT) imaging based on the actual models produced by the space holder method. This was done to better visualise the mechanical properties of the specimens, aiding understanding of how the implant would behave before submitting the design to manufacture. This allowed for analysis of the impact of discrete design factors on overall performance during the design process.

The model was applied to foams of 60%, 70% and 80% porosities. The values obtained by the FEA simulation relation to both strength and elastic modulus was consistent with the experimental values and the values in existing literature. This suggests that this computational method is appropriate for analysing the properties of highly porous materials such as the titanium foams in this study, for orthopaedic implants.

The measured elastic moduli of the 60%, 70% and 80% porous titanium foams were found to be 3930.56, 2754.36, and 1455.10 MPa, respectively. These are almost optimal values for dental implants. However, in contrast to this, the FEM simulation produced values of a lower yield strength and elastic modulus in relation to the 70% porous foam, and higher values for the 60% and 80% porosity samples.

The FEM modelling result most consistent with experimental results was measured for the 70% porous sample, as the nature of the micropores in the structure were considered. These affect the elastic and plastic matrix properties of the substance.

A titanium foam dental implant model with calibrated parameters was then used to mimic the dental implant system. This model aided the analysis of surgical applications of the titanium foam implants. The stress measured in the 80% porosity titanium foam implant was found to be less than that measured in the 60% and 70% porosity samples.

Therefore, as the 80% porous foam experienced less stress, the surrounding bone needed to bear greater stress. This suggests that a greater load was transferred to the surrounding bone

around the 80% porous titanium foam implant. This may indicate a potential solution for the existing stress shielding issue.

Ultimately, there was a high level of consistency between the experimental results and the results obtained from the simulation compression tests. Therefore, the proposed model is an accurate indicator of the performance of a bioimplant system founded from titanium foam.

Thus, the space holder powder metallurgy technique was used in conjunction with a magnesium powder space holder, resulting in biomimetic titanium scaffolds with a selected range of porosities (60%, 70% and 80%).

Each porous scaffold showed a significant amount of pore interconnectivity, which is thought to be favourable for both osseointegration and ingrowth of bone tissue. According to figures obtained by previous studies, the average range of pore sizes in the manufactured samples were optimal for promoting osseointegration [12, 13]. The pore size was determined by porosity analysis.

Furthermore, the 60% and 80% porosity foams exhibited similar compressive strength values and elastic moduli to those of human cortical and cancellous bone. Therefore, analysis of the structural and mechanical characteristics of the titanium samples suggests that the current approach may be beneficial in manufacturing implants needed for bone tissue engineering in the future.

FEA modelling was then used to quantify the mechanical properties of the different titanium porous implant structures. By uniting the different mechanical and performative factors of the implant, it is suggested that a combination of regular and randomised structures would be best suited for an implant design. The design ought to be contingent on factors such as the shape of the affected area, as materials with a more randomised structure are likely to be more effective for stress bearing positions. If this is the case, the some regularly structured material could also be used in conjunction with additional strut roughness to promote early stage bone ingrowth to connect the implant to the site.

REFERENCES

[1] J.L. Krevolin, J. Silverstein, A, Liu, Characterization of a Novel Porous Titanium Scaffold for Orthopedic Applications, ORS 2012 Annu. Meet. 6 (**2012**) 2670.

[2] G. Ryan, A. Pandit, D.P. Apatsidis, Fabrication methods of porous metals for use in orthopaedic applications, Biomaterials. 27 (**2006**) 2651–2670.

[3] P. Siegkas, N. Petrinic, V.L. Tagarielli, Measurements and micro-mechanical modelling of the response of sintered titanium foams, J. Mech. Behav. Biomed. Mater. 57 (**2016**) 365–375.

[4] C.E. Wen, Y. Yamada, A. Nouri, P. Hodgson, Porous Titanium with Porosity Gradients for Biomedical Applications, Mater. Sci. Forum. 539–543 (**2007**) 720–725.

[5] X. Zhang, W. Guo, J. Qiu, S. Wang, X. Yu, L. Li, H. Liu, Nanostructured titanium foam with metal ions incorporation for promoting osteogenic differentiation of mesenchymal stem cells, J. Alloys Compd. 729 (**2017**) 816–822.

[6] F. Zhang, E. Otterstein, E. Burkel, Spark plasma sintering, microstructures, and mechanical properties of macroporous titanium foams, Adv. Eng. Mater. 12 (**2010**) 863–872.

[7] J. Jakubowicz, G. Adamek, M. Dewidar, Titanium foam made with saccharose as a space holder, J. Porous Mater. 20 (**2013**) 1137–1141.

[8] A. Nouri, P. D., C. We, Biomimetic Porous Titanium Scaffolds for Orthopedic and Dental Applications, Biomimetics Learn. from Nat. (**2010**) 415–451.

[9] S. Kashef, S.A. Asgari, P. Hodgson, W.Y. Yan, Simulation of Three-Point Bending Test of Titanium Foam for Biomedical Applications, Adv. Mater. Res. 32 (**2008**) 237–240.

[10] J.Y. Xiong, Y.C. Li, X.J. Wang, P.D. Hodgson, C.E. Wen, Titanium-nickel shape memory alloy foams for bone tissue engineering, J. Mech. Behav. Biomed. Mater. 1 (**2008**) 269–273.

[11] A.H. Yusop, A.A. Bakir, N.A. Shaharom, M.R. Abdul Kadir, H. Hermawan, Porous biodegradable metals for hard tissue scaffolds: A review, Int. J. Biomater. 2012 (**2012**).

[12] J.P. Li, J.R. De Wijn, C.A. Van Blitterswijk, K. De Groot, The effect of scaffold architecture on properties of direct 3D fiber deposition of porous Ti_6Al_4V for orthopedic implants, J. Biomed. Mater. Res. - Part A. 92 (**2010**) 33–42.

[13] Y. Chen, J.E. Frith, A. Dehghan-Manshadi, H. Attar, D. Kent, N.D.M. Soro, M.J. Bermingham, M.S. Dargusch, Mechanical properties and biocompatibility of porous

titanium scaffolds for bone tissue engineering, J. Mech. Behav. Biomed. Mater. 75 (**2017**) 169–174.

[14]   R. Singh, P.D. Lee, J.R. Jones, G. Poologasundarampillai, T. Post, T.C. Lindley, R.J. Dashwood, Hierarchically structured titanium foams for tissue scaffold applications, Acta Biomater. 6 (**2010**) 4596–4604.

[15]   Z. Esen, E. Tarhan Bor, Ş. Bor, Characterization of loose powder sintered porous titanium and Ti_6Al_4V alloy, Turkish J. Eng. Environ. Sci. 33 (**2009**) 207–219.

[16]   Z. Wally, W. van Grunsven, F. Claeyssens, R. Goodall, G. Reilly, Porous Titanium for Dental Implant Applications, Metals (Basel). 5 (**2015**) 1902–1920.

[17]   C.E.C. Wen, Y. Yamada, K. Shimojima, Y. Chino, H. Hosokawa, M. Mabuchi, Novel titanium foam for bone tissue engineering, J. Mater. Res. 17 (**2002**) 2633–2639.

[18]   D.C. Dunand, Processing of titanium foams, Adv. Eng. Mater. 6 (**2004**) 369–376.

[19]   H.-D. Jung, H. Lee, H.-E. Kim, Y.-H. Koh, J. Song, Fabrication of Mechanically Tunable and Bioactive Metal Scaffolds for Biomedical Applications, J. Vis. Exp. (**2015**) 1–11.

[20]   O. Smorygo, A. Marukovich, V. Mikutski, A.A. Gokhale, G.J. Reddy, J.V. Kumar, High-porosity titanium foams by powder coated space holder compaction method, Mater. Lett. 83 (**2012**) 17–19.

[21]   Y. Zhao, L.E. Monaghan, A novel manufacturing method for titanium foam for biomedical applications, 2008 World Congr. Powder Metall. Part. Mater. PowderMet 2008, June 8, 2008 - June 12, 2008. (**2008**) 9340–9348.

[22]   M. Bram, C. Stiller, H.P. Buchkremer, D. Stöver, H. Baur, High-porosity titanium, stainless steel, and superalloy parts, Adv. Eng. Mater. 2 (**2000**) 196–199.

[23]   M. Barrabés, P. Sevilla, J.A. Planell, F.J. Gil, Mechanical properties of nickel-titanium foams for reconstructive orthopaedics, Mater. Sci. Eng. C. 28 (**2008**) 23–27.

[24]   J. Rivard, V. Brailovski, S. Dubinskiy, S. Prokoshkin, Fabrication, morphology and mechanical properties of Ti and metastable Ti-based alloy foams for biomedical applications, Mater. Sci. Eng. C. 45 (**2014**) 421–433.

[25]   A. Kennedy, Porous Metals and Metal Foams Made from Powders, Powder Metall. (**2012**).

[26]   M. Sharma, G.K. Gupta, O.P. Modi, B.K. Prasad, A.K. Gupta, Titanium foam through powder metallurgy route using acicular urea particles as space holder, Mater. Lett. 65 (**2011**) 3199–3201.

[27] M. Tange, A. Manonukul, P. Srikudvien, The effects of organic template and thickening agent on structure and mechanical properties of titanium foam fabricated by replica impregnation method, Mater. Sci. Eng. A. 641 (**2015**) 54–61.

[28] T. Matsushita, S. Fujibayashi, T. Kokubo, Titanium foam for bone tissue engineering, Met. Foam Bone Process. Modif. Charact. Prop. 17 (**2016**) 111–130.

[29] F. García-Moreno, Commercial applications of metal foams: Their properties and production, Materials (Basel). 9 (**2016**) 20–24.

[30] M. Yazdimamaghani, M. Razavi, D. Vashaee, K. Moharamzadeh, A.R. Boccaccini, L. Tayebi, Porous magnesium-based scaffolds for tissue engineering, Mater. Sci. Eng. C. 71 (**2017**) 1253–1266.

[31] S. Kashef, A. Asgari, T.B. Hilditch, W. Yan, V.K. Goel, P.D. Hodgson, Fatigue crack growth behavior of titanium foams for medical applications, Mater. Sci. Eng. A. 528 (**2011**) 1602–1607.

[32] Y. Chino, D.C. Dunand, Directionally freeze-cast titanium foam with aligned, elongated pores, Acta Mater. 56 (**2008**) 105–113.

[33] C. Zou, E. Zhang, M. Li, S. Zeng, Preparation, microstructure and mechanical properties of porous titanium sintered by Ti fibres, J. Mater. Sci. Mater. Med. 19 (**2008**) 401–405.

[34] U. Müller, T. Imwinkelried, M. Horst, M. Sievers, U. Graf-Hausner, Do human osteoblasts grow into open-porous titanium, Eur. Cells Mater. 11 (**2006**) 8–15.

[35] T. Imwinkelried, Mechanical properties of open-pore titanium foam, J. Biomed. Mater. Res. - Part A. 81 (**2007**) 964–970.

[36] A. Manonukul, P. Srikudvien, M. Tange, Microstructure and mechanical properties of commercially pure titanium foam with varied cell size fabricated by replica impregnation method, Mater. Sci. Eng. A. 650 (**2016**) 432–437.

[37] S. Kashef, A. Asgari, T.B. Hilditch, W. Yan, V.K. Goel, P.D. Hodgson, Fracture toughness of titanium foams for medical applications, Mater. Sci. Eng. A. 527 (**2010**) 7689–7693.

[38] N. Jha, D.P. Mondal, J. Dutta Majumdar, A. Badkul, A.K. Jha, A.K. Khare, Highly porous open cell Ti-foam using NaCl as temporary space holder through powder metallurgy route, Mater. Des. 47 (**2013**) 810–819.

[39] X.H. Wang, J.S. Li, R. Hu, H.C. Kou, Mechanical properties and pore structure deformation behaviour of biomedical porous titanium, Trans. Nonferrous Met. Soc. China (English Ed. 25 (**2015**) 1543–1550.

[40] J.C. Li, D.C. Dunand, Mechanical properties of directionally freeze-cast titanium foams, Acta Mater. 59 (**2011**) 146–158.

[41] M.V. de Oliveira, A.C. Moreira, C.R. Appoloni, R.T. Lopes, L.C. Pereira, C.A.A. Cairo, Porosity Study of Sintered Titanium Foams, Mater. Sci. Forum. 530–531 (**2006**) 22–28.

[42] A. Bansiddhi, D.C. Dunand, Titanium and NiTi foams for bone replacement, Woodhead Publishing Limited, **2014**.

[43] G.E. Ryan, A.S. Pandit, D.P. Apatsidis, Porous titanium scaffolds fabricated using a rapid prototyping and powder metallurgy technique, Biomaterials. 29 (**2008**) 3625–35.

[44] Y.J. Chen, B. Feng, Y.P. Zhu, J. Weng, J.X. Wang, X. Lu, Fabrication of porous titanium implants with biomechanical compatibility, Mater. Lett. 63 (**2009**) 2659–2661.

[45] E.D. Spoerke, N.G. Murray, H. Li, L.C. Brinson, D.C. Dunand, S.I. Stupp, A bioactive titanium foam scaffold for bone repair, Acta Biomater. 1 (**2005**) 523–533.

[46] W. Tanwongwan, J. Carmai, Finite Element Modelling of Titanium Foam Behaviour for Dental Application, Engineering. III (**2011**) 4–9.

[47] J. Xiao, Y. Yang, G.B. Qiu, Y.L. Liao, H. Cui, X.W. Lü, Volume change of macropores of titanium foams during sintering, Trans. Nonferrous Met. Soc. China (English Ed. 25 (**2015**) 3834–3839.

[48] B. Notarberardino, Image Based Finite Element Modelling for the Mechanical Characterisation of Complex Material Systems, Sch. Eng. (**2010**).

[49] H. Zarkoob, S. Ziaei-Rad, M. Fathi, H. Dadkhah, An investigation on mechanical behavior of barium titanate foam with hydroxyapatite coating, Ceram. Int. 38 (**2012**) 3445–3451.

[50] R. Singh, P.D. Lee, R.J. Dashwood, T.C. Lindley, Titanium foams for biomedical applications: a review, Mater. Technol. 25 (**2010**) 127–136.

[51] M. Dewidar, Mechanical and Microstructure Properies of High Porosity Sintered Ti-6Al- 4V Powder for Biomedical Applications, J. Eng. Sci. 34 (**2006**) 1929–1940.

[52] T.D. Sargeant, M.O. Guler, S.M. Oppenheimer, A. Mata, R.L. Satcher, D.C. Dunand, S.I. Stupp, Hybrid bone implants: Self-assembly of peptide amphiphile nanofibers within porous titanium, Biomaterials. 29 (**2008**) 161–171.

[53] Y. Chino, H. Hosokawa, C. Wen, Y. Yamada, M. Mabuchi, K. Shimojima, Compressive Deformation Characteristics of Open-Cell Mg Alloys with Controlled Cell Structure, Mater. Trans. 43 (**2005**) 1298–1305.

[54] M. Ghidelli, M. Sebastiani, K.E. Johanns, G.M. Pharr, Effects of indenter angle on micro-scale fracture toughness measurement by pillar splitting, J. Am. Ceram. Soc. 100 (**2017**) 5731–5738.

[55] W.-J. Seong, U.-K. Kim, J.Q. Swift, Y.-C. Heo, J.S. Hodges, C.-C. Ko, Elastic properties and apparent density of human edentulous maxilla and mandible., Int. J. Oral Maxillofac. Surg. 38 (**2009**) 1088–93.

[56] T. Kokubo, S. Yamaguchi, Novel Bioactive Titanate Layers Formed on Ti Metal and Its Alloys by Chemical Treatments, Materials (Basel). 3 (**2009**) 48–63.

[57] J.P. Li, S.H. Li, K. de Groot, P. Layrolle, Preparation and Characterization of Porous Titanium, Key Eng. Mater. 218–220 (**2001**) 51–54.

[58] C. Pappalettere, Computational Modelling of Biomechanics and Biotribology in the Musculoskeletal System, Comput. Model. Biomech. Biotribology Musculoskelet. Syst. Biomater. Tissues. (**2014**) 485–511.

[59] A. Roychowdhury, Application of the Finite Element Method in Orthopedic Implant Design, J. Long. Term. Eff. Med. Implants. 19 (**2009**) 55–82.

[60] R. Huiskes, A Survey of Finite Element Analysis in Orthopedic Biomechanics : The First Decade, J. Biomech. 16 (**1983**) 385–409.

[61] B. Chang, W. Song, T. Han, J. Yan, F. Li, L. Zhao, H. Kou, Y. Zhang, Influence of pore size of porous titanium fabricated by vacuum diffusion bonding of titanium meshes on cell penetration and bone ingrowth, Acta Biomater. 33 (**2016**) 311–321.

[62] D. Hara, Y. Nakashima, T. Sato, M. Hirata, M. Kanazawa, Y. Kohno, K. Yoshimoto, Y. Yoshihara, A. Nakamura, Y. Nakao, Y. Iwamoto, Bone bonding strength of diamond-structured porous titanium-alloy implants manufactured using the electron beam-melting technique, Mater. Sci. Eng. C. 59 (**2016**) 1047–1052.

[63] L. Tuchinskiy, Novel fabrication technology for metal foams (Tuchinskiy).pdf, J. Adv. Mater. (**2005**).

[64] V.S. Cheong, P. Fromme, A. Mumith, M.J. Coathup, G.W. Blunn, Novel adaptive finite element algorithms to predict bone ingrowth in additive manufactured porous implants, J. Mech. Behav. Biomed. Mater. 87 (**2018**) 230–239.

[65] S. Thelen, F. Barthelat, L.C. Brinson, Mechanics considerations for microporous titanium as an orthopedic implant material, J. Biomed. Mater. Res. - Part A. 69 (**2004**) 601–610.

[66] B. Dabrowski, W. Swieszkowski, D. Godlinski, K.J. Kurzydlowski, Highly porous titanium scaffolds for orthopaedic applications, J. Biomed. Mater. Res. - Part B Appl. Biomater. 95 (**2010**) 53–61.

[67] X. Guangsheng, K. Hongchao, L. Xianghong, L. Fuping, L. Jinshan, Z. Lian, Microstructure and Mechanical Properties of Porous Titanium Based on Controlling Young's Modulus, Rare Met. Mater. Eng. 46 (**2017**) 2041–2048.

[68]   Y. Xiong, C. Qian, J. Sun, Fabrication of porous titanium implants by three-dimensional printing and sintering at different temperatures, Dent. Mater. J. 31 (**2012**) 815–820.

[69]   X. Fan, B. Feng, J. Weng, J. Wang, X. Lu, Processing and properties of porous titanium with high porosity coated by bioactive titania nanotubes, Mater. Lett. 65 (**2011**) 2899–2901.

[70]   L. Wang, P. Liu, L. Wang, W. Xing, Y. Fan, N. Xu, Preparation conditions and porosity of porous titanium sintered under positive pressure, Mater. Manuf. Process. 28 (**2013**) 1166–1170.

[71]   F. Li, J. Li, G. Xu, G. Liu, H. Kou, L. Zhou, Fabrication, pore structure and compressive behavior of anisotropic porous titanium for human trabecular bone implant applications, J. Mech. Behav. Biomed. Mater. 46 (**2015**) 104–114.

[72]   M. Khodaei, M. Fathi, M. Meratian, O. Savabi, The effect of porosity on the mechanical properties of porous titanium scaffolds: Comparative study on experimental and analytical values, Mater. Res. Express. 5 (**2018**).

[73]   T. Shimizu, K. Matsuzaki, Y. Ohara, Process of Porous Titanium Using a Space Holder, J. Japan Soc. Powder Powder Metall. 53 (**2006**) 36–41.

[74]   Y. Chen, D. Kent, M. Bermingham, A. Dehghan-Manshadi, G. Wang, C. Wen, M. Dargusch, Manufacturing of graded titanium scaffolds using a novel space holder technique, Bioact. Mater. 2 (**2017**) 248–252.

[75]   S.K. Parashar, J.K. Sharma, A review on application of finite element modelling in bone biomechanics, Perspect. Sci. 8 (**2016**) 696–698.

[76]   H. Zarkoob, S. Ziaei-Rad, M. Fathi, H. Dadkhah, An investigation on mechanical behavior of barium titanate foam with hydroxyapatite coating, Ceram. Int. 38 (**2012**) 3445–3451.

[77]   H. Do Jung, T.S. Jang, L. Wang, H.E. Kim, Y.H. Koh, J. Song, Novel strategy for mechanically tunable and bioactive metal implants, Biomaterials. 37 (**2015**) 49–61.

[78]   J. Qin, Q. Chen, C. Yang, Y. Huang, Research process on property and application of metal porous materials, J. Alloys Compd. 654 (**2016**) 39–44.

[79]   H. Schiefer, M. Bram, H.P. Buchkremer, D. Stöver, Mechanical examinations on dental implants with porous titanium coating, J. Mater. Sci. Mater. Med. 20 (**2009**) 1763–1770.

[80]   L.M.R. De Vasconcellos, F.N. Oliveira, D. De Oliveira Leite, L.G.O. De Vasconcellos, R.F. Do Prado, C.J. Ramos, M.L. De Alencastro Graça, C.A.A. Cairo, Y.R. Carvalho, Novel production method of porous surface Ti samples for biomedical application, J. Mater. Sci. Mater. Med. 23 (**2012**) 357–364.

[81] J. Luyten, I. Thijs, M. Ravelingien, S. Mullens, Bone engineering with porous ceramics and metals, Adv. Eng. Mater. 13 (**2011**) 1002–1007.

[82] X. Rao, J. Li, X. Feng, C. Chu, Bone-like apatite growth on controllable macroporous titanium scaffolds coated with microporous titania, J. Mech. Behav. Biomed. Mater. 77 (**2018**) 225–233.

[83] I. Mutlu, Sinter-coating method for the production of TiN-coated titanium foam for biomedical implant applications, Surf. Coatings Technol. 232 (**2013**) 396–402.

[84] L.P. Lefebvre, E. Baril, Properties of titanium foams for biomedical applications, Adv. Eng. Mater. 15 (**2013**) 159–165.

[85] F.P. Li, J.S. Li, G.J. Liu, H.C. Kou, G.S. Xu, L. Zhou, Fabrication and Compressive Properties of Porous Ti$_6$Al$_4$V Alloy with Elongated Pores for Biomedical Application, Mater. Sci. Forum. 815 (**2015**) 354–358.

[86] Q. Ran, W. Yang, Y. Hu, X. Shen, Y. Yu, Y. Xiang, K. Cai, Osteogenesis of 3D printed porous Ti$_6$Al$_4$V implants with different pore sizes, J. Mech. Behav. Biomed. Mater. 84 (**2018**) 1–11.

[87] J. Parthasarathy, B. Starly, S. Raman, A. Christensen, Mechanical evaluation of porous titanium (Ti$_6$Al$_4$V) structures with electron beam melting (EBM), J. Mech. Behav. Biomed. Mater. 3 (**2010**) 249–259.

[88] L. Xiang, L. Yun, W. Chengtao, Z. Wenguang, L. Yuanchao, Fabrication and in vivo evaluation of Ti$_6$Al$_4$V implants with controlled porous structure and complex shape, Front. Mech. Eng. 7 (**2012**) 66–71.

[89] D.C. Dunand, Effects of Pore Morphology and Bone Ingrowth on Mechanical Properties of Microporous Titanium as an Orthopaedic Implant Material, Mater. Trans. 45 (**2004**) 1124–1131.

[90] J. Xiao, Y.L. Liao, G.B. Qiu, Titanium Foams Prepared by Using Carbamide as Spacer for Cortical Bone Implant, Mater. Sci. Forum. 815 (**2015**) 321–326.

[91] T.H. Reddy, S. Pal, K.C. Kumar, M.K. Mohan, V. Kokol, Finite element analysis for mechanical response of magnesium foams with regular structure obtained by powder metallurgy method, Procedia Eng. 149 (**2016**) 425–430.

[92] S. Zhao, S.J. Li, W.T. Hou, Y.L. Hao, R. Yang, L.E. Murr, Microstructure and mechanical properties of open cellular Ti–6Al–4V prototypes fabricated by electron beam melting for biomedical applications, Mater. Technol. (**2016**) 1–10.

[93] A. Salerno, P.A. Netti, 1 - Introduction to biomedical foams BT - Biomedical Foams for Tissue Engineering Applications, Biomed. Foam. Tissue Eng. Appl. (**2014**) 3–39.

[94] X.B. Xue, Y.Y. Zhao, V. Kearns, R.L. Williams, Mechanical and Biological Properties of Titanium Syntactic Foams, Miner. Met. Mater. Soc. 2 (**2010**) 129–136.

[95]   Y. Cui, J. Jiang, Z. Lai, W.K. Wong, Z. Hu, An integrated optimisation algorithm for feature extraction, dictionary learning and classification, Neurocomputing. 275 (**2018**) 2740–2751.

[96]   A. Nouri, Titanium foam scaffolds for dental applications, Elsevier, **2016**.

[97]   L.M.R. De Vasconcellos, D. De Oliveira Leite, F.O. Nascimento, L.G.O. De Vasconcellos, M.L. De Alencastro Graça, Y.R. Carvalho, C.A.A. Cairo, Porous titanium for biomedical applications: An experimental study on rabbits, Med. Oral Patol. Oral Cir. Bucal. 15 (**2010**) e407–e412.

[98]   S.N. Dezfuli, S.K. Sadrnezhaad, M.A. Shokrgozar, S. Bonakdar, Fabrication of biocompatible titanium scaffolds using space holder technique, J. Mater. Sci. Mater. Med. 23 (**2012**) 2483–2488.

[99]   P. Siegkas, V.L. Tagarielli, N. Petrinic, L.P. Lefebvre, The compressive response of a titanium foam at low and high strain rates, J. Mater. Sci. 46 (**2011**) 2741–2747.

[100] N. Tuncer, G. Arslan, Designing compressive properties of titanium foams, J. Mater. Sci. 44 (**2009**) 1477–1484.

[101] T.F. Hong, Z.X. Guo, R. Yang, Fabrication of porous titanium scaffold materials by a fugitive filler method, J. Mater. Sci. Mater. Med. 19 (**2008**) 3489–3495.

[102] N. Tuncer, G. Arslan, E. Maire, L. Salvo, Influence of cell aspect ratio on architecture and compressive strength of titanium foams, Mater. Sci. Eng. A. 528 (**2011**) 7368–7374.

[103] M.R. Baldissera, P.R. Rios, L.R.O. Hein, H.R.Z. Sandim, Three-dimensional characterization of pores in Ti-6Al-4V alloy, Mater. Res. 14 (**2011**) 102–106.

[104] S.R. Bhattarai, K.A.R. Khalil, M. Dewidar, H.H. Pyoung, K.Y. Ho, H.Y. Kim, Novel production method and in-vitro cell compatibility of porous Ti-6Al-4V alloy disk for hard tissue engineering, J. Biomed. Mater. Res. - Part A. 86 (**2008**) 289–299.

[105] X. Li, C.T. Wang, W.G. Zhang, Y.C. Li, Properties of a porous Ti-6Al-4V implant with a low stiffness for biomedical application, Proc. Inst. Mech. Eng. Part H J. Eng. Med. 223 (**2009**) 173–178.

[106] M.H. Lee, K.B. Kim, J.H. Han, J. Eckert, D.J. Sordelet, High strength porous Ti-6Al-4V foams synthesized by solid state powder processing, J. Phys. D. Appl. Phys. 41 (**2008**).

[107] E.E. Aşik, Ş. Bor, Fatigue behavior of Ti-6Al-4V foams processed by magnesium space holder technique, Mater. Sci. Eng. A. 621 (**2015**) 157–165.

[108] B. Arifvianto, M.A. Leeflang, J. Zhou, Characterization of the porous structures of the green body and sintered biomedical titanium scaffolds with micro-computed tomography, Mater. Charact. 121 (**2016**) 48–60.

[109] C. Xiang, Y. Zhang, Z. Li, H. Zhang, Y. Huang, H. Tang, Preparation and compressive behavior of porous titanium prepared by space holder sintering process, Procedia Eng. 27 (**2012**) 768–774.

[110] S. Oppenheimer, D.C. Dunand, Solid-state foaming of Ti-6A1-4V by creep or superplastic expansion of argon-filled pores, Acta Mater. 58 (**2010**) 4387–4397.

[111] B. Lee, T. Lee, Y. Lee, D.J. Lee, J. Jeong, J. Yuh, S.H. Oh, H.S. Kim, C.S. Lee, Space-holder effect on designing pore structure and determining mechanical properties in porous titanium, Mater. Des. 57 (**2014**) 712–718.

[112] D.P. Mondal, M. Patel, H. Jain, A.K. Jha, S. Das, R. Dasgupta, The effect of the particle shape and strain rate on microstructure and compressive deformation response of pure Ti-foam made using acrowax as space holder, Mater. Sci. Eng. A. 625 (**2015**) 331–342.

[113] Z. Esen, Ş. Bor, Characterization of Ti-6Al-4V alloy foams synthesized by space holder technique, Mater. Sci. Eng. A. 528 (**2011**) 3200–3209.

[114] D.J. Jorgensen, D.C. Dunand, Ti-6Al-4V with micro- and macropores produced by powder sintering and electrochemical dissolution of steel wires, Mater. Sci. Eng. A. 527 (**2010**) 849–853.

[115] M.M. Dewidar, J.K. Lim, Properties of solid core and porous surface Ti-6Al-4V implants manufactured by powder metallurgy, J. Alloys Compd. 454 (**2008**) 442–446.

[116] Q. Naziri, K. Issa, R. Pivec, S.F. Harwin, R.E. Delanois, M.A. Mont, Excellent Results of Primary THA Using a Highly Porous Titanium Cup, Orthopedics. 36 (**2013**) e390–e394.

[117] N. Tuncer, G. Arslan, E. Maire, L. Salvo, Investigation of spacer size effect on architecture and mechanical properties of porous titanium, Mater. Sci. Eng. A. 530 (**2011**) 633–642.

[118] D.P. Mondal, M. Patel, S. Das, A.K. Jha, H. Jain, G. Gupta, S.B. Arya, Titanium foam with coarser cell size and wide range of porosity using different types of evaporative space holders through powder metallurgy route, Mater. Des. 63 (**2014**) 89–99.

[119] Y. Li, Z. Guo, J. Hao, S. Ren, Porosity and mechanical properties of porous titanium fabricated by gelcasting, Rare Met. 27 (**2008**) 282–286.

[120] N. de F. Daudt, M. Bram, A.P.C. Barbosa, A.M. Laptev, C. Alves, Manufacturing of highly porous titanium by metal injection molding in combination with plasma treatment, J. Mater. Process. Technol. 239 (**2017**) 202–209.

[121] L.M.R. de Vasconcellos, M.V. de Oliveira, M.L. de A. Graça, L.G.O. de Vasconcellos, Y.R. Carvalho, C.A.A. Cairo, Porous titanium scaffolds produced by powder metallurgy for biomedical applications, Mater. Res. 11 (**2008**) 275–280.

[122] L.J. Gibson, Mechanical Behavior of Metallic Foams, Annu. Rev. Mater. Sci. 30 (**2000**) 191–227.

[123] M. Ashby, A. Evans, N. Fleck, L. Gibson, J. Hutchinson, H. Wadley, F. Delale, Metal Foams: A Design Guide, **2001**.

[124] F. Causa, N. Gargiulo, E. Battista, P.A. Netti, Titanium biomedical foams for osseointegration, in: Biomed. Foam. Tissue Eng. Appl., Elsevier, **2014**: pp. 391–411.

[125] B.M. Willie, X. Yang, N.H. Kelly, J. Merkow, S. Gagne, R. Ware, T.M. Wright, M.P.G. Bostrom, Osseointegration into a novel titanium foam implant in the distal femur of a rabbit, J. Biomed. Mater. Res. - Part B Appl. Biomater. 92 (**2010**) 479–488.

[126] B. Matijasevic, J. Banhart, Improvement of aluminium foam technology by tailoring of blowing agent, Scr. Mater. 54 (**2006**) 503–508.

[127] K. Alvarez, H. Nakajima, Metallic scaffolds for bone regeneration, Materials (Basel). 2 (**2009**) 790–832.

[128] S. Arabnejad Khanoki, D. Pasini, Multiscale Design and Multiobjective Optimization of Orthopedic Hip Implants with Functionally Graded Cellular Material, J. Biomech. Eng. 134 (**2012**) 031004.

[129] X. Jian, C. Hao, Q. Guibao, Y. Yang, L. Xuewei, Investigation on relationship between porosity and spacer content of titanium foams, Mater. Des. 88 (**2015**) 132–137.

[130] D.P. Mondal, J. Datta Majumder, N. Jha, A. Badkul, S. Das, A. Patel, G. Gupta, Titanium-cenosphere syntactic foam made through powder metallurgy route, Mater. Des. 34 (**2012**) 82–89.

[131] X.H. Wang, J.S. Li, R. Hu, H.C. Kou, L. Zhou, Mechanical properties of porous titanium with different distributions of pore size, Trans. Nonferrous Met. Soc. China (English Ed. 23 (**2013**) 2317–2322.

[132] I.M. Arabatzis, P. Falaras, Synthesis of porous nanocrystalline TiO2 foam, Nano Lett. 3 (**2003**) 249–251.

[133] B. Matijasevic-Lux, J. Banhart, S. Fiechter, O. Görke, N. Wanderka, Modification of titanium hydride for improved aluminium foam manufacture, Acta Mater. 54 (**2006**) 1887–1900.

[134] B. Xie, Y.Z. Fan, T.Z. Mu, B. Deng, Fabrication and energy absorption properties of titanium foam with CaCl2as a space holder, Mater. Sci. Eng. A. 708 (**2017**) 419–423.

[135] Z. Esen, Ş. Bor, Processing of titanium foams using magnesium spacer particles, Scr. Mater. 56 (**2007**) 341–344.

[136] A. Salimon, Y. Bréchet, M.F. Ashby, A.L. Greer, Potential applications for steel and titanium metal foams, J. Mater. Sci. 40 (**2005**) 5793–5799.

[137] H.C. Hsu, S.K. Hsu, S.C. Wua, P.H. Wang, W.F. Ho, Design and characterization of highly porous titanium foams with bioactive surface sintering in air, J. Alloys Compd. 575 (**2013**) 326–332.

[138] J.T. Hsu, Y.J. Chen, J.T. Ho, H.L. Huang, S.P. Wang, F.C. Cheng, J. Wu, M.T. Tsai, A comparison of micro-CT and dental CT in assessing cortical bone morphology and trabecular bone microarchitecture, PLoS One. 9 (**2014**).

[139] K. Kato, S. Ochiai, A. Yamamoto, Y. Daigo, K. Honma, S. Matano, K. Omori, Novel multilayer Ti foam with cortical bone strength and cytocompatibility, Acta Biomater. 9 (**2013**) 5802–5809.

[140] F. Li, J. Li, H. Kou, L. Zhou, Anisotropic Porous Ti_6Al_4V Alloys Fabricated by Diffusion Bonding: Adaption of Compressive Behavior to Cortical Bone Implant Applications, J. Mater. Sci. Technol. 32 (**2016**) 937–943.

[141] H. Lee, T.S. Jang, J. Song, H.E. Kim, H. Do Jung, Multi-scale porous Ti_6Al_4V scaffolds with enhanced strength and biocompatibility formed via dynamic freeze-casting coupled with micro-arc oxidation, Mater. Lett. 185 (**2016**) 21–24.

[142] A.E. Johnson, T.S. Keller, Mechanical properties of open-cell foam synthetic thoracic vertebrae, J. Mater. Sci. Mater. Med. 19 (**2008**) 1317–1323.

[143] J.P. Li, J.R. De Wijn, C.A. Van Blitterswijk, K. De Groot, Porous Ti_6Al_4V scaffolds directly fabricated by 3D fibre deposition technique: Effect of nozzle diameter, J. Mater. Sci. Mater. Med. 16 (**2005**) 1159–1163.

[144] M.A. Lopez-Heredia, E. Goyenvalle, E. Aguado, P. Pilet, C. Leroux, M. Dorget, P. Weiss, P. Layrolle, Bone growth in rapid prototyped porous titanium implants, J. Biomed. Mater. Res. - Part A. 85 (**2008**) 664–673.

[145] J.P. Li, J.R. De Wijn, C.A. Van Blitterswijk, K. De Groot, Porous Ti_6Al_4V scaffold directly fabricating by rapid prototyping: Preparation and in vitro experiment, Biomaterials. 27 (**2006**) 1223–1235.

[146] M.A. Lopez-Heredia, J. Sohier, C. Gaillard, S. Quillard, M. Dorget, P. Layrolle, Rapid prototyped porous titanium coated with calcium phosphate as a scaffold for bone tissue engineering, Biomaterials. 29 (**2008**) 2608–2615.

[147] A. Mansourighasri, N. Muhamad, A.B. Sulong, Processing titanium foams using tapioca starch as a space holder, J. Mater. Process. Technol. 212 (**2012**) 83–89.

[148] M. Collins, J. Bassett, H.B. Wen, C. Gervais, M. Lomicka, P. Sawas, Trabecular Metal ™ Dental Implants : Overview of design and developmental research, Zimmer Dent. Inc. (**2012**) 24–27.

metals MDPI

Article

Fabrication, morphology analysis, and mechanical properties of Ti foams manufactured using the space holder method for bone substitute materials

Oktay Cetinel [1,*], Ziya Esen [2] and Bora Yildirim [1]

[1] Department of Mechanical Engineering, Hacettepe University, 06800 Beytepe, Ankara,Turkey; oktaycetinel@hacettepe.edu.tr (O.C.); boray@hacettepe.edu.tr (B.Y.)

[2] Department of Materials Science and Engineering, Cankaya University, 06790 Etimesgut, Ankara,Turkey; ziyaesen@cankaya.edu.tr

[*] Correspondence: oktaycetinel@hacettepe.edu.tr; Tel.: +90-312-418-4129

Abstract: Porous titanium (Ti) offers several key attributes as a biomedical material. Among the known characteristics of Ti relevant to biomedical applications, the mechanical performance and effects of a pore structure on the deformation characteristics under compressive loading were examined. The space holder method was employed to generate Ti foams with target porosities of 60%, 70%, and 80%. A micro-computed tomography analysis and optical and scanning electron microscopy were performed to examine the pore morphology and microstructure. The mechanical properties along with the elastic modulus and compressive strength were evaluated via uniaxial compression testing. Ti foam samples with three porosity levels displayed average elastic moduli and compressive strengths comparable to those of human cancellous and cortical bone. All Ti foam samples had elastic moduli similar to those of cancellous bone with their open porous structures. Although the foam samples with ~60% porosity had compressive strength comparable to that of cortical bone, the samples with ~80% porosity displayed compressive strength similar to that of cancellous bone. The results indicate that Ti foam scaffolds produced using the space holder method have great potential for applications in hard tissue engineering, as their mechanical properties and pore structures are similar to those of bone.

Keywords: biomaterials; Ti foam; micro-CT analysis; mechanical properties

1. Introduction

The superior biocompatibility, specific strength, and corrosion resistance of titanium (Ti) and its alloys have led to the extensive use of these materials in bone implants [1–3]. A major problem with such implants is stress shielding due to the difference between the elastic moduli of implant materials (110 GPa for Ti) and that of bone (10–30 GPa). This difference leads to delayed bone healing, increased porosity in the bone surrounding the implant, and loosening of the implant [4, 5]. These issues have generated growing interest in the development of metallic implant materials with reduced elastic moduli.

In particular, porous materials have attracted increasing research interest as potential orthopedic materials with well-matched elastic moduli that permit long-term bonding via full in-growth of the bone tissues [6–8]. Various porous materials have been discussed in numerous published reviews focused on the importance of both mechanical and microscopic structural properties (pore size and porosity) [8–10]. In particular, the significance of these morphological properties for achieving bone regeneration via osteogenesis was discussed [11]. While significant bone in-growth was reported for large pore sizes of 100–600 μm, small pore sizes of 75–100 μm show unmineralized osteoid tissue growth and 10–75 μm pores exhibit fibrous tissue growth [12, 13]. Hence, 100 μm is usually regarded as the minimum pore size for successful mineralized bone regeneration [14–18].

Porous Ti scaffolds can be produced using several methods such as additive manufacturing, foaming, and powder metallurgy. The economy and high efficiency of powder metallurgy have resulted in broad industrial applications in material blending and compaction, facilitating the mass production of implant materials with tailored compositions, shapes, and mechanical properties [19]. Moreover, powder sintering in combination with space holder techniques can generate highly porous scaffolds with effective control of the morphology. Many authors have described this approach, in which the metallic powders and space holder particles are mixed together and compacted prior to the removal of the space holders either before or during sintering [14–16]. Magnesium (Mg) has also been reported to be a potential space holder material for fabricating porous scaffolds of Ti [2].

The porosity, pore size, and morphology of the resulting material determine its mechanical properties. Hence, numerous researchers have examined the effects of various porosities and/or pore sizes on the mechanical performance of porous Ti [2, 6–11]. Nevertheless, the effect of varying the pore-size distribution has not been well examined using micro-CT analysis [20].

In the present study, a Mg powder space holder was used in a powder metallurgical approach to produce porous Ti scaffolds for applications in tissue engineering. The aim was to produce metallic scaffolds with interconnected pore structures along with mechanical characteristics compatible with those of human cancellous and cortical bones. Compatible osteointegration and deformation behavior of the porous Ti implant also were also investigated.

2. Materials and Methods

2.1. Scaffold preparation

The powder metallurgy method was used to generate porous Ti scaffolds, in which the porosity was constrained by varying the volume ratio of Mg to Ti powder. For the primary matrix, angular Ti powder (> 99% purity (ASTM 1580-1) with an average particle size of 53.6 μm and normal particle size distribution of 50–60 μm was used. For the space-holder material Mg was chosen because it has very limited solid solubility in Ti [2]. Spherical Mg powder (>99.5% purity) with an average particle size of around 300 μm and normal particle size distribution 250–355 μm was employed. The selection of Mg powder size was informed by published work in which a pore size of 250 μm was found to assist cell migration, while optimal mechanical properties of the porous structure were achieved via high sphericity [2]. Hence, a 250 μm pore size was aimed at for optimum osteointegration performance after sintering the porous samples.

The PVA(Polyvinyl Alcohol) added Ti powder was mixed for 1 h with Mg powders to generate powder mixtures containing 60%, 70%, and 80% Mg by volume. Cylindrical samples (9 mm diameter, 9 mm height) for characterization were then produced by uniaxial compression at 600 MPa using a 12t manual hydraulic press with floating die. At least three samples of each targeted porosity were prepared using the same procedure to analyze the repeatability and accuracy of the experiments.

The samples were sintered for 2 h under high purity Ar gas at 1200 °C in an atmosphere-controlled tube furnace. To avoid contamination during sintering, the samples were positioned in Ti crucibles

obtained by machining of Ti rods. To avoid adverse effects on the scaffold integrity due to melting and boiling of the Mg powders and to enable maximum removal of the space-holder, the furnace was heated to the sintering temperature (above the boiling point of Mg, 1090 °C) slowly at a heating rate of 4 °C/min.

2.2. Morphology, porosity, and phase analysis

Optical and scanning electron microscopies (SEM, Jeol JSM 6400) were used to examine the morphology and microstructure of the foams. For this procedure, the specimens were crushed to see the pore structure and prepared metallographically after mounting the samples, which were cut longitudinally along the axis of compaction. Kroll's reagent was used to reveal the underlying microstructures of the foams. In addition, to study the pore morphology of the specimens under compressive deformation, each specimen was examined both before and after application of a minimal compressive strain.

The internal and external pore shapes, along with surface and volume characteristics relevant to bone histomorphometry (e.g., porosity and pore distribution) were examined by micro-computed tomography (micro-CT) using a Skyscan 1272 industrial micro-CT machine (Brüker GmbH, Germany), affording a maximum resolution of 0.35 μm (16Mp). A step size of 0.01 mm was used to examine the scaffold cross-sections in three directions.

ImageJ was used to analyze the micropore distribution patterns with the image threshold technique on SEM images to determine the overall porosity level and microporosity and to calculate the mean pore diameter equivalents, pore morphology, and sizes. Following scanning, the micrograph images underwent a cleaning process to sharpen the features, allowing for more precision and accuracy in the analysis. This stage is necessary as the program in imaging employs color threshold changes; thus, the clean image allows for closer examination of the details of the micrograph. Following image analysis, the extracted data were then stored in Microsoft Excel format to allow for additional statistical analysis and presentation in graphs. Doing so made it possible to determine the pore distribution and the relationship between the immersion period and final micropore size/structure.

The main phases in the manufactured porous samples were identified via X-ray diffraction (XRD, RigakuD/Max2200/PC) analysis at 40 kV and 2θ angles between 30° and 90° using a Cu-Kα radiation source.

2.3. Mechanical testing

To examine their mechanical properties, cylindrical porous Ti samples (9 mm diameter, 9 mm height) were subjected to compression testing at room temperature using an Instron 3369 with a cross head speed of 0.005 mm/s. To obtain the stress–strain curves of samples, each specimen was subjected to an increasing load until complete fracture of the specimen was observed. The moduli of the samples were found by measuring the slopes of the linear regions of the curves, while the compression strengths were measured at the maximum stress levels of the stress–strain curves. The evaluated results were also compared with human cortical and cancellous bone to analyze the similarities.

3. Results

3.1. Morphology and phase analysis

Representative SEM images obtained from the crushed cross-sections of samples designed to have porosities near 60%, 70%, and 80% are shown in Figure 1. After Mg removal by evaporation, the samples with target porosities of 60%, 70%, and 80% were observed to have porosities in the ranges of 55.9%–58.7%, 68.4%–69.9%, and 76.4%–78.0%, respectively. The small discrepancies between the target and obtained porosity levels were attributed to sintering, which resulted in shrinkage of the samples by the formation of sintering bonds between particles. In the samples with relatively low additions of

Mg particles, i.e., 60% Mg, the pore shapes were usually round with smoothly curved pore walls. For higher porosity levels, the pore shape started to deviate from a perfect spherical shape probably due to pore interconnections.
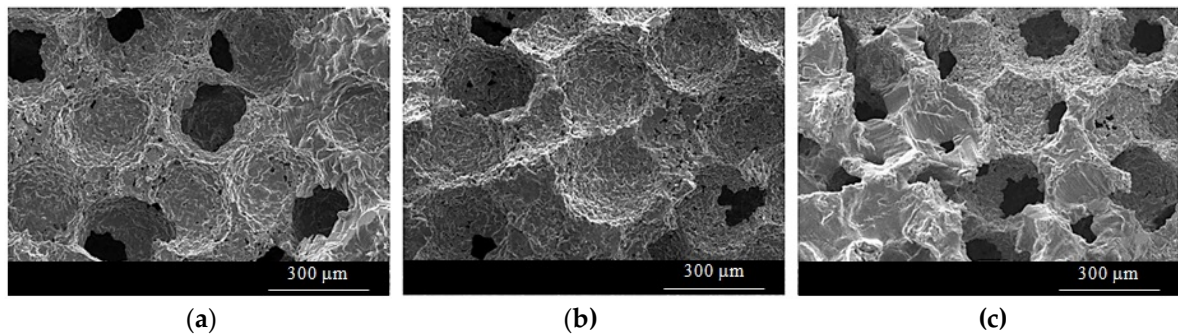

Figure 1. SEM macrostructure of porous Ti samples at ×100 magnification with porosities of (**a**) 55.9%, (**b**) 68.4%, and (**c**) 78%.

Along with the large macro-pores generated by removing the Mg particles, Figure 2 reveals the presence of micro-pores on the cell walls as well due to incomplete sintering of the Ti powders. This characteristic is typical of sintered Ti microstructures. Although the cell walls were microporous, the sintering was sufficient to form bonds between the Ti powders, as revealed by the grain boundaries of α-Ti in Figure 2(b).
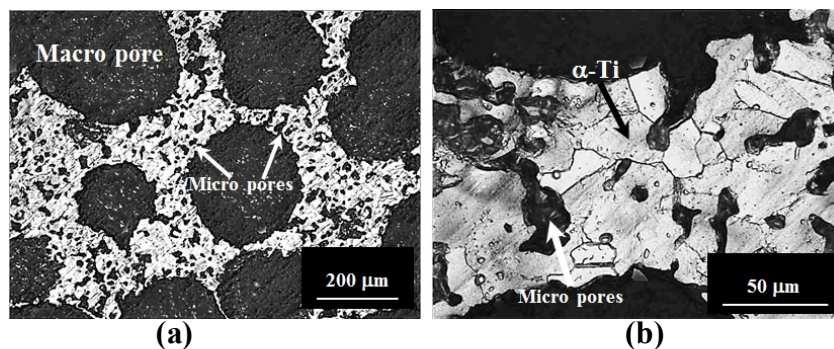

Figure 2. Polished cross-sectional optical microscope images of Ti-foam with 55.9% porosity showing (a) macro-pores formed by Mg evaporation and microporous cell walls and (b) cell walls containing micro-pores and grains of the α-Ti phase.

The micro-CT scan images for the samples with designed porosities of 60%, 70%, and 80% are shown in Figure 3. Moreover, the 3D solid models at 45° cut angles, which were obtained by re-construction of the actual specimen structure from a set of micro-CT images, are depicted in Figure 4.
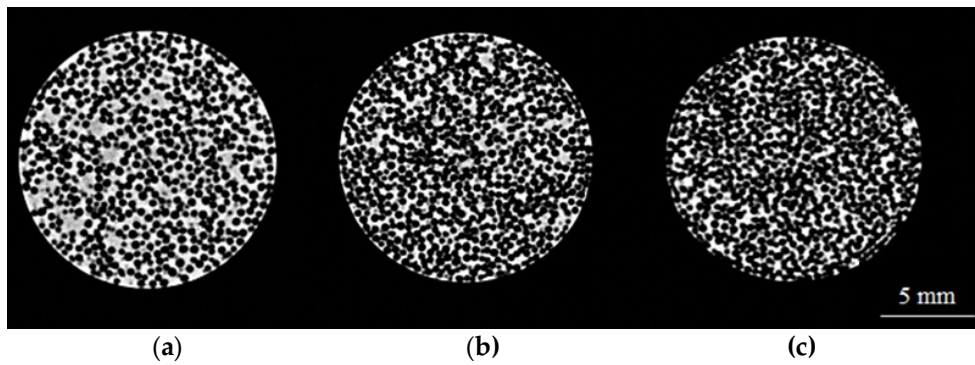
Figure 3. Micro-CT scan microstructure of porous Ti samples with porosities of (**a**) 55.9%, (**b**) 68.4%, and (**c**) 78.0%.

The micro-CT scans indicated a significant level of agreement between the target and obtained porosities. The average resultant pore diameters, measured using imageJ software, were around 253 μm, 267 μm, and 273 μm for the samples with target porosities of 60%, 70%, and 80%, respectively.
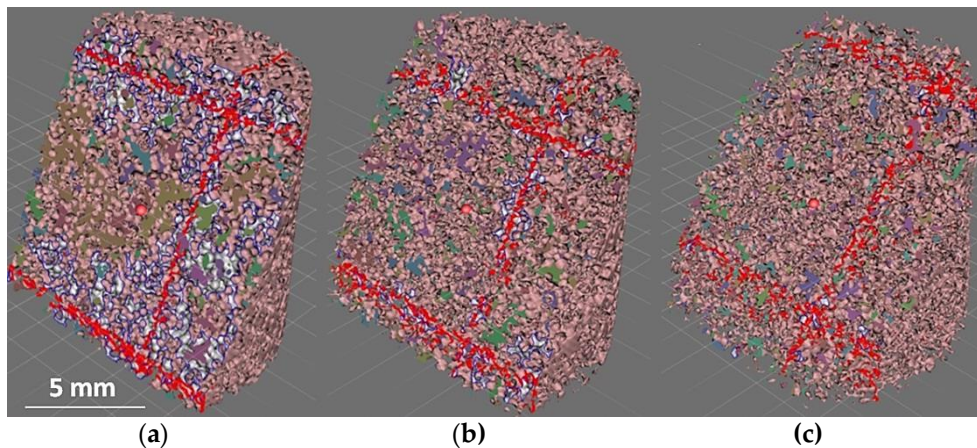

Figure 4. Three-dimensional solid models of porous Ti samples obtained at 45° cut angles with porosities of (**a**) 55.9%, (**b**) 68.4%, and (**c**) 78.0%.

As can be seen, the obtained pore size in all samples were less than the initial average Mg particle size (300 μm) probably due to sintering shrinkage, which caused further densification by formation of sintering bonds. The average pore size was observed to increase with increasing Mg content of the initial compacts since more interconnections occurred between the pores after removing Mg from these samples (Figure 3(c)).
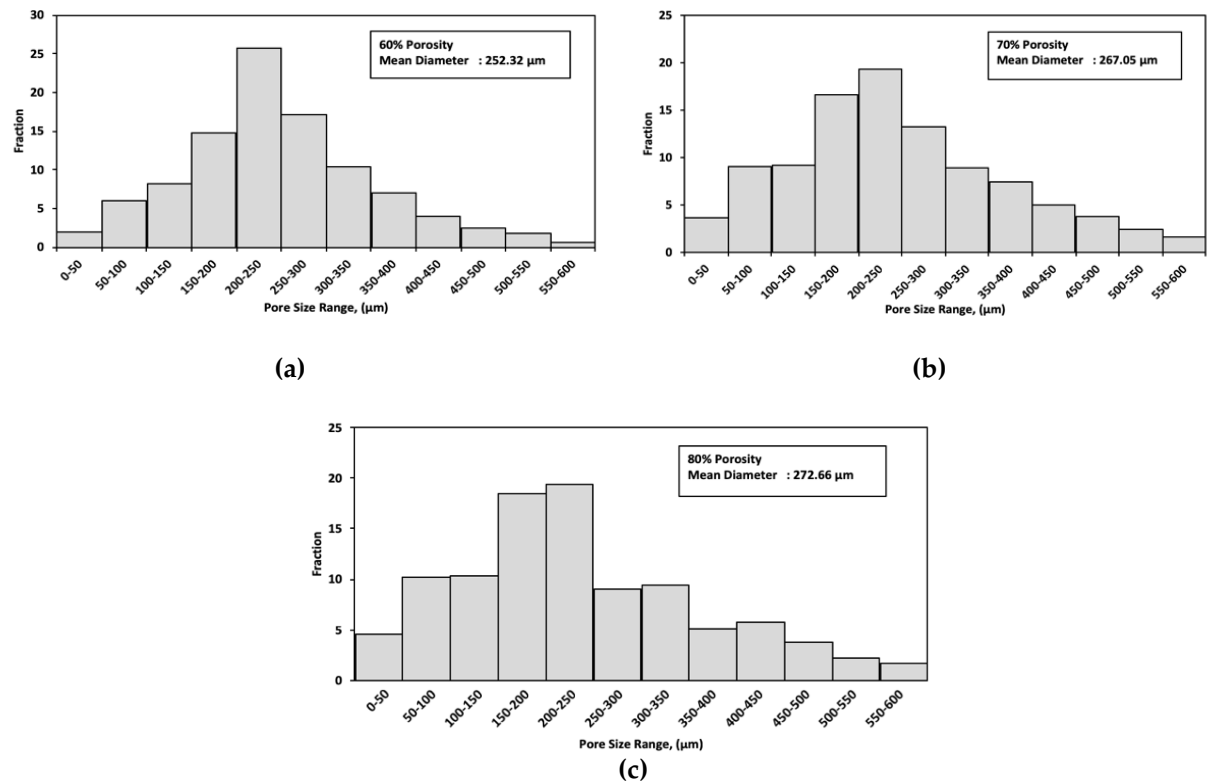
Figure 5. Porosity analysis results obtained using an imageJ image analyzer with targeted porosities of (a) 60%, (b) 70%, and (c) 80%.

According to the statistical pore-size analysis results (Figure 5), the Ti samples had pore sizes in the range of 5.0–887.5 μm. The pores larger than the initial Mg particles were due to the interconnection of large pores. Meanwhile, the pores smaller than the Mg particles and called micro-pores are likely due to partial sintering of Ti powders on the cell walls, as shown in Figure 2. Further, all of samples displayed largely uniform pore size distributions in the range of 150–300 μm with a good open porous structure both in the in their surface and interior regions.

In addition to the porosity content and the morphologies and type of pores, the production of Ti foams free of oxides and without binder residue or Mg is crucial for biomedical applications. In all of the samples, Mg was completely removed during production, so the manufactured foams were free of binder residue and Mg, as can be seen in the diffraction patterns in Figure 6. Moreover, no oxides of Ti were detected and the production technique yielded only the α-Ti phase, as revealed by the α-phase grains in Figure 2(b) and the diffraction pattern.
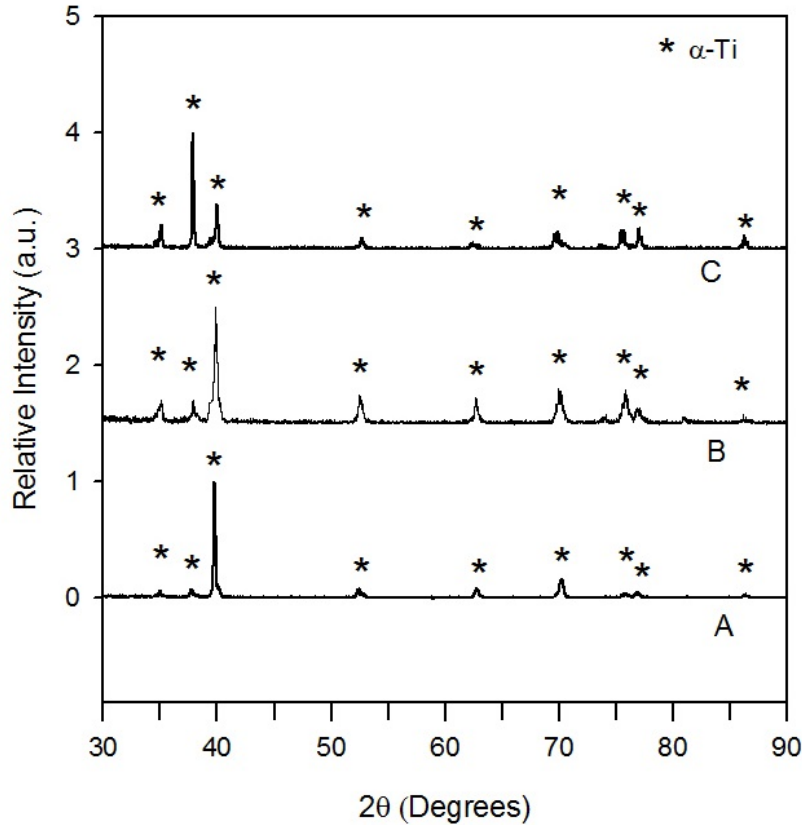
Figure 6. X-ray diffraction patterns of manufactured Ti foams. A: 55.9% porosity, B: 68.4% porosity, and C: 78.0% porosity.

3.2. Mechanical properties

3.2.1. Stress–strain curves

The compressive stress–strain curves of the Ti samples with target porosities of 60%, 70%, and 80% are presented in Figure 7. The curves show an initial elastic deformation phase followed by an extensive plateau with almost constant flow stress up to significant strains. The stress–strain curves of such foams also contain a densification stage in which the flow stress increases sharply. However, this stage could not be observed in the given curves since the samples fractured at the beginning of the densification stage. This type of behavior has also been widely observed in Ti foams in previous research studies [11-15].

All plateau regions were observed following maximum peak stresses, which suddenly dropped prior to the start of the plateau stage. The maximum peak compressive strengths were found to be around 148.0 MPa, 38.0 MPa, and 22.0 MPa, while their lowest values at the drop point were around 116.0 MPa, 34.0 MPa, and 16.0 MPa for 60%, 70%, and 80% porosity, respectively.
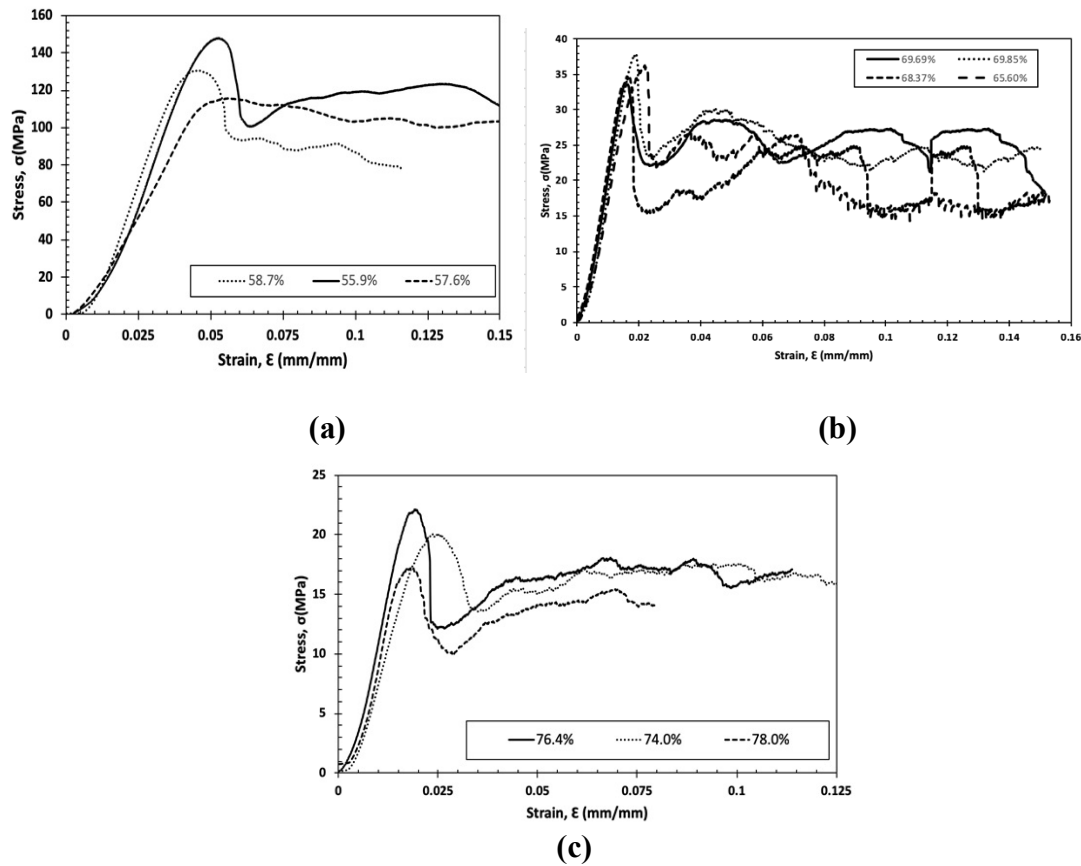
Figure 7. Compressive stress–strain curves of porous Ti with target porosities of (a) 60%, (b) 70%, and (c) 80%.

The elastic moduli of the Ti group samples with target porosities of 60%, 70%, and 80% are presented in Figure 7(a). In the present study, the elastic moduli were obtained from the slopes of the linear elastic regions. Thus, for the first group of samples (55.9%–58.7% porosity), the elastic moduli were 3.1–4.5 GPa, while the second group of samples (68.4%–69.9% porosity) had elastic moduli of 2.5—2.8 GPa, and the third group of samples (76.4%–78.0% porosity) displayed elastic moduli in the range of 1.2–1.7 GPa. The elastic modulus generally increased with decreasing porosity, with the maximum elastic modulus of 4.5 GPa being measured for the sample with 58.7% porosity. When the porosity was increased to 78.0%, the elastic modulus was reduced to just 1.7 GPa. This trend held true for the samples having porosities between the maximum and minimum porosities, as they displayed elastic moduli less than or equal to 2.8 GPa. The mean elastic moduli were calculated to be 4.0 GPa, 2.8 GPa, and 1.4 GPa for the samples with target porosities of 60%, 70%, and 80%, respectively. The calculated elastic moduli of the foams fall in the range of that of human cancellous bone (0.5–5 GPa) [21], which has an open porous structure similar to those of manufactured Ti foams. Therefore, manufactured foams may be evaluated as potential candidate biometals as they have elastic moduli similar to those of bone, which helps alleviate stress shielding.

Similar to the elastic modulus versus porosity change, the compressive strength (peak stress measured subsequent to the elastic region) displayed a decreasing tendency with increasing porosity. However, the strength drop beyond a target porosity of 60% is rather sharp (Figure 7(b)). Although the samples in the first group (55.9%–58.7% porosity) had compressive strengths in the range of cortical bone strength (100–230 MPa [21]), those in the third group (76.4%–78.0% porosity) had strengths similar to that of cancellous bone 2–12 MPa [21]. Meanwhile, the samples in the second group (68.4%–69.9% porosity) exhibited compressive strengths between those of cortical and cancellous bone. It is

clearly evident that, by alternating the porosity content, it is possible to tune the mechanical properties of foams to make them mechanically more compatible with human bone.

Implants made of bulk materials with greater elastic moduli and compressive strengths than bone do not permit the necessary transfer of stress to the neighboring bone. This situation promotes resorption of the bone surrounding the implant, thereby loosening the implant, reducing the service life, and ultimately requiring revision surgery. Hence, materials with mechanical properties more comparable to those of human bone (i.e., high strength and low elastic modulus) are necessary if these problems are to be avoided [13]. The porous Ti samples manufactured in the present study displayed compressive strengths and elastic moduli comparable with those of human bone, demonstrating the potential application of these materials in biomedical implants.
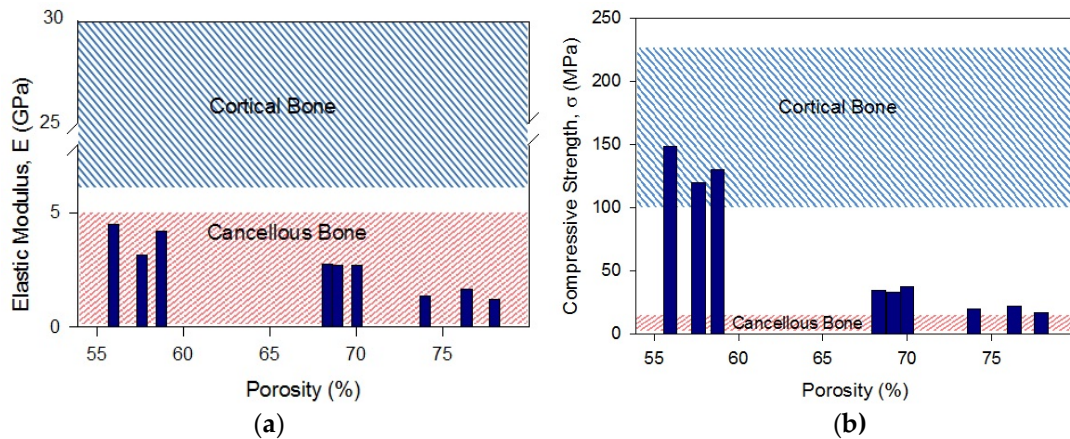

Figure 8. Mechanical property changes of Ti foams with porosity: (a) elastic modulus, (b) compressive strength.

3.2.2. Macroscopic deformation band

The surfaces of the deformed Ti specimens with 60%, 70%, and 80% target porosities are shown in Figure 9, indicating slight deformation of most of the pores along the edges. Moreover, deformation bands are evident within the 80% porous specimens, but absent from the 60% porous specimens. Nevertheless, local deformation partially surrounding the pores is evident at low porosities.

The development of deformation bands has previously been strongly correlated with the appearance of plateau regions in the compressive stress–strain curves for porous materials [22]. Hence, the plateau region observable in Figure 6 for the specimens with low porosity probably reflects the tendency of the specimens to undergo deformation one layer at a time, resulting in the deformation bands in the internal microstructures. This conclusion supports the observations made in previous studies [13].
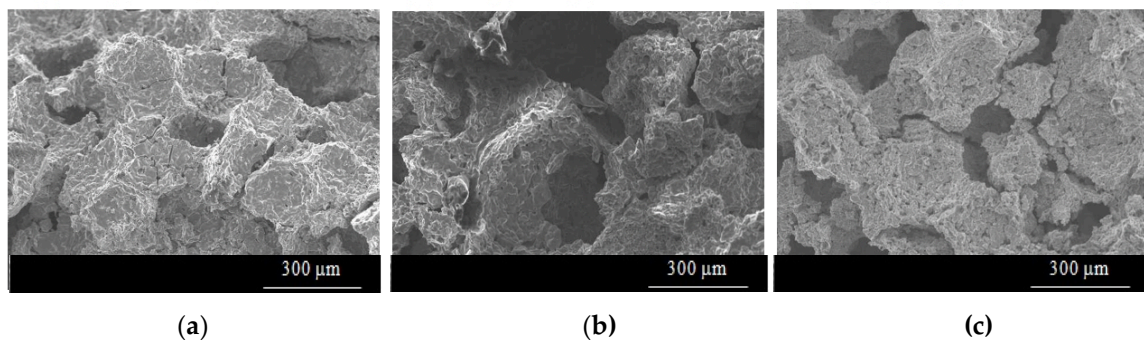

Figure 9. SEM microstructure of compressed porous Ti samples at ×100 magnification with porosities of (**a**) 60%, (**b**) 70%, and (**c**) 80%.

The less evident deformation band in the 70% porous specimen, along with only partial deformation around the pores, is also consistent with the absence of a plateau region in the stress–strain curve (Figure 6). This finding clearly demonstrates that deformation in porous Ti is largely dependent upon the porosity level.

3.2.3. Microscopic deformation mode of cell wall

The literature indicates three types of deformation modes for the cell wall, namely, bending, buckling, and yielding [14]. All three types of cell wall deformation are indicated in Figure 9 for the Ti specimens with 60%, 70%, and 80% target porosities.

All three types of deformations are observable for the 60% porous specimen (Figure 10a), which is consistent with published work in which bending and buckling occur in every cell, leading to localized deformation [15]. However, Figure 10c reveals no buckling and little bending for the specimen with 80% porosity, while the majority of cell walls exhibit yielding deformation. Also visible are cracks in the cell walls, formed after yielding with a 45° angle to the cell wall.
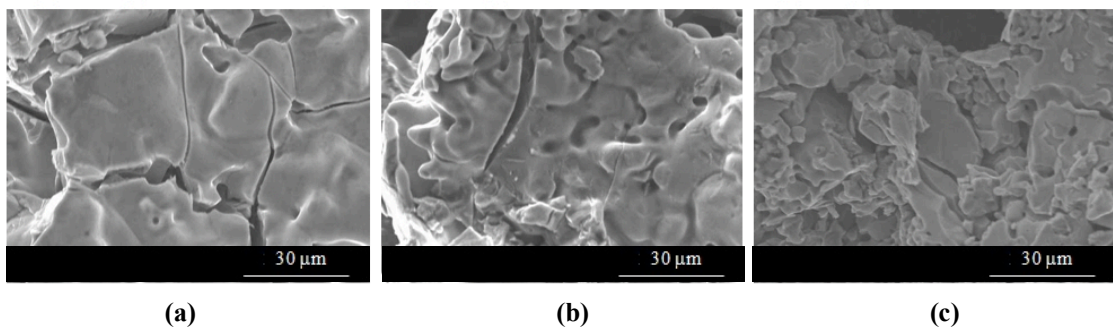

| (a) | (b) | (c) |

Figure 10. SEM images of compressed porous Ti samples at ×1000 magnification with target porosities of (a) 60%, (b) 70%, and (c) 80%.

Figure 9 clearly demonstrates that the Ti samples with 60% and 70% porosity deform by bending, buckling, and yielding of the cell walls, whereas the Ti sample with 80% porosity deforms by bending and yielding of the cell walls. Strong correlations have been noted between the microscopic and macroscopic deformation characteristics [8], indicating that the deformation of a porous metal involves three processes: (i) localized strain at cell nodes, (ii) development of discrete concentrated strain bands, and (iii) total plastic collapse. In contrast to the effects of yielding, cell wall buckling and bending led to strong local deformation, which promoted the development of deformation bands.

4. Discussion

4.1   Structure observation

Previous studies, both in vivo and in vitro, have shown that the desirable pore size of biomaterials is one of the key parameters in the process of bone development [5]. In the present study, the analysis indicated that the target porosity range of 150–300 μm was attained, with a uniform, narrow distribution of pores (256 μm +/− 28 μm) displaying high levels of interconnectivity from the center to the surface of the material. According to previous research, this pore morphology promotes osseointegration by aiding the transport of oxygen and nutrients necessary for the formation of blood vessels during the development of bone tissue [8]. Two types of pores were present in the Ti samples: (i) large or macro pores (100–350 μm), which promote direct bone formation, and (ii) small or micro

pores (<100 μm), which promote hypoxic conditions and stimulate the formation of articular cartilage prior to bone formation. Hence, previous researchers have argued that porous Ti with this type of connective three-dimensional network morphology could benefit bone formation as well as supplying pathways for effective in-growth of bone [8].

4.2   Mechanical properties

The presently available bulk implant materials display greater stiffness than human bone, thereby failing to transfer the requisite amount of stress to the surrounding bone. This shortcoming leads to implant loosening due to resorption of the bone surrounding the implant. Consequently, the development of implant materials with optimum combinations of compressive strength and low elastic modulus is necessary to prevent implant loosening, increase the implant service life, and circumvent the need for surgical re-adjustment [5]. The elastic modulus of human cortical bone is in the range of 7–30 GPa, while that of human cancellous bone is less than 5 GPa [21], and the compressive strength of human bone ranges from 2 MPa to 230 MPa [21]. In the present study, the Ti foam samples displayed decreasing compressive strengths of 148–16.0 MPa and elastic moduli of 4.5–1.2 GPa with increasing porosity. Thus, porous Ti materials with broad ranges of compressive strengths and elastic moduli are desirable equivalents to human bone, making Ti foams promising choices for biomedical applications.

5. Conclusions

In the present study, the space holder powder metallurgy technique was used in combination with a Mg powder space holder to produce biomimetic Ti scaffolds with selected porosities (60%, 70%, and 80%). Each porous scaffold displayed a significant degree of pore interconnectivity, which is favorable for osseointegration and in-growth of bone tissue. A porosity analysis also indicated that an appropriate pore size range was achieved for promoting osseointegration, as defined in previous literature [12, 13]. Moreover, the Ti foam samples with 60% and 80% porosity displayed compressive strengths compatible with those of human cortical and cancellous bone. Meanwhile, all the foam samples exhibited elastic moduli similar to that of cancellous bone. Hence, the combined results of the structural and mechanical analyses performed in this study suggest that Ti scaffolds manufactured using the described approach could be promising materials for applications in bone tissue-engineering.

References

1.   Singh, R.; Lee, P.D.; Jones, J.R.; Poologasundarampillai, G.; Post, T.; Lindley, T.C.; Dashwood, R.J. Hierarchically structured titanium foams for tissue scaffold applications. *Acta Biomater.* **2010**, *6*, 4596–4604.

2.   Esen, Z.; Bor, Ş. Characterization of Ti-6Al-4V alloy foams synthesized by space holder technique. *Mater. Sci. Eng. A* **2011**, *528*, 3200–3209.

3.   Kashef, S.; Asgari, S.A.; Hodgson, P.; Yan, W.Y. Simulation of Three-Point Bending Test of Titanium Foam for Biomedical Applications. *Adv. Mater. Res.* **2008**, *32*, 237–240.

4.   Imwinkelried, T. Mechanical properties of open-pore titanium foam. *J. Biomed. Mater. Res. - Part A* **2007**, *81*, 964–970.

5. Kashef, S.; Asgari, A.; Hilditch, T.B.; Yan, W.; Goel, V.K.; Hodgson, P.D. Fracture toughness of titanium foams for medical applications. *Mater. Sci. Eng. A* **2010**, *527*, 7689–7693.

6. Barrabés, M.; Sevilla, P.; Planell, J.A.; Gil, F.J. Mechanical properties of nickel-titanium foams for reconstructive orthopaedics. *Mater. Sci. Eng. C* **2008**, *28*, 23–27.

7. Matsushita, T.; Fujibayashi, S.; Kokubo, T. Titanium foam for bone tissue engineering. *Met. Foam Bone Process. Modif. Charact. Prop.* **2016**, *17*, 111–130.

8. Tuncer, N.; Arslan, G. Designing compressive properties of titanium foams. *J. Mater. Sci.* **2009**, *44*, 1477–1484.

9. Xue, X.B.; Zhao, Y.Y.; Kearns, V.; Williams, R.L. Mechanical and Biological Properties of Titanium Syntactic Foams. *Miner. Met. Mater. Soc.* **2010**, *2*, 129–136.

10. Mansourighasri, A.; Muhamad, N.; Sulong, A.B. Processing titanium foams using tapioca starch as a space holder. *J. Mater. Process. Technol.* **2012**, *212*, 83–89.

11. Kashef, S.; Asgari, A.; Hilditch, T.B.; Yan, W.; Goel, V.K.; Hodgson, P.D. Fatigue crack growth behavior of titanium foams for medical applications. *Mater. Sci. Eng. A* **2011**, *528*, 1602–1607.

12. Jian, X.; Hao, C.; Guibao, Q.; Yang, Y.; Xuewei, L. Investigation on relationship between porosity and spacer content of titanium foams. *Mater. Des.* **2015**, *88*, 132–137.

13. Sufizar Ahmad; Azizi Kassim Fabrication of titanium foam by using compaction method. *Eprints. Uthm. Edu. My* **2010**.

14. Spoerke, E.D.; Murray, N.G.; Li, H.; Brinson, L.C.; Dunand, D.C.; Stupp, S.I. A bioactive titanium foam scaffold for bone repair. *Acta Biomater.* **2005**, *1*, 523–533.

15. Xiong, J.Y.; Li, Y.C.; Wang, X.J.; Hodgson, P.D.; Wen, C.E. Titanium-nickel shape memory alloy foams for bone tissue engineering. *J. Mech. Behav. Biomed. Mater.* **2008**, *1*, 269–273.

16. Xiao, J.; Yang, Y.; Qiu, G.B.; Liao, Y.L.; Cui, H.; Lü, X.W. Volume change of macropores of titanium foams during sintering. *Trans. Nonferrous Met. Soc. China (English Ed.* **2015**, *25*, 3834–3839.

17. Li, J.P.; Li, S.H.; de Groot, K.; Layrolle, P. Preparation and Characterization of Porous Titanium. *Key Eng. Mater.* **2001**, *218–220*, 51–54.

18. Xie, B.; Fan, Y.Z.; Mu, T.Z.; Deng, B. Fabrication and energy absorption properties of titanium foam with CaCl2as a space holder. *Mater. Sci. Eng. A* **2017**, *708*, 419–423.

19. Bansiddhi, A.; Dunand, D.C. *Titanium and NiTi foams for bone replacement*; Woodhead Publishing Limited, **2014**; ISBN 9780857099037.

20. Sargeant, T.D.; Guler, M.O.; Oppenheimer, S.M.; Mata, A.; Satcher, R.L.; Dunand, D.C.; Stupp, S.I. Hybrid bone implants: Self-assembly of peptide amphiphile nanofibers within porous titanium. *Biomaterials* **2008**, *29*, 161–171.

21. Kokubo, T.; Yamaguchi, S. Novel Bioactive Titanate Layers Formed on Ti Metal and Its Alloys by Chemical Treatments. *Materials (Basel).* **2009**, *3*, 48–63.

22. Hsu, H.C.; Hsu, S.K.; Wua, S.C.; Wang, P.H.; Ho, W.F. Design and characterization of highly porous titanium foams with bioactive surface sintering in air. *J. Alloys Compd.* **2013**, *575*, 326–332.

23. Ghidelli, M.; Sebastiani, M.; Johanns, K.E.; Pharr, G.M. Effects of indenter angle on micro-scale fracture toughness measurement by pillar splitting. *J. Am. Ceram. Soc.* **2017**, *100*, 5731–5738.

24. Seong, W.-J.; Kim, U.-K.; Swift, J.Q.; Heo, Y.-C.; Hodges, J.S.; Ko, C.-C. Elastic properties and apparent density of human edentulous maxilla and mandible. *Int. J. Oral Maxillofac. Surg.* **2009**, *38*, 1088–93.

HACETTEPE UNIVERSITY
GRADUATE SCHOOL OF SCIENCE AND ENGINEERING
THESIS/DISSERTATION ORIGINALITY REPORT

HACETTEPE UNIVERSITY
GRADUATE SCHOOL OF SCIENCE AND ENGINEERING
TO THE DEPARTMENT OF MECHANICAL ENGINEERING

Date: 09/07/2019

Thesis Title / Topic: PRODUCTION AND CHARACTERISATION OF TITANIUM FOAM SCAFFOLDS AS BONE SUBSTITUTE MATERIALS

According to the originality report obtained by myself/my thesis advisor by using the *Turnitin* plagiarism detection software and by applying the filtering options stated below on 21/05/2019 for the total of 117 pages including the a) Title Page, b) Introduction, c) Main Chapters, d) Conclusion sections of my thesis entitled as above, the similarity index of my thesis is 5 %.

Filtering options applied:
1. Bibliography/Works Cited excluded
2. Quotes excluded / included
3. Match size up to 5 words excluded

I declare that I have carefully read Hacettepe University Graduate School of Sciene and Engineering Guidelines for Obtaining and Using Thesis Originality Reports; that according to the maximum similarity index values specified in the Guidelines, my thesis does not include any form of plagiarism; that in any future detection of possible infringement of the regulations I accept all legal responsibility; and that all the information I have provided is correct to the best of my knowledge.

I respectfully submit this for approval.

		Date and Signature
Name Surname:	OKTAY ÇETİNEL	
Student No:	N15244160	
Department:	MECHANICAL ENGINEERING	09.07.2019
Program:	MECHANICAL ENGINEERING P.h.D.	
Status:	☐ Masters ☒ Ph.D. ☐ Integrated Ph.D.	

ADVISOR APPROVAL

APPROVED.

Prof .Dr.Bora Yıldırım

CURRICULUM VITAE

Credentials

Name, Surname : Oktay ÇETİNEL

Place of Birth: ANKARA

Marital Status: Single

E-mail Address: oktaycetinel@hacettepe.edu.tr

Education

High School: Bilkent High School,2011

MEng: University of Bath, Mechanical Engineering,2015

PhD: Hacettepe University, Mechanical Engineering, 2019

Foreign Languages

German: Intermediate

English: Fluent

Areas of Experiences

- Finite Element Modelling
- Foam Modelling
- Sintering Technologies
- SEM Analysis
- Porosity Analysis
- Powder Metallurgy
- Simulation Technologies (LS-DYNA etc.)
- Fracture Mechanics
- Micro CT-Scan Technologies
- Process Re-engineering

- Needs Assessment
- Relationship Management

Work Experience

Mechanical Engineer/Shareholder, Sumer Inc.   June 2015 – Continuing

In charge of the manufacturing and research and development team at our family run company that focuses on Medical Device manufacturing and currently manufacture autoclaves, washer disinfectors, operating tables, warming cabinets, blood bank refrigerators and freezers, mother milk refrigerators and freezers and stainless steel hospital equipments to our 43 distributors worldwide with more than 38 years of experience in this field and currently own one of the biggest medical device manufacturing facilities in Turkey with a manufacturing space of over 25,000 m2 production area.

Mechanical Engineer/ Founding Partner, Adger Ltd.   September 2018 – Continuing

A university partnered company that provides special projects for Turkish National Army. Our current projects include mine resistant vehicle seat project for ASELSAN (Turkish Armed Forces Foundation) and mobile energy harvesting unit for Turkish Ministry of Defence (SSM).

Projects and Budgets

Researcher / Intern, Total Prenatal Nutrition (TPN) Project   June – September 2013
Sumer Inc. & Yildirim Beyazit University project dedicated to the design, domestic production and subsequent export of a TPN device suitable for use in newborn units, supported by The Scientific & Technological Research Council of Turkey (TUBITAK), with the aim of eliminating dependency on overseas manufacturers.

- Technology Management: Originated a new technological planning methodology by combining two disparate techniques, impressing project consultant Prof. Ugur Dilmen and receiving special commendation from the Technological Research Council of Turkey.

Researcher / Intern, Smart Blood Bank Refrigerator Project   June – September 2012
Sumer Inc. & Turkish Red Crescent

High visibility project, which received an award from the Ankara Chamber of Commerce, presented by Turkey's Prime Minister, and supported by T.R. Ministry of Development.

- Design Support: Actively involved in design and testing phases of the project; contributed to product usability by making insightful recommendations on functionality, sizing and portability, based on in-depth research.
- Requirements Analysis: Engaged with product's end users in hospitals in Ankara and Istanbul, gathering requirements and presenting findings to the Chief Engineer, which were incorporated into the design process.
- Quality Assurance: Carried out extensive product testing; calibrated equipment on a daily basis, backed up all information and ran overnight data processing programmes.

Publications

- Cetinel, O.; Esen, Z.; Yildirim, B. Fabrication, Morphology Analysis, and Mechanical Properties of Ti Foams Manufactured Using the Space Holder Method for Bone Substitute Materials. Metals 2019, 9, 340. https://doi.org/10.3390/met9030340

Oral and Poster Presentations

- OTEKON 09th International Automative Technologies Congress, Oral presentation, 2018, Numerical Modelling of Dynamics of Crash Box Collision Geometry
- ICWET 05th International Conference on Welding Technologies, Oral presentation, 2018, Effect of Filler Wire Chemical Composition On Joint Properties Of 1050a Aluminum Alloy
- ICWET 05th International Conference on Welding Technologies, Oral presentation, 2018, Steel-Composite (Al-SiC) Structural Materials and Characterisation of Its Joined Interfaces

- ICETAS 04th International Conference on Engineering Technology and Applied Sciences, Oral presentation, 2019,Modelling and Development of an Active Car Suspension on a Quarter Car Model